Development of photo/excited triplets based functional materials for aqueous systems

河野, 宏徳

Development of photo-excited triplets based functional materials for aqueous systems

Hironori Kouno

Department of Chemistry and Biochemistry
Graduate School of Engineering
Kyushu University

2020

Development of photo-excited triplets based functional materials for aqueous systems

Author : Hironori Kouno

Supervisor : Nobuo Kimizuka

A thesis submitted in fulfillment of the requirements for the degree of Doctor of Philosophy

in

Department of Chemistry and Biochemistry Graduate School of Engineering Kyushu University

March 2020

KYUSHU UNIVERSITY

Preface

The research described herein was conducted under the supervision of Professor Nobuo Kimizuka in the Department of Chemistry and Biochemistry, Graduate School of Engineering, Kyushu University, between April 2014 and March 2020.

This thesis should be of interest due to the phenomenal properties of photo-excited triplet states, especially triplet-triplet annihilation-based photon upconversion (TTA-UC) and triplet dynamic nuclear polarization (triplet-DNP). In physics area, a lot of intriguing phenomena have been found, however, most of them are still fundamental research. To overcome this situation, molecular design from the viewpoint of molecular systems is essential to promote the functionality. I hope my research provides an important initial step towards the practical use of TTA-UC and triplet DNP.

Acknowledgements

Foremost, I would like to thank Professor Nobuo Kimizuka who guided me and continuously encouraged me in the past six years. I am grateful to him for introducing me to the wonders of scientific research and providing excellent research facilities and an outstanding research ambiance. Notably, I learned how to design molecular structures with remarkable functionality for molecular systems. I believe it is one of the original things I learned in Kimizuka Laboratory. And I warmly thank him for his precious advice, criticism and discussions on my work.

I am deeply indebted to Associate Professor Nobuhiro Yanai for providing invaluable guidance throughout my research. I got unique opportunity to learn how to set up a completely new research topic. And his diligent effort and training were the stepping stone behind each and every success I achieved, and will undoubtedly remain the prime asset for my future research.

My sincere thanks also go to Associate Professor Teppei Yamada, Associate Professor Shigenori Fujikawa and Assistant Professor Masa-aki Morikawa. They gave me a lot of advices and suggestions at every step of my research.

I express great gratitude to Dr. Tomohiro Uesaka and Dr. Kenichiro Tateishi (Cluster for Pioneering Research, RIKEN, RIKEN Nishina Center for Accelerator-Based Science) for their piercing suggestions and valuable discussions during the collaborations.

This work was partly supported by JSPS KAKENHI grant number JP25220805 (Grants-in-Aid for Scientific Research (S)), JP26810036 (Grant-in-Aid for Young Scientists (B)), JP16H00844 (Grant-in-Aid for Scientific Research on Innovative Area), JP17H04799 (Grant-in-Aid for Young Scientists (A)), JP16H06513 (Grant-in-Aid for Scientific Research on Innovative Areas: Coordination Asymmetry), JP16H00844 (Grant-in-Aid for Scientific Research on Innovative Areas: Soft Molecular Systems), JPMJPR14KE (PRESTO program on "Molecular Technology and Creation of New Functions" from JST), The Murata Science Foundation, JPMJPR18GB (PRESTO program on "Creation of Life Science Basis by Using Quantum Technology), The Yoshida Foundation for the Promotion of Learning and Education, JP17J04506 (Grant-in-Aid for JSPS Research Fellow).

I would like to thank Technical staff Kazumi Matsuno, Ryo Maeda, Azusa Suematsu and Chihoko Fukakusa for their warm solicitudes. I sincerely appreciate Professor Yosiki Katayama and Professor Takuma Yasuda for reviewing this thesis.

The author wishes to express his gratitude to Professor Pengfei Duan (National Center for Nanoscience and Technology, China), Assistant Professor Shogo Amemori (Kanazawa University), Assistant Professor Angelo Monguzzi (Università degli Studi di Milano-Bicocca), Dr. Keita Ishiba, Dr. Joseph Ka Ho Hui, Dr. Kouta Masutani, Dr. Deepak Asthana, Dr. Rakesh Kumar Gupta, Dr. Pankaj Bharmoria, Dr. Biplab Joarder, Dr Arijit Mallick, Dr. Taku Ogawa, Dr. Kazuma Mase, Dr. Hisanori Nagatomi, Mr. Daisuke Kichise, Mr. Yuya Nagao, Dr. Masaya Matsuki, Dr Masanori Hosoyamada, Dr. Shota Hisamitsu, Mr. Taro Wakiyama, Ms. Rina Yoshida, Dr. Yimin Liang, Mr. Tsubasa Kashino, Mr. Kanji Shiraishi, Mr. Ryosuke Yamamoto, Mr. Keisuke Kanakogi, Mr. Yuta Kubo, Mr. Tomoya Shimono, Ms. Mariko Kozue, Mr. Keisuke Okumura, Mr. Shinya Uchino, Mr. Hirotaka Ohara, Mr. Yoichi Sasaki, Ms. Hanyu Yang, Mr. Toshiki Eguchi, Mr. Hongyou Zhou, Mr. Yuki Nagai, Ms. Nao Hirakawa, Mr. Saiya Fujiwara, Mr. Junji Miyano, Ms. Xiaopeng Zou, Mr. Yusuke Kawashima, Ms. Fan Gao, Ms. Risa Okeda, Ms. Mika Kinoshita, Mr. Takashi Kobayashi, Mr. Tetsuro Kobayashi, Mr. Keisuke Hayashi, Ms. Rena Haruki, Mr. Koki Nishimura, Mr Hirotaka Inoue, Ms. Risa Iwami, Ms. Mone Sakata, Mr. Yuichiro Seki, Mr. Naoyuki Harada, Ms. Kana Orihashi, Ms. Mio Koharagi, Mr. Donggyu Kwak, Mr. Issei Maruyama, Ms. Kanae Izumi, Mr. Jumpei Kondo, Mr. Kentaro Tanaka, Mr. Ryoichi Tomomatsu, Mr. Tomoyuki Hamachi, Mr. Fumitoshi Matoba, Mr. Akio Yamauchi, Ms. Naura Fakhira Antariksa for warm supports and discussion.

Dr. Taku Ogawa and Dr. Shogo Amemori have been great mentors to me. I received kind guidance of not only experimental technique but also the way to proceed research. And teaching my juniors, Ms. Rena Haruki, Mr. Yusuke Kawashima, Mr. Koki Nishimura, and Mr. Tomoyuki Hamachi, was one of the important experiences in my research. I have learned so much things while working with all of you, though I'm afraid that I may have given you much trouble.

Friends and family have furthermore contributed to this publication. I thank my grandparents Yukio Ohtani and Ryoko Ohtani and my younger brother Hisashi Kouno for their continuous support and encouragement. Last but not least, I would like to pay high regards to my parents Taka Kouno and Emi Kouno for their sincere encouragement throughout my life.

Hironori Kouno
Department of Chemistry and Biochemistry
Graduate School of Engineering, Kyushu University
March 2020

Contents

Chapter 1 General introduction

1.1 Physical phenomena based on photo-excited triplet states

Recently, the interesting properties of photo-excited triplet states have attracted much attention, e.g., triplet-triplet annihilation-based photon upconversion (TTA-UC),[1-15] triplet dynamic nuclear polarization (triplet-DNP),[16-21] singlet fission (SF),[22,23] organic light emitting diodes (OLED),[24,25] and nitrogen vacancy centers (NVC).[26,27] The unique properties of triplet excited states of functional molecular materials are promising for the development of novel materials.

1.1.1 Spin configurations of triplet excited states

A state energy-level diagram (Figure 1-1) provides a model for displaying the relative energies of the ground state (S_0), lowest-energy excited state (S_1), and lowest energy triplet state (T_1) of an organic molecule. In an energy-level diagram, the vertical coordinate represents the potential energy of the system and the horizontal coordinate has no physical meaning. In the Born-Oppenheimer approximation, nuclei are static with respect to the movement of electrons and the nuclear coordinates can be separated from the electrons. The electronic configurations of S_0, S_1 and T_1 are shown in Figure 1-1.[28] According to Kasha's rule, the excitation of higher-energy excited states generally results in deactivation to S_1 and T_1 faster than any other measurable process. The lines represent the state energies of S_1 and T_1. For simplicity, vibrational levels were omitted from this state energy diagram. S_1 and T_1 are spin isomers and the difference between them is related to the electron occupancies of their highest occupied (HO) molecular orbital and lowest unoccupied (LU) molecular orbital. The Pauli exclusion principle states that no more than two electrons may occupy an orbital and the electrons must have paired spins. In other words, all of the orbitals are filled with two electrons and the two electrons in each orbital must be spin paired. In the excited states, two electrons are orbitally unpaired; that is, each electron is in a different orbital, one in a HO and the other is in a LU. The Pauli principle allows the spins of two electrons to be paired if they do not occupy the same orbital. As a result, either a singlet or a triplet excited state may result from the same electronic configuration of the two electrons in half-occupied orbitals depending on whether the electron spins are opposite or aligned, respectively.

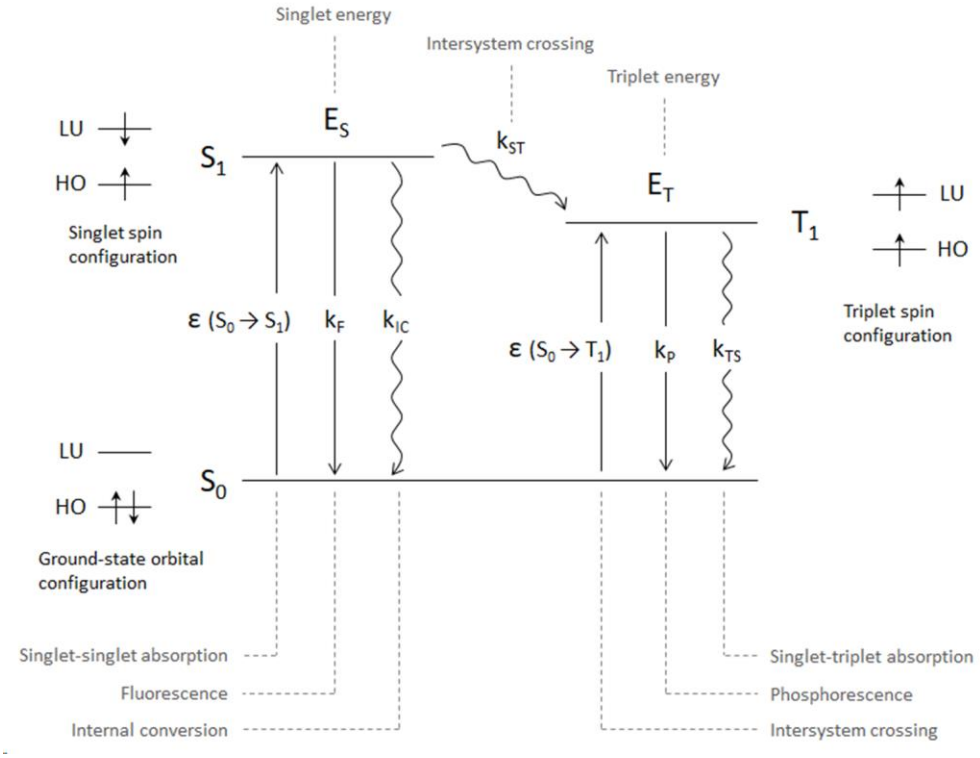

Figure 1-1. State energy-level diagram for organic molecular photochemistry.

T_1 is generated via intersystem crossing (ISC) from S_1. ISC may occur via spin-orbit coupling of S_1 to the upper vibrational levels of T_1, or spin-orbit coupling of S_1 to an upper T_n state followed by rapid $T_n \rightarrow T_1$ internal conversion. The spin-forbidden triplet-singlet emission of photons ($T_1 \rightarrow S_0$), called phosphorescence, is characterized by rate constant k_P. The spin-forbidden radiationless transitions between T_1 and S_0 is characterized by rate constant k_{TS}. The rate constant of ISC, k_{ST}, depends on the energy gap between S_1 and T_1. or the Franck-Condon factor.[28]

1.1.2 Properties of triplet excited states

One of the unique properties of triplet excited states is long lifetime. Phosphorescence is a spin-forbidden process, thus its rate is generally low. The thermal decay from T_1 to S_0 is also hampered because this transition is spin-forbidden. T_1 often has a long lifetime compared to that of S_1, extending into the microsecond or millisecond scale. In contrast to phosphorescence lifetime, fluorescence lifetime is usually of the nanosecond order. Because of the long T_1 lifetime, unique phenomena based on triplet excited states, such as triplet-triplet energy transfer (TTET) and triplet-triplet annihilation (TTA), are observed.

Triplet excited states are easily quenched by molecular oxygen (O_2). In photochemistry, quenching means the energy transfer from an excited molecule to O_2 or a reaction with a molecule in a singlet excited state. O_2 possesses a triplet ground state (T_0 : $^3\Sigma_g^-$) and singlet excited states (S_1 : $^1\Delta_g$ and S_2 : $^1\Sigma_g^+$). The energy gap between $^3\Sigma_g^-$ and $^1\Delta_g$ is ~1274 nm and that of $^3\Sigma_g^-$ and $^1\Sigma_g^+$ is ~762 nm (Figure 1-2).[29,30] Generally, excitation energies of O_2 are lower than those of triplet states of organic compounds. Therefore, transfer of triplet excited energy occurs from the molecules to O_2. As a consequence, O_2 acts as an efficient quencher for many triplet state molecules.[31,32] In addition, superoxide is generated by electron transfer and this reactive oxygen species oxidizes compounds. To avoid these quenching processes, measurements involving triplet states are generally performed under deoxygenated conditions.

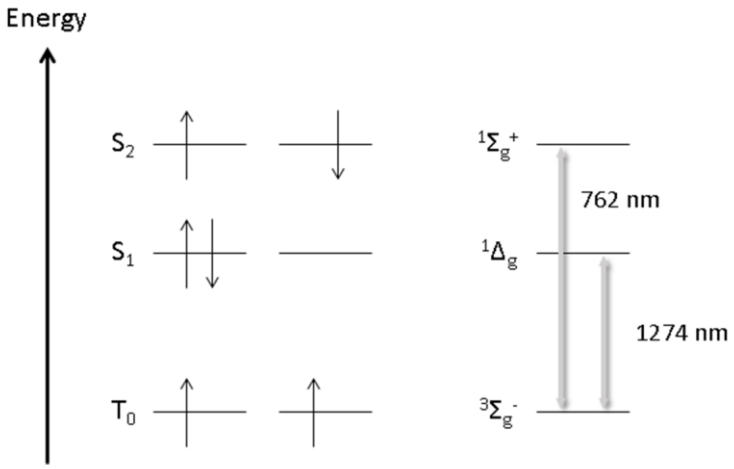

Figure 1-2. Electron configurations, energies and symbols for the three lowest-energy excited states of molecular oxygen.

Magnetism in photo-excited triplet states is another interesting property. A triplet state has a spin quantum number $S = 1$. If no external magnetic field is present and if there is no interaction between electrons, the three spin components designated by the magnetic quantum numbers M_S = +1, 0, and -1, respectively, will be degenerate. Applying magnetic field, $\boldsymbol{H}$, will remove this degeneracy, producing three states. The induced splitting of idealized triplet states is shown in Figure 1-3.[33]

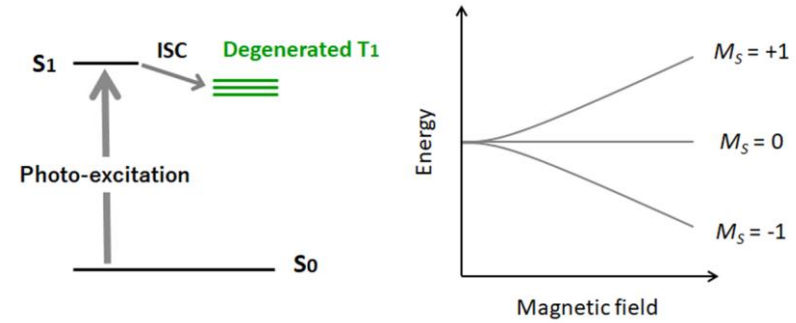

Figure 1-3. Triplet energy levels of an organic compound without accounting for zero-field splitting.

The transitions between $M_S = +1 \leftrightarrow 0$ and $M_S = 0 \leftrightarrow -1$ are magnetic dipole allowed transitions under $\boldsymbol{H}$. The transition between $M_S = 1 \leftrightarrow -1$ should occur at approximately one-half the magnetic field strength of those of the $M_S = 1 \leftrightarrow 0$ and $M_S = 0 \leftrightarrow -1$ transitions; however, the $M_S = 1 \leftrightarrow -1$ transition is magnetic dipole forbidden. The population of each triplet sublevel is selectively generated in applied $\boldsymbol{H}$ and spin polarization patterns depend on the generation process of triplet excited states.[34] The population of triplet sublevels is not at thermal equilibrium; therefore, the polarization does not depend on temperature.

As mentioned above, triplet excited states have intriguing properties. In this thesis, we focused on TTA-UC and triplet-DNP. These phenomena are expected to be useful for biological applications; however, mainly physicists are engaged in basic research at present. The perspective of chemists may open the way to materialization of practical applications that use triplet excited states.

1.2 Triplet-triplet annihilation-based photon upconversion (TTA-UC)

1.2.1 Basics of TTA-UC

TTA-UC is a method to convert lower energy photons into higher energy photons through a sequence of energy transfer steps. TTA-UC is technologically important for a variety of applications ranging from energy to biology. TTA-UC has a competitive advantage over the other upconversion (UC) mechanisms including two-photon absorption[35,36] and multiple excitations of inorganic nanoparticles doped with lanthanide ions (Ln^{3+}).[37-39] The UC mechanisms of two-photon absorption and inorganic nanocrystals are shown in Figure 1-4.

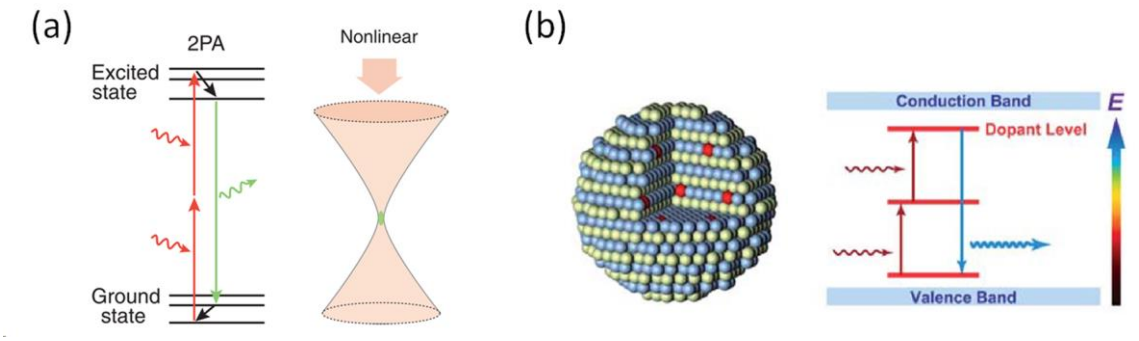

Figure 1-4. (a) Schematic illustration of two-photon absorption with a Jablonski diagram. (b) Schematic illustration of a UC nanoparticles composed of a crystalline host and lanthanide dopant ions embedded in the host lattice (left). Energy-level diagram showing that UC luminescence primarily originates from electron transitions between energy levels of localized dopant ions (right). (a) and (b) were adapted with permission from ref. 35 (NPG) and 39 (RSC), respectively.

Two-photon absorption is a nonlinear absorption process whereby two photons are absorbed simultaneously by a molecule and an electron is promoted from a lower energy level to a higher energy level. The total energy of the transition is equal to the sum of the two photon energies (Figure 1-4a). Two photons should be arrived at a molecule within 0.5 fs to combine their energies to excite the molecule; thus, the two-photon absorption process occurs at a focused point and high-power excitation is required.[35] In contrast, UC nanoparticles generally consist of an inorganic host and Ln^{3+} dopant ions, such as Er^{3+}, Tm^{3+}, and Ho^{3+}, embedded in the host lattice (Figure 1-4b). The strongly shielded f orbitals of the Ln^{3+} dopant ions retain their atomic-like properties. The Ln^{3+} ions commonly have multiple spectroscopically active levels in a host lattice and these active levels can facilitate multiple

excitations for UC processes. However, this system also suffers from the fateful flaw of requiring high excitation intensities (~10 W cm^{-2}) because of its intrinsic low absorption.[9,40]

Recently, there has been remarkable development of TTA-UC with multi-chromophore systems composed of a donor (triplet sensitizer) and acceptor (emitter). Such TTA-UC systems can operate under a non-coherent and low-intensity light source (< 100 mW cm^{-2}).[1-15] As illustrated in Figure 1-5, the TTA-UC mechanism starts with the generation of donor triplets ($T_{1,D}$) by ISC from the photo-generated singlet state ($S_{1,D}$). This triplet excited energy is transferred from donor to acceptor through TTET. Two sensitized acceptor triplets generate a higher-energy excited singlet state through TTA, which consequently produces a delayed fluorescence. The TTET and TTA processes occur by an electron-exchange (Dexter) mechanism, which requires the involved molecules to approach one another within a distance of 1 nm. The long lifetime of triplet states and relatively high absorption coefficient of the donor enable efficient energy transfer and operation under low-energy excitation light.

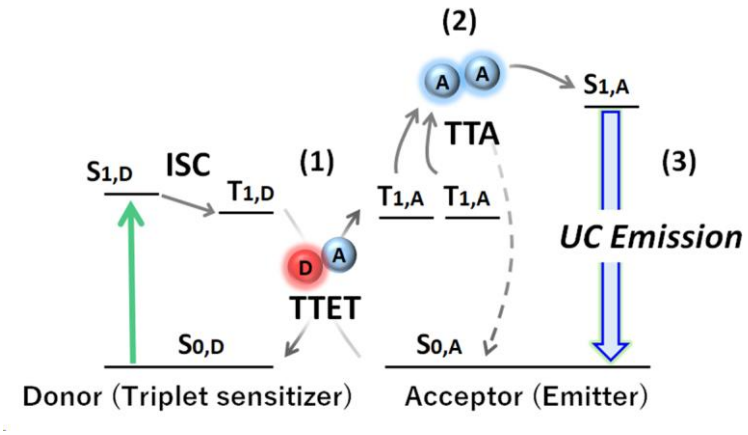

Figure 1-5. Schematic of the triplet-triplet annihilation-based upconversion (TTA-UC) process, showing the energy levels involved in the TTA-UC (S = singlet, T = triplet). The TTA-UC uses a pair of the donor (triplet sensitizer) with high intersystem crossing (ISC) efficiency and acceptor (emitter) with a high fluorescence quantum yield. Green and blue arrows indicate the absorption and emission processes, respectively. First, the sensitizer absorbs the low energy light to form the excited singlet state ($S_{1,D}$). Second, the triplet state ($T_{1,D}$) is populated through ISC. Third, triplet-triplet energy transfer (TTET) from the donor $T_{1,D}$ to the acceptor occurs via the Dexter mechanism. The subsequent diffusion and collision of two excited acceptor triplets ($T_{1,A}$) generate a higher energy excited singlet state ($S_{1,A}$) through TTA. From the excited singlet state ($S_{1,A}$), the upconverted delayed fluorescence is emitted.

The TTA phenomenon was first observed back in the 1960s,[41] but it was only recently that TTA was recognized as a deactivation process that decreases the photocurrent in organic photovoltaic devices. From the beginning of research on TTA-UC, highly efficient solution systems have been developed.[1,2,4,9,42] Next, various organic donor and acceptor pairs including not only visible-to-visible but also near infrared (NIR)-to-visible or visible-to-ultraviolet (UV) TTA-UC systems have been developed.[43-45] During this progresses, a novel triplet sensitization strategy was developed that has attracted much attention. This strategy aims to minimize the energy loss during ISC from S_1 to T_1 of triplet donor molecules, which is fatal for NIR-to-vis and vis-to-UV UC. Molecules displaying thermally activated delayed fluorescence (TADF),[46-48] quantum dots and chalcogenide nanocrystals,[49-54] and direct singlet-triplet (S-T) absorption metal complexes [55,56] have been employed as triplet sensitizers.[57]

Researchers have proposed TTA-UC-based applications (biological applications are described later). Schmidt and co-workers have reported a TTA-UC-enhanced dye-sensitized solar cell.[58] A solution-based UC system is contained within an encapsulated chamber on the back of the solar cell. Hanson et al. proposed a different strategy that entailed introducing self-assembled bilayers of sensitizer and acceptor molecules on a metal oxide substrate as a step toward an electronically coupled TTA-UC solar cell.[12] Castellano and colleagues revealed that it is possible to generate hydrogen using TTA-UC and Monguzzi and co-workers demonstrated enhanced performance in a photo-catalytic water-splitting cell using a TTA-UC system.[59,60] In the latter case, a light upconverter was able to harvest sub-bandgap photons and inject this additional energy into the photocatalyst through efficient light UC. In addition, Campos et al. achieved various photo-redox transformations under infrared radiation with TTA-UC materials were reported.[61]

As mentioned above, many triplet sensitizers and emitters have been developed and a wide variety of applications based on TTA-UC have been proposed. For practical applications, along with the conversion wavelength, excitation intensity, and quantum yield are important parameters used to characterize TTA-UC systems.

1.2.2 Parameters of TTA-UC

In general, the quantum yield is defined as the ratio of absorbed photons to emitted photons, and thus the maximum quantum yield (Φ_{UC}) of the bimolecular TTA-UC process is 50%. However, many reports multiply this value by two to set maximum efficiency at 100%. To avoid the confusion between these different definitions, the UC efficiency is written as $\Phi_{UC}{}'$ (= $2\Phi_{UC}$) when its maximum is normalized to be 100%,

$$\Phi_{UC}{}' = 2\Phi_{UC} = f\Phi_{ISC}\Phi_{TTET}\Phi_{TTA}\Phi_{F,A} \qquad (equation\ 1)$$

where Φ_{ISC}, Φ_{TTET}, Φ_{TTA} and $\Phi_{F,A}$ represent the quantum efficiencies of donor ISC, donor-to-acceptor TTET, TTA, and acceptor fluorescence, respectively, and f is the statistical probability of obtaining the singlet excited state after the annihilation of two triplets.[2,4]

The efficiency of a multi-exciton TTA process depends on the concentration of excited species; namely, the excitation intensity. From the viewpoint of practical applications, the excitation intensity is one of the most important parameters. Monguzzi and co-workers proposed a figure-of-merit parameter called the threshold excitation intensity, I_{th}, at which half of the produced triplets are used for TTA (Figure 1-6).[62] I_{th} is the excitation light intensity at which Φ_{TTA} is 0.5, which is derived from the relationship between the UC emission intensity and the excitation light intensity.

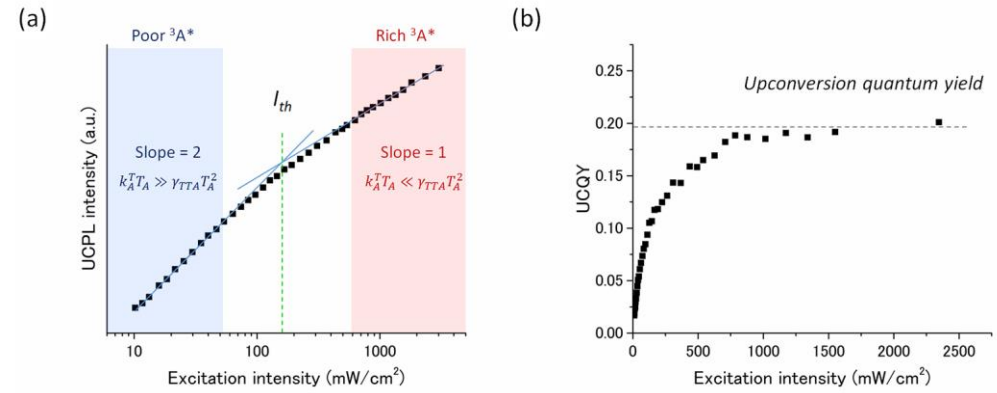

Figure 1-6. Typical excitation intensity of upconversion in a triplet-triplet annihilation-based upconversion mechanism. (a) Upconversion emission intensity as a function of excitation intensity. (b) Upconversion quantum yield as a function of excitation intensity.

At low incident light intensity, the emission from bimolecular annihilation processes exhibits quadratic dependence on the excitation intensity. In the high-energy excitation regime, the TTA process becomes dominant for emitter triplet decay, resulting in quasilinear dependence, which is derived from the following equations,[62,63]

$$\frac{\partial T_D}{\partial t} = \alpha I_{exc} - k_D^T T_D - k_{tr} T_D \qquad (equation\ 2-1)$$

$$\frac{\partial T_A}{\partial t} = k_{tr} T_D - k_A^T T_A - \gamma_{TTA} T_A^2 \qquad (equation\ 2-2)$$

$$\frac{\partial S_A}{\partial t} = 0.5 f \gamma_{TTA} T_A^2 - k_A^S S_A \qquad (equation\ 2-3)$$

where T_D and T_A represents the populations of the donor (D) and acceptor (A) excited triplets, respectively, and S_A is acceptor excited singlet states, α is the absorption coefficient of the donor, and I_{exc} is excitation intensity. γ_{TTA} is the rate constant of the TTA, and k is the decay rate constant, and the subscripts D and A represent donor and acceptor, respectively. At low excitation power, TTA becomes negligible with respect to the acceptor spontaneous radiative and nonradiative decay of the acceptor, which is the main triplet deactivation channel; that is, $k_A^T T_A \gg \gamma_{TTA} T_A^2$. (region with a blue background in Figure 1-6a). At low excitation power, the concentration of S_A in the steady state can be described as a function of the excitation intensity as follows,

$$S_A = 0.2 \frac{\gamma_{TTA}}{k_A^S} \left[\frac{\frac{k_{tr}}{k_A^T}}{k_D^T + k_{tr}} \right]^2 [\alpha I_{exc}]^2 \propto I_{exc}^2 \qquad (equation\ 3)$$

According to equation 3, the UC emission intensity is proportional to the square of the excitation intensity; thus, the slope of their double logarithmic plots is two.

By contrast, in the high excitation regime, the acceptor triplet decay channel is TTA because $\gamma_{TTA}T_A^2$ becomes larger than $k_A^T T_A$ ($\gamma_{TTA}T_A^2 \gg k_A^T T_A$) (region with a red background regime in Figure 1-6a),

$$S_A = 0.2\frac{1}{k_A^S}\left[\frac{k_{tr}}{k_D^T + k_{tr}}\right]^2 \alpha I_{exc} \propto I_{exc} \qquad (equation\ 4)$$

Equation 4 shows that S_A becomes proportional to the excitation intensity, that is, the slope of the double logarithmic plots becomes one. The I_{th} can be obtained from the intersection of these lines and represented by the following equation,

$$I_{th} = \frac{1}{\alpha\Phi_{TTET}\gamma_{TTA}\tau_{A,T}^2} = \frac{1}{8\pi a_0 \alpha\Phi_{TTET}D_T\tau_{A,T}^2} \qquad (equation\ 5)$$

where τ_A is the lifetime of the acceptor triplet and α is the absorption coefficient of the donor. In addition, this formula can be re-expressed by replacing γ_{TTA} with the diffusion constant D_T because $\gamma_{TTA} = 8\pi a_0 D_T$, where a_0 is the annihilation distance between emitter triplets.[64] To achieve a low I_{th} value, large sensitizer absorbance, efficient TTET, fast triplet diffusion, and long emitter triplet lifetime are required.

The most efficient TTA-based UC has been achieved for donor–acceptor pairs molecularly dissolved in organic solvents because they allow fast diffusion of the excited molecules. Therefore, I_{th} with a few mW cm^{-2} have been achieved, which is comparable intensity to that of sunlight.

1.2.3 Oxygen quenching and TTA-UC in aqueous media

Oxygen quenching

There is a fatal problem in solution-state TTA-UC. As mentioned in section 1.1.2, O_2 efficiently quenches triplet excited states. Consequently, traditional organic bimolecular TTA-UC systems work efficiently only in oxygen-free solutions (O_2 concentration below 1 ppm).[65] Quenching is mainly caused by the energy transfer between the organic molecule triplet state and ground state of O_2, leading to the formation of singlet oxygen. Singlet oxygen is a highly reactive species that can oxidize the photoactive molecules, which leads to further loss of efficiency. Therefore, methods to protect triplets form O_2 have been actively developed (Figure 1-7).[32] There are two main types of protection strategies. One is the addition of sacrificial reducing agents (scavenger). Oleate derivatives are frequently used as an oxygen scavenger because they are common biocompatible compounds.[40,66,67] Unsaturated phosphite ester,[68] sulfite,[69] sulfide derivatives,[70] and limonene,[71] have also been used as sacrificial oxygen scavengers. The second strategy is using a specific solid polymer or viscous liquid as a matrix.[3,31,32] However, both approaches hinder molecular diffusion and have limited ability to improve the UC performance. (equation 5)

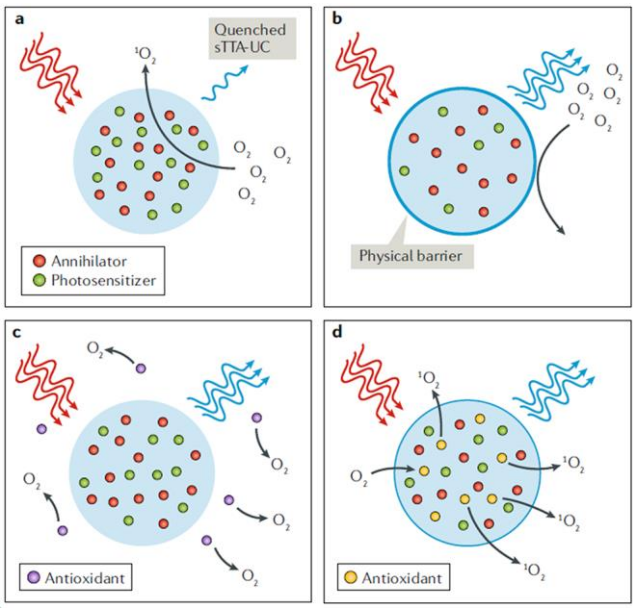

Figure 1-7. Chemical strategies to prevent quenching of TTA-UC by triplet or singlet oxygen. (a) Quenching of TTA-UC emission by oxygen via singlet oxygen generation. (b) Physical barrier that prevents diffusion of O_2. (c) Exogeneous antioxidants quench ground-state or singlet oxygen. (d) Antioxidants are added to a nanoparticle. Adapted with permission from ref. 32, NPG.

TTA-UC in aqueous media

TTA-UC is a useful light conversion method for biological applications. In bioimaging, upconverted emission can be easily isolated from the excitation light and enhance the signal-to-noise ratio. In addition, deep tissue penetration is also required for imaging and phototherapy. Red or NIR light can achieve deeper tissue penetration (up to 1 cm) compared with that of green, blue or UV light (~500 μm).[72] Moreover, there is a possibility that high-energy blue or UV light damages cells, whereas red and NIR are considered safer alternatives.[73] In optogenetics, most proteins respond to light with a wavelength of < 500 nm.[74] Considering these points, TTA-UC has great advantages because low-energy excitation with non-coherent and weak intensity can be used and higher energy light is generated.

Although most of the studies on TTA-UC have been carried out in organic media, development of TTA-UC systems that operate in aqueous media is important because such systems are expected to find interdisciplinary applications in the area of life science including bioimaging, sensing, drug delivery, and photodynamic therapy. To date, TTA-UC systems designed for use in aqueous media include polymer nanocapsules or microcapsules with an oil core,[3,66,75,76] and rubbery or rigid polymer nanoparticles.[65,77,78]

Although the TTA-UC systems that work in aqueous media under ambient condition are limited, in vitro or in vivo demonstrations have been reported.[40,66,76,79-81] Fuyou Li and co-workers demonstrated the first report of TTA-UC bioimaging in mice with singlet oxygen scavengers. They prepared nanocapsules containing reductive linoleic acid and oleic acid which have unsaturated bonds. The oxygen scavenger system enabled realization of an air-stable TTA-UC system (Figure 1-8).[66]

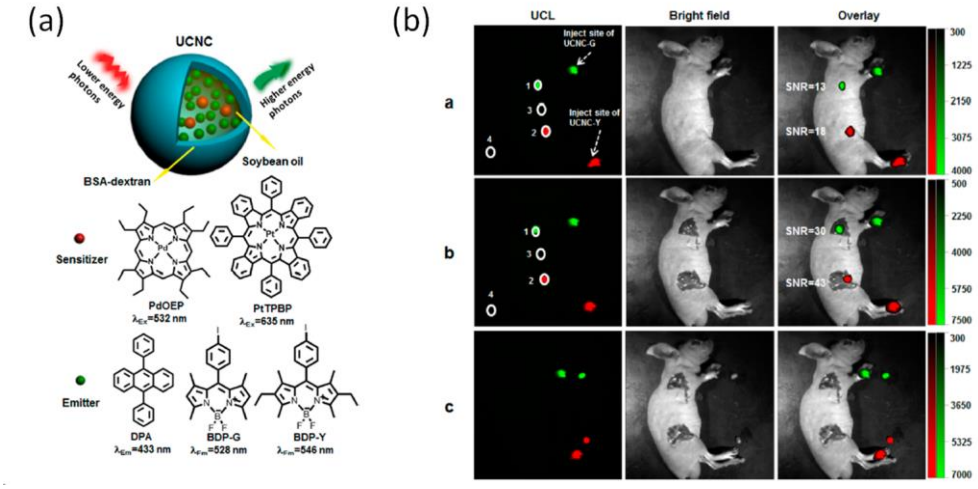

Figure 1-8. (a) Schematic illustration of the triplet-triplet annihilation-based upconversion (TTA-UC) process of the upconversion nanocapsules (UCNC), and chemical structures of sensitizers (PdOEP and PtTPBP) and annihilators (DPA, BODIPY derivatives). (b) a: In vivo, b: in situ, and c: ex vivo upconversion luminescence lymphatic imaging of a living mouse 30 min after injection of UCNC-G and UCNC-Y (20 μL) in fore and hind paws, respectively (λ_{ex} = 635 nm, λ_{UC} = 530 ± 25 nm, excitation power density = 12.5 mW cm^{-2}). Adapted with permission from ref. 66, ACS.

Another strategy to achieve aqueous-based TTA-UC systems is using a viscous matrix to suppress O_2 diffusion. For example, Kim and co-workers have reported an UC system consisting of chromophores encapsulated in a hexadecane/polyisobutylene mixture that operates in aerated water.[3,82] Monguzzi and colleagues demonstrated a micelle system loaded with hydrophobic UC dyes that worked in aerated water.[83] They found that the donor concentration affected the UC efficiency. The vesicle systems reported by Bonnet et al. and König et al. were demonstrated in deaerated conditions.[7,84]

While these approaches allow for air-stable UC emission with reasonably high efficiency, the limited diffusion of large dye molecules in these viscous matrices is forecast to cause potential issues for further developments. Overall, these results indicated that there is currently no clear design strategy to realize efficient TTA-UC in aqueous systems.

1.2.4 Overview of this thesis on TTA-UC

The main focus of this thesis about TTA-UC is to establish air-stable aqueous TTA-UC systems and methodology to achieve oxygen tolerance in aqueous solution phase by introducing the self-assembly concept.

Chapter 2 describes the first example of an air-saturated aqueous triplet energy migration-based TTA-UC system. We made the assume that ordered aqueous molecular self-assemblies with extended molecular networks containing interactions such as hydrogen bonding can prevent the intrusion of O_2 from the bulk water into the hydrophobic interior of the molecular assemblies. As a proof of concept, a novel amphiphilic acceptor is designed. Co-assemblies of this acceptor with an anionic donor show efficient triplet energy migration-based TTA-UC emission in deaerated aqueous dispersions, which is largely preserved even in the air-saturated aqueous systems (Figure 1-9).

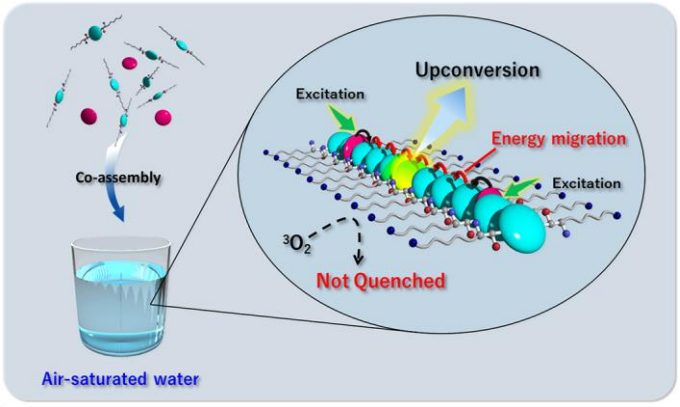

Figure 1-9. Schematic of the aqueous triplet energy migration-based TTA-UC system. The co-assembly of donor (pink) and acceptor (blue) in aerated water showed UC emission. Oxygen quenching was effectively avoided because the intermolecular hydrogen bonding networks limited oxygen diffusion in the acceptor assemblies.

In chapter 3, a method to avoid oxygen quenching in aqueous media is discussed (Figure 1-10). This chapter introduces a simple strategy to achieve air-stable TTA-UC in water. Amphiphilic acceptor molecules and anions with long alkyl chains are co-assembled in water. The assemblies with hydrophobic donor maintained 80% of their TTA-UC efficiency in aqueous dispersion compared with that under deaerated conditions. This work demonstrates the new promising potential of supramolecular chemistry to achieve photophysical and photochemical functions with oxygen-sensitive species.

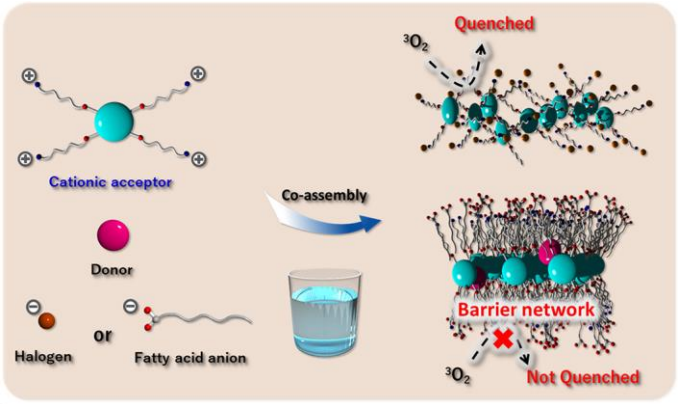

Figure 1-10. Schematic illustration of the aqueous TTA-UC molecular system and its oxygen-barrier properties. Addition of anion with long alkyl chains to cationic acceptor self-assemblies produced hydrophobic ion pairs. The resultant structural transformation into dense molecular assemblies leads to interfacial supramolecular crowding, which efficiently shielded the triplet excited states from quenching by dissolved oxygen in water.

1.3 Triplet dynamic nuclear polarization (triplet-DNP)

1.3.1 Fundamentals of nuclear magnetic resonance

Since its introduction over 70 years ago,[85,86] nuclear magnetic resonance (NMR) spectroscopy has established itself as one of the most widely used analytical tools in the chemical sciences, providing an element-specific and nondestructive measurement technique that is applicable to many phases. In contrast to other spectroscopic techniques, NMR experiments are performed in the MHz radio-frequency region, and the transitions between nuclear spin energy levels are quite small. Thus, the NMR experiments causes only a slight perturbation of the systems. However, the sensitivity of NMR spectroscopy is intrinsically limited by the low nuclear polarization under ambient conditions, is in accordance with Boltzmann's law. In the case of species with nuclear spins $I = 1/2$ such as ^{1}H, ^{13}C, ^{19}F, and electrons, the thermal equilibrium spin polarization (P_{th}) is defined by the following equation,

$$P_{th} = \frac{N\uparrow - N\downarrow}{N\uparrow + N\downarrow} = \frac{exp\left(\frac{\gamma\hbar B_0}{2kT}\right) - exp\left(-\frac{\gamma\hbar B_0}{2kT}\right)}{exp\left(\frac{\gamma\hbar B_0}{2kT}\right) + exp\left(-\frac{\gamma\hbar B_0}{2kT}\right)} = \tanh\left(\frac{\gamma\hbar B_0}{2kT}\right) \quad (equation\ 6)$$

where $N\uparrow$ and $N\downarrow$ are the populations of the eigenstates $|+\frac{1}{2}>$ and $|-\frac{1}{2}>$, respectively, γ is the gyromagnetic ratio of the nuclear or electron spin, $\hbar$ is the Dirac's constant, B_0 is the magnetic field, k is the Boltzmann constant, and T is the temperature.[87]

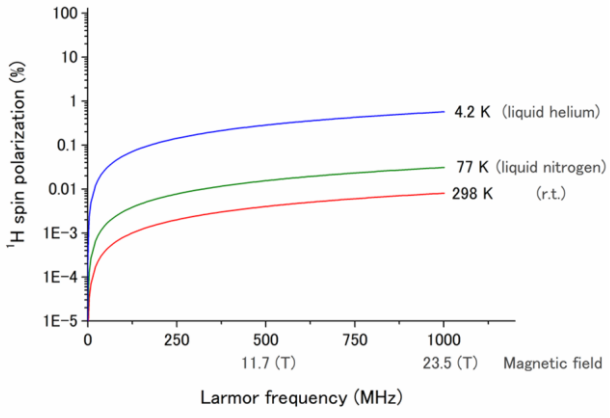

Figure 1-11. ^{1}H spin polarization in thermal equilibrium as a function of magnetic field.

According to the equation 6, ^{1}H spin polarization depends on temperature and magnetic field (Figure 1-11). We often use NMR spectroscopy to identify molecular structure at the Larmor frequency of 500 MHz (magnetic field of 11.7 T); however, ^{1}H spin polarization value at 298 K is no more than 0.004%. Therefore, the sensitivity of NMR spectroscopy is low.

1.3.2 Nuclear spin polarization

The definition of spin polarization is schematically illustrated in Figure 1-12. Hyperpolarization means the large difference of abundance ratio between $|+\frac{1}{2}>$ and $|-\frac{1}{2}>$ compared to that of the thermal equilibrium state.

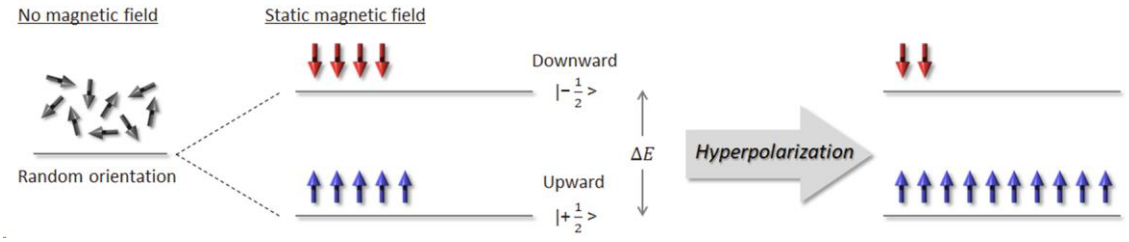

Figure 1-12. Schematic illustration of the Zeeman effect and hyperpolarization.

The intensity of NMR signals can be enhanced by several orders of magnitude by using the hyperpolarization of different molecules.[88] *Para*-hydrogen-based hyperpolarization, which is called *para*-hydrogen-induced polarization (PHIP) has been reported.[89,90] In PHIP, the singlet order of a *para*-hydrogen molecule is reacted with an asymmetric unsaturated bond of a precursor molecule. Then, the symmetry of *para*-hydrogen is broken and observable polarization is obtained. More recently, it has been shown that *para*-hydrogen can be used to hyperpolarize a growing range of organic substrates by establishing of a simple and reversible interaction at a metal center. In this process, the substrate and *para*-hydrogen exchange freely in solution with those on the complex, and the concentration of hyperpolarized product builds up in solution as a result. This process has been termed signal amplification by reversible exchange (SABRE).[91-93] Spin exchange optical pumping (SEOP) can be used to generate hyperpolarized noble gases (^{3}He, ^{83}Kr, and ^{129}Xe).[94,95] In particular, ^{129}Xe is inert and easily encapsulated in cage compounds, which induces a large chemical shift. The potential of hyperpolarized noble gases as a biomarker has been demonstrated by the hyperpolarized chemical exchange saturation transfer (hyperCEST) approaches.[96,97] However, this method is restricted by the limited number of substrates that can be hyperpolarized.

DNP is another hyperpolarization method and its basic concept was reported in 1978.[98] Larsen and co-workers reported the dissolution DNP technique.[99] This technique requires the presence of unpaired electrons (e.g., organic free radicals) because the thermal electron spin polarization is 660 times higher than that of ^{1}H (equation 6). The organic free radicals are doped into a glass matrix and then polarization transfer from electrons to ^{1}H nuclei is conducted at cryogenic temperature. Importantly, to obtain high polarization enhancement of over 660 times, very low temperature is necessary because the electron spin polarization also depends on the Boltzmann distribution. Dissolution DNP involves hyperpolarization in the solid state at around 1 K and then subsequent conversion into a liquid by rapid dissolution through heating. The development of dissolution DNP has opened up to new possibilities, such as analysis of protein by proton exchange.[100-106] However, the dissolution DNP technique has intrinsic problems. One is that extremely low temperature is essential in order to generate hyperpolarization. Second, the resolution of NMR spectroscopy can be degraded by the presence of paramagnetic species.[107] Finally, the spin-lattice relaxation time (T_1) of a glassy matrix is generally short compared to that of crystals.[108,109] However, matrix vitrification of matrix is needed to solubilize the polarizing agent and substrates.

1.3.3 Basics of triplet-DNP

A solution to these issues has been proposed that involves using thermal non-equilibrium electron spin polarization in photo-excited triplet states, which is called triplet DNP. Large electron spin polarization in the excited triplet state sublevels is produced regardless of temperature and magnetic field (Figure 1-13),[110] and the paramagnetic species (triplet excited state) is deactivated on the microsecond time scale. A typical scheme of triplet DNP is shown in Figure 1-14.

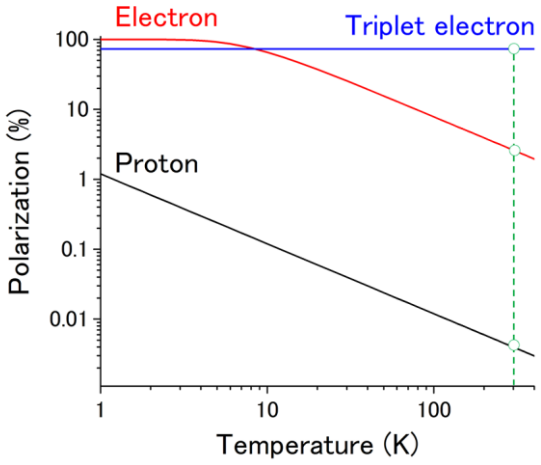

Figure 1-13. Nuclear spin polarization in thermal equilibrium under a magnetic field in 11.7 T as a function of temperature. The blue line represents the thermal non-equilibrium triplet state of pentacene.

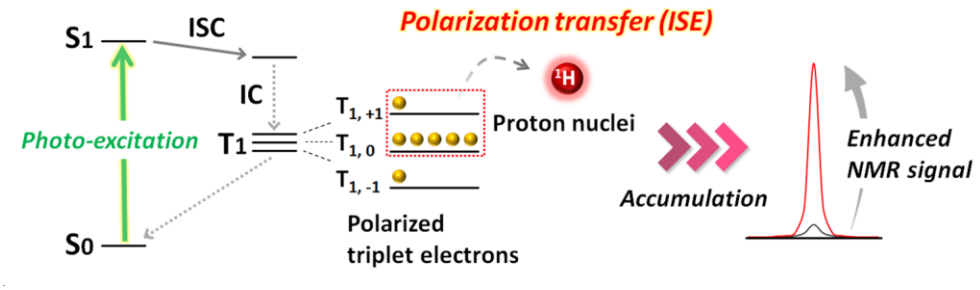

Figure 1-14. Typical scheme of triplet-DNP. Photo-excitation of a polarizing agent is followed by spin-selective intersystem crossing (ISC). The resulting large electron spin polarization is transferred to the nuclear spin polarization through the integrated solid effect (ISE).

A triplet polarizing agent absorbs excitation light and the subsequent spin-selective ISC generates the large electron spin polarization in the triplet excited state sublevels. This polarization is effectively transferred to the nuclear spins by the integrated solid effect (ISE), followed by polarized spin diffusion to the bulk.[111,112] To induce the ISE, a field sweep and microwave irradiation near the transition frequency between the triplet sublevels are simultaneously applied. The inhomogeneously-broadened triplet spins are adiabatically swept to transfer the hyperpolarization. Finally, the signal enhancement is achieved.

1.3.4 Parameters of triplet-DNP

Enhancement factor and spin polarization

The enhancement factor (ε) of triplet-DNP was calculated by comparing the integrated intensities of the hyperpolarized ^{1}H NMR signal of each sample after a triplet-DNP sequence with the ^{1}H NMR signal of reference sample in thermal equilibrium,[113]

$$\varepsilon = \frac{N_{ref}}{N_{DNP}} \frac{T_{DNP}}{T_{ref}} \frac{g_{ref}}{g_{DNP}} \frac{E_{DNP}}{E_{ref}} \qquad (equation\ 7)$$

where N is the number of ^{1}H spins, T is temperature, and g is the receiver gain, and E is the recorded signal voltage. The ^{1}H spin polarization (P) was also determined by

$$P = \varepsilon \tanh \frac{\gamma \hbar B}{2kT} \qquad (equation\ 8)$$

where γ, $\hbar$, B, k, and T are the gyromagnetic ratio, reduced Planck constant, magnetic field, Boltzmann constant, and temperature, respectively.

Buildup behavior

The buildup behavior of ^{1}H spin polarization is shown in Figure 1-15 and given by the following equation,[113]

$$\frac{dP_H(t)}{dt} = \frac{1}{T_B}[P_e - P_H(t)] + \frac{1}{T_1}[P_H(t) - P_{H\,thermal}] \qquad (equation\ 9)$$

where P_H, P_e, $P_{H\,thermal}$, t, T_B, and T_1 are the spin polarization of ^{1}H, the spin polarization of electrons in the photo-excited triplet state, the spin polarization of ^{1}H in the thermal equilibrium state, time, the buildup rate constant and spin-lattice relaxation time, respectively. $P_{H\,thermal}$ was negligible (0.0002%) at 298 K and in 0.68 T. Equation 9 was solved as

$$P_H(t) = P_f\left\{1 - exp\left[-\left(\frac{1}{T_B} + \frac{1}{T_1}\right)\right]t\right\} \qquad (equation\ 10)$$

and P_f is defined by

$$P_f = \frac{1}{1 + \frac{T_B}{T_1}}P_e \qquad (equation\ 11)$$

For simplification, in some cases the buildup curve is fitted by A[1-exp(-t/T)] + B. Importantly, these equations are completed considering the fast diffusion limit condition. That is, the ^{1}H spin diffusion rate is much faster than the feasible triplet-DNP repetition rate.[87]

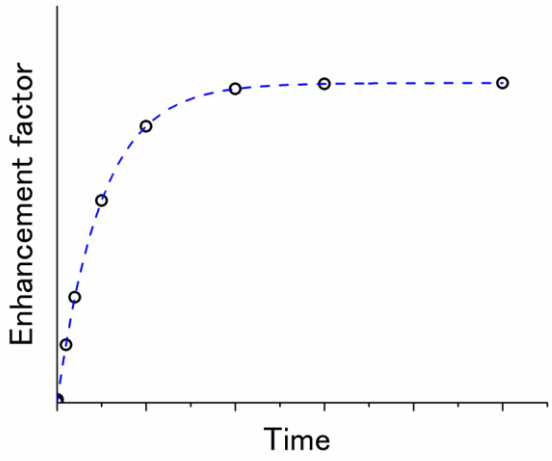

Figure 1-15. Buildup curve of the nuclear spin polarization. The broken line is a fitting curve with the following equation, A[1-exp(-t/T)] + B.

1.3.5 Current situation of triplet-DNP

Hawser and co-workers demonstrated the first triplet-DNP systems.[114,115] In 1990, Wenchebach et al. published a breakthrough report with an ISE sequence at room temperature.[16] They used pentacene as a triplet polarizing agent and naphthalene as a matrix and enhanced the naphthalene ^{1}H polarization by 5500 times. Since the first report of room-temperature triplet-DNP, only pentacene and pentacene derivatives have been used as triplet polarizing agents, whereas a number of matrixes have been developed.[16,18,20,21,87,113,116]

Despite its potential, the application of triplet-DNP has been limited by the instability of the pentacene skeleton under the ambient conditions.[117,118] Therefore, doping in an air-stable solid matrix or deoxygenated conditions is necessary at present. From the viewpoint of analysis related to biomolecules, an environment close to that of living cells is desirable;[119] in other words, generation of hyperpolarization in aqueous media (pure water or buffer). Tateishi and co-workers have been reported ^{1}H hyperpolarization of water molecules at 90 K by employing glassy matrix composed of ethanol-d6 : water = 80:20 (v/v) doped with 0.1 mM of 6,13-diphenylpentacene.[21] However, it was difficult to increase the proportion of water because of the aggregation of triplet polarizing agents. To date, triplet-DNP research has mainly focused on clarifying the basics of this phenomenon; the design and synthesis of novel triplet polarizing agents have not been reported.

1.3.6 Overview of the study of triplet-DNP

The research presented in this thesis concentrates mainly on the development of novel triplet polarizing agents for triplet DNP as first step. Then, to establish aqueous triplet DNP systems, the molecular design of water-soluble triplet polarizing agents is discussed.

Chapter 4 describes the potential of diaza-substituted acenes as air-stable and high-performance triplet polarizing agents (Figure 1-16). The introduction of electron-withdrawing diaza substituents onto pentacene and tetracene lowers the lowest unoccupied molecular orbital level and provides much improved stability under the ambient conditions. Importantly, the diaza-substituted pentacene and tetracene offer similar, or even slightly better, ^{1}H NMR signal enhancement to that of pentacene in a prototypical triplet-DNP test using *p*-terphenyl crystals. This work removes one of the largest obstacles in the use of triplet-DNP for the hyperpolarization of biological molecules.

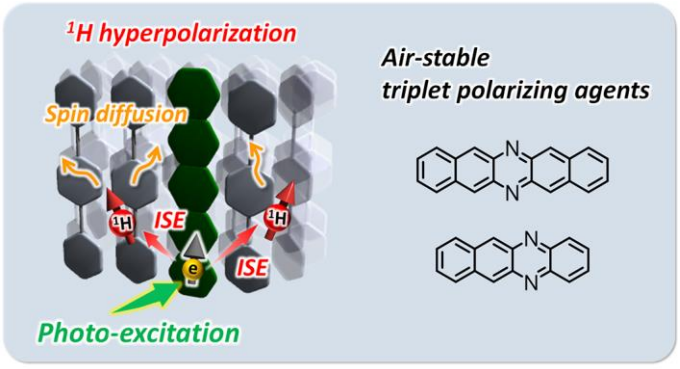

Figure 1-16. Schematic illustration of the triplet-DNP system and the chemical structure of triplet-DNP polarizing agents.

In chapter 5, we demonstrated the first example of ^{1}H NMR signal enhancement in crystalline ice by triplet DNP with a novel water-soluble triplet polarizing agent which has carboxylic acid functionalities (Figure 1-17). The ion-pairing of a triplet polarizing agent with carboxylic acid groups and hydrophilic and bulky amine is a simple method to achieve dispersibility even in an ice matrix. This concept of hyperpolarization in ice provides an important initial step towards the hyperpolarization of various biomolecules in water and even in vivo.

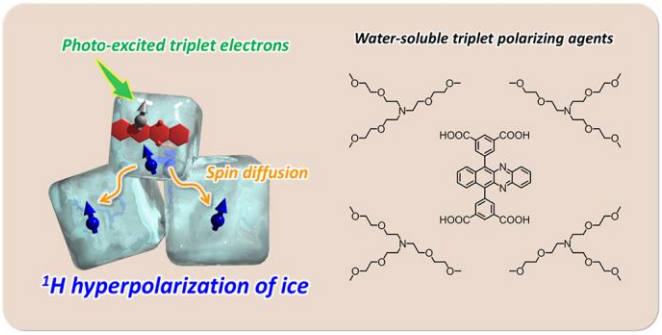

Figure 1-17. Schematic illustration of hyperpolarization by triplet-DNP in a pure ice state.

1.4 Conclusion

Modern chemistry offers the advantage of enabling the design of a variety of molecular units, thus appropriate molecular design opens up possibilities to achieve materialization. And one of the most promising method to realize functions is self-assembly. In self-assembly, molecules spontaneously organize into ordered assemblies driven by non-covalent intermolecular forces.

Water has unique properties and is an excellent solvent for not only small and polar molecules but also solutes such as oxygen, amino acids, and proteins. Water participates in strong interactions, forming hydrogen bonds with other molecules including water molecules. A molecular design to suppress the strong hydrogen bonding between water molecules is necessary to expand the applications of functional materials into aqueous media. In particular, it is important to control the interfaces between water and functional molecules to establish functional materials. In this thesis, the concept of developing self-assembled molecular systems with the ability to work in aqueous media is investigated.

References

(1) Baluschev, S.; Miteva, T.; Yakutkin, V.; Nelles, G.; Yasuda, A.; Wegner, G. *Phys. Rev. Lett.* **2006,** *97*, 143903.

(2) Singh-Rachford, T. N.; Castellano, F. N. *Coord. Chem. Rev.* **2010,** *254*, 2560-2573.

(3) Kim, J.-H.; Kim, J.-H. *J. Am. Chem. Soc.* **2012,** *134*, 17478-17481.

(4) Monguzzi, A.; Tubino, R.; Hoseinkhani, S.; Campione, M.; Meinardi, F. *Phys. Chem. Chem. Phys.* **2012,** *14*, 4322-4332.

(5) Simon, Y. C.; Weder, C. *J. Mater. Chem.* **2012,** *22*, 20817-20830.

(6) Börjesson, K.; Dzebo, D.; Albinsson, B.; Moth-Poulsen, K. *J. Mater. Chem. A* **2013,** *1*, 8521-8524.

(7) Askes, S. H. C.; Bahreman, A.; Bonnet, S. *Angew. Chem. Int. Ed.* **2014,** *53*, 1029-1033.

(8) Schulze, T. F.; Schmidt, T. W. *Energy Environ. Sci.* **2015,** *8*, 103-125.

(9) Zhou, J.; Liu, Q.; Feng, W.; Sun, Y.; Li, F. *Chem. Rev.* **2015,** *115*, 395-465.

(10) Yanai, N.; Kimizuka, N. *Chem. Commun.* **2016,** *52*, 5354-5370.

(11) Fan, C.; Wu, W.; Chruma, J. J.; Zhao, J.; Yang, C. *J. Am. Chem. Soc.* **2016,** *138*, 15405-15412.

(12) Hill, S. P.; Hanson, K. *J. Am. Chem. Soc.* **2017,** *139*, 10988-10991.

(13) Huang, Z.; Tang, M. L. *J. Am. Chem. Soc.* **2017,** *139*, 9412-9418.

(14) Han, J.; Jiang, Y.; Obolda, A.; Duan, P.; Li, F.; Liu, M. *J. Phys. Chem. Lett.* **2017,** *8*, 5865-5870.

(15) Xu, W.; Liang, W.; Wu, W.; Fan, C.; Rao, M.; Su, D.; Zhong, Z.et al. *Chem. - Eur. J.* **2018,** *24*, 16677-16685.

(16) Henstra, A.; Lin, T.-S.; Schmidt, J.; Wenckebach, W. T. *Chem. Phys. Lett.* **1990,** *165*, 6-10.

(17) Iinuma, M.; Takahashi, Y.; Shaké, I.; Oda, M.; Masaike, A.; Yabuzaki, T.; Shimizu, H. M. *J. Magn. Reson.* **2005,** *175*, 235-241.

(18) Tateishi, K.; Negoro, M.; Kagawa, A.; Kitagawa, M. *Angew. Chem. Int. Ed.* **2013,** *52*, 13307-13310.

(19) Tateishi, K.; Negoro, M.; Nishida, S.; Kagawa, A.; Morita, Y.; Kitagawa, M. *Proc. Natl. Acad. Sci. USA* **2014,** *111*, 7527-7530.

(20) Negoro, M.; Kagawa, A.; Tateishi, K.; Tanaka, Y.; Yuasa, T.; Takahashi, K.; Kitagawa, M. *J. Phys. Chem. A* **2018,** *122*, 4294-4297.

(21) Tateishi, K.; Negoro, M.; Nonaka, H.; Kagawa, A.; Sando, S.; Wada, S.; Kitagawa, M.et al. *Phys. Chem. Chem. Phys.* **2019,** *21*, 19737-19741.

(22) Smith, M. B.; Michl, J. *Chem. Rev.* **2010,** *110*, 6891-6936.

(23) Walker, B. J.; Musser, A. J.; Beljonne, D.; Friend, R. H. *Nat. Chem.* **2013,** *5*, 1019-1024.

(24) Chen, S.; Deng, L.; Xie, J.; Peng, L.; Xie, L.; Fan, Q.; Huang, W. *Adv. Mater.* **2010,** *22*, 5227-5239.

(25) Uoyama, H.; Goushi, K.; Shizu, K.; Nomura, H.; Adachi, C. *Nature* **2012,** *492*, 234-238.

(26) Doherty, M. W.; Manson, N. B.; Delaney, P.; Jelezko, F.; Wrachtrup, J.; Hollenberg, L. C. L. *Phys. Rep.* **2013,** *528*, 1-45.

(27) Schirhagl, R.; Chang, K.; Loretz, M.; Degen, C. L. *Annu. Rev. Phys. Chem.* **2014,** *65*, 83-105.

(28) Nicholas J. Turro; Ramamurthy, V.; Scaiano, J. C. *Modern Molecular Photochemistry of Organic Molecules*; University Science Books, U.S.: Sausalito, California, 2010.

(29) Dam, N.; Keszthelyi, T. s.; Andersen, L. K.; Mikkelsen, K. V.; Ogilby, P. R. *J. Phys. Chem. A* **2002,** *106*, 5263-5270.

(30) Schweitzer, C.; Schmid, R. *Chem. Rev.* **2003,** *103*, 1685−1757.

(31) Filatov, M. A.; Baluschev, S.; Landfester, K. *Chem. Soc. Rev.* **2016,** *45*, 4668-4689.

(32) Askes, S. H. C.; Bonnet, S. *Nat. Rev. Chem.* **2018,** *2*, 437-452.

(33) S. P. McGlynn; T. Azumi; Kinoshita, M. *Molecular spectroscopy of the triplet state*; Prentice-Hall, U.S.: Englewood cliffs, New Jersey, 1969.

(34) Bayliss, S. L.; Kraffert, F.; Wang, R.; Zhang, C.; Bittl, R.; Behrends, J. *J. Phys. Chem. Lett.* **2019,** *10*, 1908-1913.

(35) Helmchen, F.; Denk, W. *Nat. Methods* **2005,** *2*, 932-940.

(36) Pawlicki, M.; Collins, H. A.; Denning, R. G.; Anderson, H. L. *Angew. Chem. Int. Ed.* **2009,** *48*, 3244-3266.

(37) Auzel, F. *Chem. Rev.* **2004,** *104*, 139−173.

(38) Wang, F.; Liu, X. *Chem. Soc. Rev.* **2009,** *38*, 976-989.

(39) Wang, F.; Banerjee, D.; Liu, Y.; Chen, X.; Liu, X. *Analyst* **2010,** *135*, 1839-1854.

(40) Huang, L.; Zhao, Y.; Zhang, H.; Huang, K.; Yang, J.; Han, G. *Angew. Chem. Int. Ed.* **2017,** *56*, 14400-14404.

(41) Parker, C. A.; Hatchard, C. G.; Joyce, T. A. *Nature* **1965,** *205*, 1282-1284.

(42) Zhao, J.; Ji, S.; Guo, H. *RSC Adv.* **2011,** *1*, 937-950.

(43) Yakutkin, V.; Aleshchenkov, S.; Chernov, S.; Miteva, T.; Nelles, G.; Cheprakov, A.; Baluschev, S. *Chem. - Eur. J.* **2008,** *14*, 9846-9850.

(44) Singh-Rachford, T. N.; Nayak, A.; Muro-Small, M. L.; Goeb, S.; Therien, M. J.; Castellano, F. N. *J. Am. Chem. Soc.* **2010,** *132*, 14203–14211

(45) Duan, P.; Yanai, N.; Kimizuka, N. *Chem. Commun.* **2014,** *50*, 13111-13113.

(46) Wu, T. C.; Congreve, D. N.; Baldo, M. A. *Appl. Phys. Lett.* **2015,** *107*, 031103.

(47) Yanai, N.; Kozue, M.; Amemori, S.; Kabe, R.; Adachi, C.; Kimizuka, N. *J. Mater. Chem. C* **2016,** *4*, 6447-6451.

(48) Chen, Q.; Liu, Y.; Guo, X.; Peng, J.; Garakyaraghi, S.; Papa, C. M.; Castellano, F. N.et al. *J. Phys. Chem. A* **2018,** *122*, 6673-6682.

(49) Huang, Z.; Li, X.; Mahboub, M.; Hanson, K. M.; Nichols, V. M.; Le, H.; Tang, M. L.et al. *Nano. Lett.* **2015,** *15*, 5552-5557.

(50) Okumura, K.; Mase, K.; Yanai, N.; Kimizuka, N. *Chem. - Eur. J.* **2016,** *22*, 7721-7726.

(51) Wu, M.; Congreve, D. N.; Wilson, M. W. B.; Jean, J.; Geva, N.; Welborn, M.; Van Voorhis, T.et al. *Nat. Photonics* **2016,** *10*, 31-34.

(52) Mongin, C.; Garakyaraghi, S.; Razgoniaeva, N.; Zamkov, M.; Castellano, F. N. *Science* **2016,** *351*, 369-372.

(53) Mase, K.; Okumura, K.; Yanai, N.; Kimizuka, N. *Chem. Commun.* **2017,** *53*, 8261-8264.

(54) Nienhaus, L.; Correa-Baena, J.-P.; Wieghold, S.; Einzinger, M.; Lin, T.-A.; Shulenberger, K. E.; Klein, N. D.et al. *ACS Energy Lett.* **2019,** *4*, 888-895.

(55) Amemori, S.; Sasaki, Y.; Yanai, N.; Kimizuka, N. *J. Am. Chem. Soc.* **2016,** *138*, 8702-8705.

(56) Sasaki, Y.; Amemori, S.; Kouno, H.; Yanai, N.; Kimizuka, N. *J. Mater. Chem. C* **2017,** *5*, 5063-5067.

(57) Yanai, N.; Kimizuka, N. *Acc. Chem. Res.* **2017,** *50*, 2487-2495.

(58) Nattestad, A.; Cheng, Y. Y.; MacQueen, R. W.; Schulze, T. F.; Thompson, F. W.; Mozer, A. J.; Fückel, B.et al. *J. Phys. Chem. Lett.* **2013,** *4*, 2073-2078.

(59) Monguzzi, A.; Oertel, A.; Braga, D.; Riedinger, A.; Kim, D. K.; Knusel, P. N.; Bianchi, A.et al. *ACS Appl. Mater. Interfaces* **2017,** *9*, 40180-40186.

(60) Khnayzer, R. S.; Blumhoff, J.; Harrington, J. A.; Haefele, A.; Deng, F.; Castellano, F. N. *Chem. Commun.* **2012,** *48*, 209-211.

(61) Ravetz, B. D.; Pun, A. B.; Churchill, E. M.; Congreve, D. N.; Rovis, T.; Campos, L. M. *Nature* **2019,** *565*, 343-346.

(62) Monguzzi, A.; Mezyk, J.; Scotognella, F.; Tubino, R.; Meinardi, F. *Phys. Rev. B* **2008,** *78*, 195112.

(63) Haefele, A.; Blumhoff, J.; Khnayzer, R. S.; Castellano, F. N. *J. Phys. Chem. Lett.* **2012,** *3*, 299-303.

(64) Jortner, J.; Choi, S.-i.; Katz, J. L.; Rice, S. A. *Phys. Rev. Lett.* **1963,** *11*, 323-326.

(65) Monguzzi, A.; Frigoli, M.; Larpent, C.; Tubino, R.; Meinardi, F. *Adv. Funct. Mater.* **2012,** *22*, 139-143.

(66) Liu, Q.; Yin, B.; Yang, T.; Yang, Y.; Shen, Z.; Yao, P.; Li, F. *J. Am. Chem. Soc.* **2013,** *135*, 5029-5037.

(67) Mongin, C.; Golden, J. H.; Castellano, F. N. *ACS Appl. Mater. Interfaces* **2016,** *8*, 24038-24048.

(68) Marsico, F.; Turshatov, A.; Pekoz, R.; Avlasevich, Y.; Wagner, M.; Weber, K.; Donadio, D.et al. *J. Am. Chem. Soc.* **2014,** *136*, 11057-11064.

(69) Askes, S. H. C.; Mora, N. L.; Harkes, R.; Koning, R. I.; Koster, B.; Schmidt, T.; Kros, A.et al. *Chem. Commun.* **2015,** *51*, 9137-9140.

(70) Dzebo, D.; Moth-Poulsen, K.; Albinsson, B. *Photochem. Photobiol. Sci.* **2017,** *16*, 1327-1334.

(71) Ma, J.; Chen, S.; Ye, C.; Li, M.; Liu, T.; Wang, X.; Song, Y. *Phys. Chem. Chem. Phys.* **2019,** *21*, 14516-14520.

(72) Plaetzer, K.; Krammer, B.; Berlanda, J.; Berr, F.; Kiesslich, T. *LIMS* **2009,** *24*, 259-268.

(73) Hopkins, S. L.; Siewert, B.; Askes, S. H.; Veldhuizen, P.; Zwier, R.; Heger, M.; Bonnet, S. *Photochem. Photobiol. Sci.* **2016,** *15*, 644-653.

(74) Kim, C. K.; Adhikari, A.; Deisseroth, K. *Nat. Rev. Neurosci.* **2017,** *18*, 222-235.

(75) Kim, J.-H.; Deng, F.; Castellano, F. N.; Kim, J.-H. *Chem. Mater.* **2012,** *24*, 2250-2252.

(76) Kwon, O. S.; Song, H. S.; Conde, J.; Kim, H. I.; Artzi, N.; Kim, J. H. *ACS Nano* **2016,** *10*, 1512-1521.

(77) Simon, Y. C.; Bai, S.; Sing, M. K.; Dietsch, H.; Achermann, M.; Weder, C. *Macromol. Rapid Commun.* **2012,** *33*, 498-502.

(78) Thévenaz, D. C.; Monguzzi, A.; Vanhecke, D.; Vadrucci, R.; Meinardi, F.; Simon, Y. C.; Weder, C. *Mater. Horiz.* **2016,** *3*, 602-607.

(79) Nagai, A.; Miller, J. B.; Kos, P.; Elkassih, S.; Xiong, H.; Siegwart, D. J. *ACS Biomater. Sci. Eng.* **2015,** *1*, 1206-1210.

(80) Askes, S. H.; Pomp, W.; Hopkins, S. L.; Kros, A.; Wu, S.; Schmidt, T.; Bonnet, S. *Small* **2016,** *12*, 5579-5590.

(81) Park, J.; Xu, M.; Li, F.; Zhou, H. C. *J. Am. Chem. Soc.* **2018,** *140*, 5493-5499.

(82) Kim, J.-H.; Deng, F.; Castellano, F. N.; Kim, J.-H. *ACS Photonics* **2014,** *1*, 382-388.

(83) Mattiello, S.; Monguzzi, A.; Pedrini, J.; Sassi, M.; Villa, C.; Torrente, Y.; Marotta, R.et al. *Adv. Funct. Mater.* **2016,** *26*, 8447-8454.

(84) Poznik, M.; Faltermeier, U.; Dick, B.; König, B. *RSC Adv.* **2016,** *6*, 41947-41950.

(85) Carver, T. R.; Slichter, C. P. *Phys. Rev.* **1953,** *92*, 212-213.

(86) Overhauser, A. W. *Phys. Rev.* **1953,** *92*, 411-415.

(87) Takeda, K. *Triplet State Dynamic Nuclear Polarization*; VDM Verlag Dr. Müeller: Saarbrücken, Germany, 2009.

(88) Kovtunov, K. V.; Pokochueva, E. V.; Salnikov, O. G.; Cousin, S. F.; Kurzbach, D.; Vuichoud, B.; Jannin, S.et al. *Chem. - Asian J.* **2018,** *13*, 1857 –1871.

(89) Bowers, C. R.; Weitekamp, D. P. *Phys. Rev. Lett.* **1986,** *57*, 2645-2648.

(90) Eisenber, R. *Acc. Chem. Res.* **1991,** *24*, 110-116.

(91) Adams, R. W.; Aguilar, J. A.; Atkinson, K. D.; Cowley, M. J.; Elliott, P. I. P.; Duckett, S. B.; Green, G. G. R.et al. *Science* **2009,** *323*, 1708-1711.

(92) Duckett, S. B.; Mewis, R. E. *Acc. Chem. Res.* **2012,** *45*, 1247–1257.

(93) Theis, T.; Truong, M. L.; Coffey, A. M.; Shchepin, R. V.; Waddell, K. W.; Shi, F.; Goodson, B. M.et al. *J. Am. Chem. Soc.* **2015,** *137*, 1404-1407.

(94) Nikolaou, P.; Goodson, B. M.; Chekmenev, E. Y. *Chem. - Eur. J.* **2015,** *21*, 3156-3166.

(95) Lilburn, D. M.; Tatler, A. L.; Six, J. S.; Lesbats, C.; Habgood, A.; Porte, J.; Hughes-Riley, T.et al. *Magn. Reson. Med.* **2016,** *76*, 1224-1235.

(96) Bouchiat, M. A.; Carver, T. R.; Varnum, C. M. *Phys. Rev. Lett.* **1960,** *5*, 373-375.

(97) Schröder, L.; Lowery, T. J.; Hilty, C.; Wemmer, D. E.; Pines, A. *Science* **2006,** *314*, 446-449.

(98) Abragam, A.; Goldman, M. *Rep. Prog. Phys.* **1978,** *41*, 395-467.

(99) Ardenkjær-Larsen, J. H.; Fridlund, B.; Gram, A.; Hansson, G.; Hansson, L.; Lerche, M. H.; Servin, R.et al. *Proc. Natl. Acad. Sci. USA* **2003,** *100*, 10158–10163.

(100) Hall, D. A.; Maus, D. C.; Gerfen, G. J.; Inati, S. J.; Becerra, L. R.; Dahlquist, F. W.; Griffin, R. G. *Science* **1997,** *276*, 930-932.

(101) Rossini, A. J.; Zagdoun, A.; Lelli, M.; Lesage, A.; Copéret, C.; Emsley, L. *Acc. Chem. Res.* **2013,** *46*, 1942–1951

(102) Chappuis, Q.; Milani, J.; Vuichoud, B.; Bornet, A.; Gossert, A. D.; Bodenhausen, G.; Jannin, S. *J. Phys. Chem. Lett.* **2015,** *6*, 1674-1678.

(103) Olsen, G.; Markhasin, E.; Szekely, O.; Bretschneider, C.; Frydman, L. *J. Magn. Reson.* **2016,** *264*, 49-58.

(104) Kurzbach, D.; Canet, E.; Flamm, A. G.; Jhajharia, A.; Weber, E. M. M.; Konrat, R.; Bodenhausen, G. *Angew. Chem. Int. Ed.* **2017,** *56*, 389-392.

(105) Sadet, A.; Stavarache, C.; Bacalum, M.; Radu, M.; Bodenhausen, G.; Kurzbach, D.; Vasos, P. R. *J. Am. Chem. Soc.* **2019,** *141*, 12448-12452.

(106) Kim, J.; Mandal, R.; Hilty, C. *J. Phys. Chem. Lett.* **2019,** *10*, 5463-5467.

(107) Lange, S.; Linden, A. H.; Akbey, U.; Franks, W. T.; Loening, N. M.; van Rossum, B. J.; Oschkinat, H. *J. Magn. Reson.* **2012,** *216*, 209-212.

(108) Koivula, E.; Punkkinen, M.; Tanttila, W. H.; Ylinen, E. E. *Phys. Rev. B: Condens. Matter Mater. Phys.* **1985,** *32*, 4556-4564.

(109) Perez, S. C.; Zuriaga, M.; Serra, P.; Wolfenson, A.; Negrier, P.; Tamarit, J. L. *J. Chem. Phys.* **2015,** *143*, 134502.

(110) Sloop, D. J.; Yu, H. L.; Lin, T. S.; Weissman, S. I. *J. Chem. Phys.* **1981,** *75*, 3746-3757.

(111) Henstra, A.; Wenckebach, W. T. *Mol. Phys.* **2014,** *112*, 1761-1772.

(112) Can, T. V.; Weber, R. T.; Walish, J. J.; Swager, T. M.; Griffin, R. G. *Angew. Chem. Int. Ed.* **2017,** *56*, 6744-6748.

(113) Iinuma, M.; Takahashi, Y.; Shaké, I.; Oda, M.; Masaike, A.; Yabuzaki, T. *Phys. Rev. Lett.* **2000,** *84*, 171-174.

(114) Maier, G.; Haeberlen, U.; Wolf, H. C.; Hausser, K. H. *Phys. Lett.* **1967,** *25A*, 384-385.

(115) Deimling, M.; Brunner, H.; Dinse, K. P.; Hawser, K. H. *J. Magn. Reson.* **1980,** *39*, 185-202.

(116) Fujiwara, S.; Hosoyamada, M.; Tateishi, K.; Uesaka, T.; Ideta, K.; Kimizuka, N.; Yanai, N. *J. Am. Chem. Soc.* **2018,** *140*, 15606-15610.

(117) Yamada, M.; Ikemoto, I.; Kuroda, H. *Bull. Chem. Soc. Jpn.* **1988,** *61*, 1057-1062.

(118) Maliakal, A.; Raghavachari, K.; Katz, H.; Chandross, E.; Siegrist, T. *Chem. Mater.* **2004,** *16*, 4980-4986.

(119) Jackson, M.; Mantsch, H. H. *Biochim. Biophys. Acta* **1991,** *1078*, 231-235.

Chapter 2 Triplet energy migration-based photon upconversion by amphiphilic molecular assemblies in aerated water

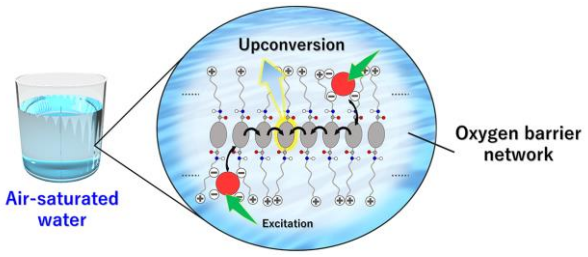

ABSTRACT: A molecular self-assembly approach is developed to resolve an outstanding issue in triplet energy migration-based photon upconversion (TEM-UC), that is, air-stable TEM-UC in water. Amphiphilic cationic acceptor (emitter) molecules self-assemble in water via hydrophobic and hydrogen bonding interactions, with which anionic donor (sensitizer) molecules are integrated through electrostatic interactions. Triplet energy is quantitatively transferred from the excited donor to the acceptor, which is followed by effective triplet energy migration among the pre-organized acceptors. It leads to TTA and concomitant UC emission in water. The dense acceptor chromophore arrays with extended hydrogen bonding networks show efficient barrier properties against molecular oxygen, as demonstrated by the stable UC emission even in air-saturated water.

2.1 Introduction

Photon upconversion (UC), converting lower-energy photons to higher-energy photons, has attracted considerable attention because of its wide variety of applications ranging from renewable energy production to bioimaging and photodynamic therapy.[1-5] Conventional UC mechanisms such as two-photon absorption and multistep excitation of lanthanides, however, require strong excitation light intensity (>Wcm^{-2}), thus limiting their applications.[6,7] On the other hand, triplet–triplet annihilation (TTA)-based UC with multi-component triplet donor (D, sensitizer) and acceptor (A, emitter) system can operate under a non-coherent, low intensity light source.[1,8-15] As summarized in Figure 2-1, this mechanism starts with the generation of donor triplets ($T_{1,D}$) by intersystem crossing (ISC) from the photo-generated singlet state ($S_{1,D}$), and the succeeding D-to-A triplet–triplet energy transfer (TTET) forms optically dark, metastable acceptor triplets ($T_{1,A}$). The subsequent diffusion and collision of two excited acceptor triplets generate a higher energy excited singlet state ($S_{1,A}$) through TTA, from which the upconverted delayed fluorescence is emitted. The TTET and TTA processes occur via an electron exchange mechanism (Dexter energy transfer), which requires the involved molecules to come close within the distance of 1 nm.

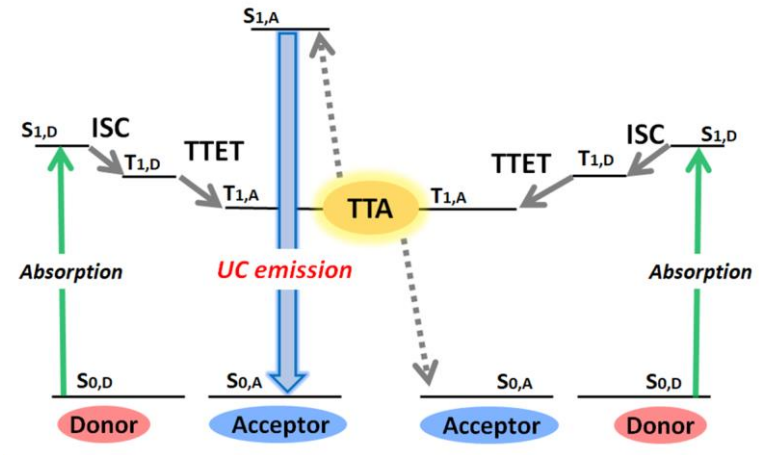

Figure 2-1. An outline of the TTA-UC process, showing the energy levels involved in the TTA-UC (S = singlet, T = triplet). The TTA-UC utilizes a pair of donor (sensitizer) with high intersystem crossing (ISC) efficiency and acceptor (emitter) with high fluorescence quantum yield. Green and blue arrows indicate the absorption and emission processes, respectively. TTET: triplet-triplet energy transfer, TTA: triplet-triplet annihilation.

In spite of the growing demand for photocatalytic and biological applications, most studies on TTA-based UC involve investigations in deaerated organic solvents, and examples in air-saturated aqueous phase have been limited because of the massive quenching of excited triplet states by dissolved molecular oxygen. Previous reports have shown that this oxygen quenching can be suppressed by employing specific solid polymers or viscous liquids as matrices to reduce the oxygen concentration.[16-21] For example, Kim and coworkers have reported photocatalytic reactions in aerated water by encapsulating UC chromophores in viscous hexadecane/polyisobutylene mixture.[17,19,21] Another strategy is to utilize viscous matrices with singlet oxygen scavenging ability.[22-26] Li et al. observed UC emission in aerated water by loading UC dyes in nanocapsules containing reductive linoleic acid and oleic acid, and applied their nanomaterials to in vivo bioimaging.[22] While these approaches allow for air-stable UC emission with reasonably high efficiency, the limited diffusion of large dye molecules in these viscous matrices is forecast to cause potential issues for further advancements.

An alternate strategy for aqueous UC is to take advantage of fast triplet energy migration (TEM) in condensed chromophore assemblies.[12,15,27-31] In essence, TEM-UC is the chemistry challenge of how to pre-organize donor and acceptor molecules for effective donor-to-acceptor TTET and inter-acceptor TEM.[31] TEM-UC works even in the absence of molecular diffusion, and therefore it has the potential to solve the inevitable issues associated with molecular-diffusion-based UC. While air-stable TEM-UC has recently been achieved in solvent-free liquids and self-assembled acceptors in organic media,[12,15,28,29] oxygen tolerant TEM-UC has not been realized in aqueous media. In this work, we show the first example of an air-stable aqueous TEM-UC system (Figure 2-2). Ordered aqueous molecular self-assemblies such as bilayer membranes have been shown to give regular chromophore alignment and exert efficient singlet energy transfer characteristics.[32,33] We made the assumption that such densely organized molecular assemblies with extended molecular networks such as hydrogen bonding may prevent the intrusion of molecular oxygen from the bulk water into the hydrophobic interior of the molecular selfassemblies.[34]

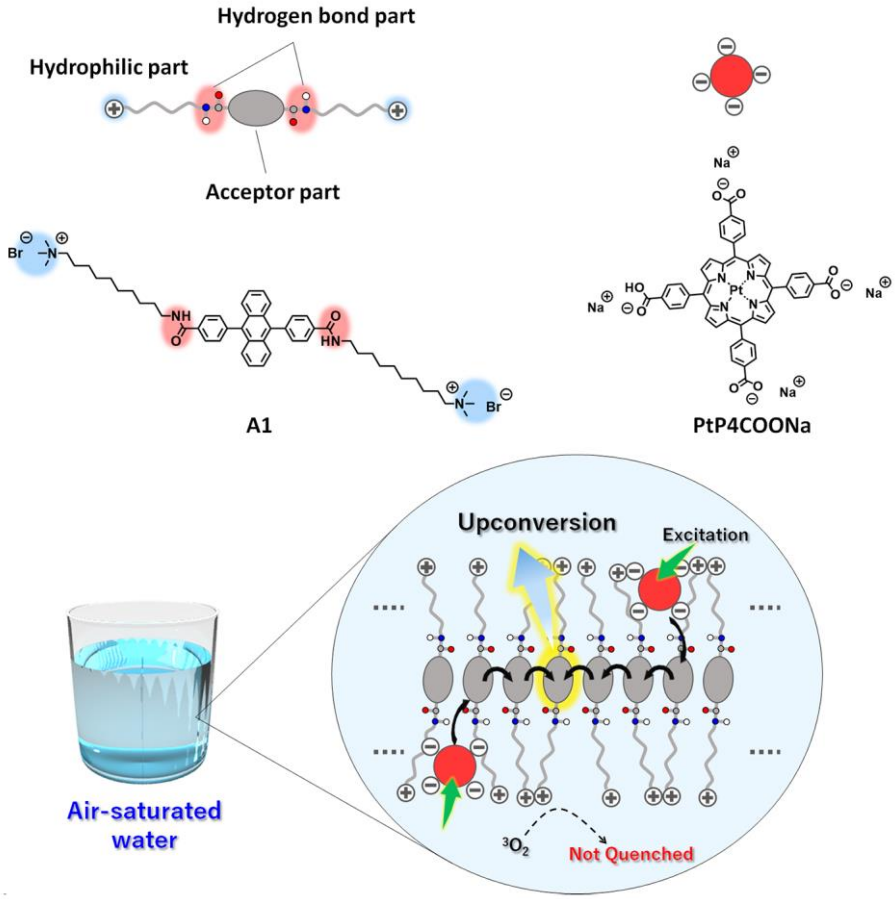

Figure 2-2. Schematic illustration of the aqueous TEM-UC system. Amphiphilic acceptor **A1** self-assembles in water to form monolayer membranes which are stabilized by hydrophobic and hydrogen bonding interactions. Anionic donor PtP4COONa co-assembles with the cationic acceptor membrane **A1** in water. Photo-excitation of the donor is followed by ISC, donor-to-acceptor TTET, TEM among the acceptor arrays, interacceptor TTA, and upconverted photoluminescence. Oxygen quenching is effectively avoided by the developed intermolecular hydrogen bonding networks in the acceptor monolayer membranes.

As a proof of concept, we designed a novel amphiphilic acceptor **A1** based on the prototypical acceptor 9,10-diphenylanthracene (DPA). Quaternary ammonium groups were introduced at both ends of the DPA chromophore, by reference to the molecular design of aqueous monolayer membranes.[35-37] The DPA unit is modified with amide groups since the formation of dense hydrogen bonding networks would be beneficial for blocking oxygen.[28,34] The long alkyl chain spacer groups locate the amide groups in the hydrophobic interior of the molecular membrane structure, which would facilitate the formation of hydrogen bond networks in water.[38] While the typical donor Pt(II) octaethylporphyrin (PtOEP) was too hydrophobic to be stably dispersed in the aqueous self-assemblies of **A1**, anionic donor PtP4COONa co-assembles with cationic **A1**, to which triplet energy was efficiently transferred (Figure 2-2). These donor–acceptor co-assemblies showed an efficient TEM-UC emission in deaerated aqueous dispersions, which was largely preserved even in the air-saturated aqueous systems. Control experiments in a water/DMF mixed solvent and with another acceptor **A2** that does not have amide groups showed no UC emission, indicating the important roles that dense molecular packing and intermolecular networks play in blocking oxygen molecules.

2.2 Experimental section

2.2.1 General methods

Characterizations

^{1}H NMR (300 MHz) spectra were measured on a Bruker DRX-spectrometer using TMS as the internal standard. Elemental analysis was conducted at the Elemental Analysis Center, Kyushu University. Absorption spectra were recorded on a JASCO V-670 spectrophotometer. Fluorescence spectra were measured by using a PerkinElmer LS 55 fluorescence spectrometer. Time-resolved photoluminescence lifetime measurements were carried out by using a time-correlated single photon counting lifetime spectroscopy system, HAMAMATSU Quantaurus-Tau C11567-01. Upconverted emission spectra were recorded on a Hamamatsu Photonics PMA-12 with the excitation source using an external, adjustable semiconductor laser (532 nm) and Argon laser GLG3100 (515 nm). The absolute quantum yield was measured in an integrating sphere using a Hamamatsu Photonics absolute quantum yield measurement system. The UC sample preparation was carried out by using Biotage Initiator. Transmission electron microscopy images were measured by using JOEL JEM-2010. Dynamic light scattering measurements were carried out by using Malvern Nano-ZS ZEN3600.

Determination of TTA-UC quantum yield

The upconverted luminescence quantum efficiency was determined relative to a standard according to the following equation,[2]

$$\Phi_{UC}{}' = 2\Phi_{std}\left(\frac{A_{std}}{A_{UC}}\right)\left(\frac{I_{UC}}{I_{std}}\right)\left(\frac{\eta_{UC}}{\eta_{std}}\right)^2$$

where, Φ, A, I and η represented the quantum yield, absorbance at 385 nm, integrated photoluminescence spectral profile, and a refractive index of the solvent. The subscripts UC and std denote the parameters of the upconversion and standard systems. The quantum efficiency of **A1** was determined relative to a standard, Rhodamine B in water (Φ = 0.25). Note that the theoretical maximum of $\Phi_{UC}{}'$ is standardized to be 1 (100%).

2.2.2 Materials

All reagents and solvents for synthesis were used as received without further purification. Pt (II) octaethylporphyrin (PtOEP) was purchased from Aldrich and used as received. PtP4COONa was synthesized according to the reported procedure.[39] ^{1}H NMR (300 MHz, $CDCl_3$): δ (ppm) = 1.20 (d, 24H), 2.78 (quintet, 4H), 7.36 (d, 4H), 7.50 (t, 2H), 8.66 (d, 4H), 8.75 (s, 4H), 8.77 (d, 4H).

Scheme 2-1

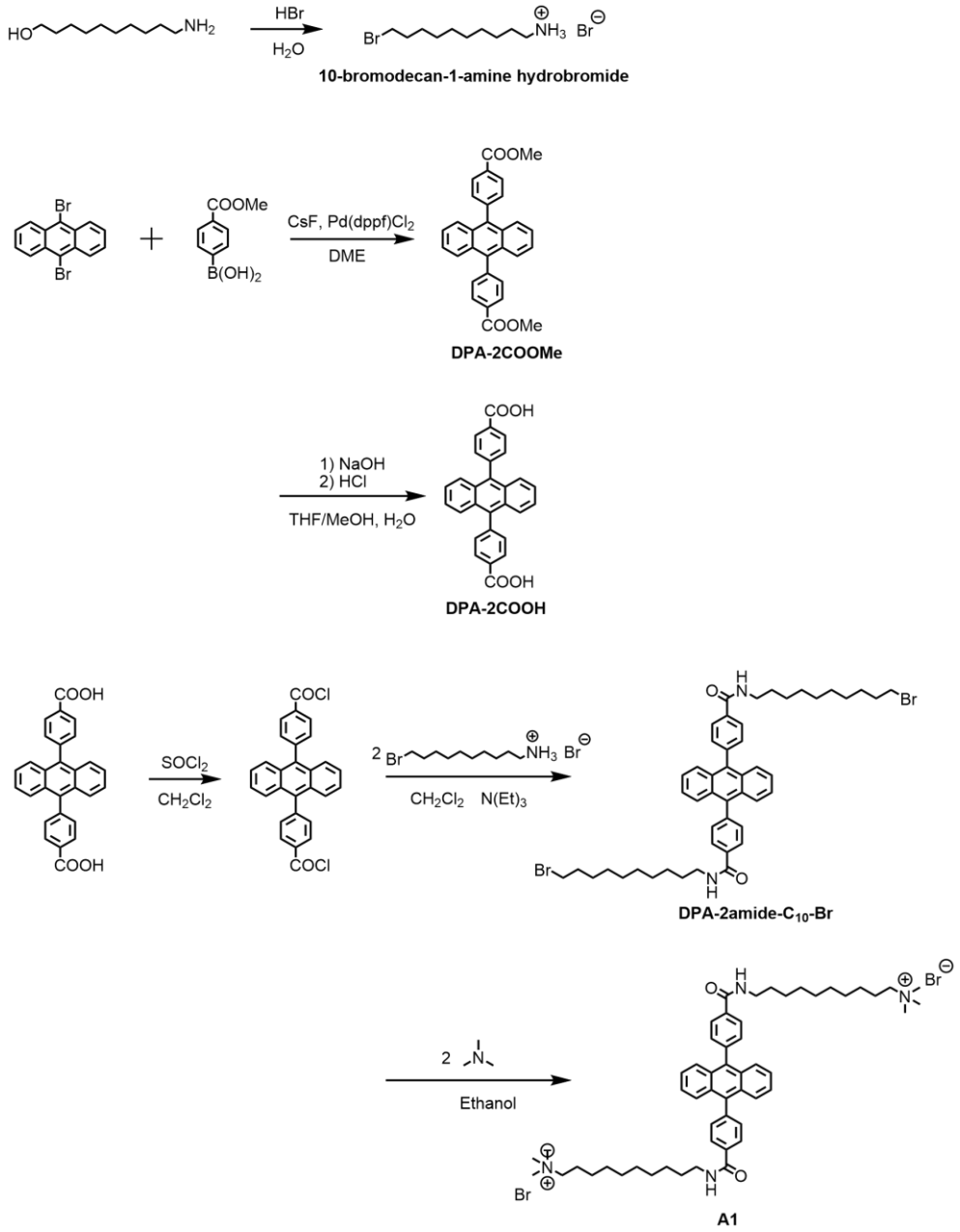

2.2.2-1 Synthesis of 10-bromodecane-1-ammonium bromide

5.1 ml of hydrobromic acid (48 %) was placed in 100 ml flask and cooled by using ice bath, to which 500 mg (2.9 mmol) of 10-aminodecane-1-ol was slowly added. The suspension was refluxed for 6 h under Ar. The solvent was removed under reduced pressure and the product was purified by recrystallization in toluene/ethanol (50/1) to give a colorless solid 10-bromodecane-1-ammonium bromide (yield : 74.2%).
^{1}H NMR (300 MHz, $CDCl_3$): δ (ppm) = 1.25-1.47 (m, 12H), 1.77-1.85 (m, 4H), 2.97-3.10 (m, 2H), 3.41 (t, 2H), 8.05 (s, 3H).

2.2.2-2 Synthesis of DPA-2COOMe

A mixture of 2.50 g (14 mmol) (4-(methoxycarbonyl)phenyl)boronic acid, 1.50 g (4.5 mmol) 9,10-dibromo anthracene, 2.47 g (16.3 mmol) CsF and 110 mg (0.135 mmol) [1,1'-Bis(diphenylphosphino)ferrocene]palladium(II) dichloride dichloromethane Adduct were placed in a 300 ml flask under Ar, and 75 ml of degassed 1,2-dimethoxyethane were added. After refluxing under Ar for 50 h, the solvent was removed to give a yellow residue. This obtained solid was suspended in 35 ml water and extracted with 100 ml of $CHCl_3$. After drying the organic phase over Na_2SO_4 and removing the solvent, the product was purified by column chromatography ($CHCl_3$) over silica gel to yield of a yellow powder (yield: 47.1%).
^{1}H NMR (300 MHz, $CDCl_3$): δ (ppm) = 4.03 (s, 6H), 7.56 (dd, 4H), 7.63 (dd, 8H), 8.31 (dd, 4H).

2.2.2-3 Synthesis of DPA-2COOH

To a suspension of 410 mg (9.18 mmol) of dimethyl 4,4-(anthracene-9,10-diyl)dibenzoate in 150 ml 1:1 mixture of THF/MeOH, 30 ml of a 2 M KOH aqueous solution was added. The mixture was heated to 40 °C for 1 day. The mixture formed by acidification with aqueous HCl (2 M) was collected by filtration, washed several times with water, yielding 204 mg (yield: 53.1 %) of a pale yellow solid.
^{1}H NMR (300 MHz, DMSO-d6): δ (ppm) = 7.44-7.49 (m, 4H), 7.51-7.58 (m, 4H), 7.64 (dd, 4H), 8.22 (dd, 4H).

2.2.2-4 Synthesis of DPA-2amide-C_{10}-Br

150 mg (0.36 mmol) of 4,4-(anthracene-9,10-diyl)dibenzoic acid was placed in 50 ml flask, and 10 ml of dehydrated benzene was added under Ar. Then, 1 ml of thionyl chloride were added to the suspension and refluxed for 5 h with catalyst quantity of dehydrated DMF. After removing the solvent and excess thionyl chloride under reduced pressure, residual yellow solid was dispersed into 15 ml of distilled dichloromethane, and this solution was added dropwise to 249 mg (0.79 mmol) of 10-bromodecane-1-ammonium bromide dissolved in 300 ml of dehydrated dichloromethane and 350 μl of trimethylamine under Ar. This mixture was stirred at room temperature for 1 day. After the reaction, the solution was washed several times with diluted hydrochloric acid aqueous solution, Na_2SO_4 aqueous solution, water with dichloromethane. Evaporation of the organic layer under reduced pressure and column chromatography with chloroform/methanol (30/1) over silica gel yielded 20 mg (yield: 5.4%) of a colorless solid.
^{1}H NMR (300 MHz, DMF-d7): δ (ppm) = 1.30-1.45 (m, 24H), 1.50-1.58 (m, 4H), 1.70 (quin, 4H), 1.90 (quin, 4H), 3.42 (t, 4H), 3.55 (quin, 4H), 6.27 (t, 2H), 7.34 (q, 4H), 7.58 (dd, 4H), 7.61 (quin, 4H), 8.06 (dd, 4H).

2.2.2-5 Synthesis of acceptor 1 (**A1**)

20 mg (0.023 mmol) of DPA-2amide-C_{10}-Br was dissolved in 10 ml of trimethylamine ethanol solution. The solution was heated by microwave at 80 °C for 14 h. After the reaction, the solution was cooled to room temperature. The precipitated colorless solid product was purified by filtration to provide **A1** (yield: 52.8%).
^{1}H NMR (300 MHz, DMF-d7): δ (ppm) = 1.30-1.50 (m, 24H), 1.65-1.75 (m, 4H), 1.85-1.95 (m, 4H),3.34-3.36 (s, 18H), 3.49-3.51. (m, 8H), 7.51-7.55 (m, 4H), 7.62-7.66 (m, 8H), 8.32 (dd, 4H), 8.76 (t, 2H).
Elemental analysis for C54H76N4O2Br2: calculated (%) H 7.87 C 66.66 N 5.76; found (%) H 7.62 C 66.41 N 5.62.

Scheme 2-2

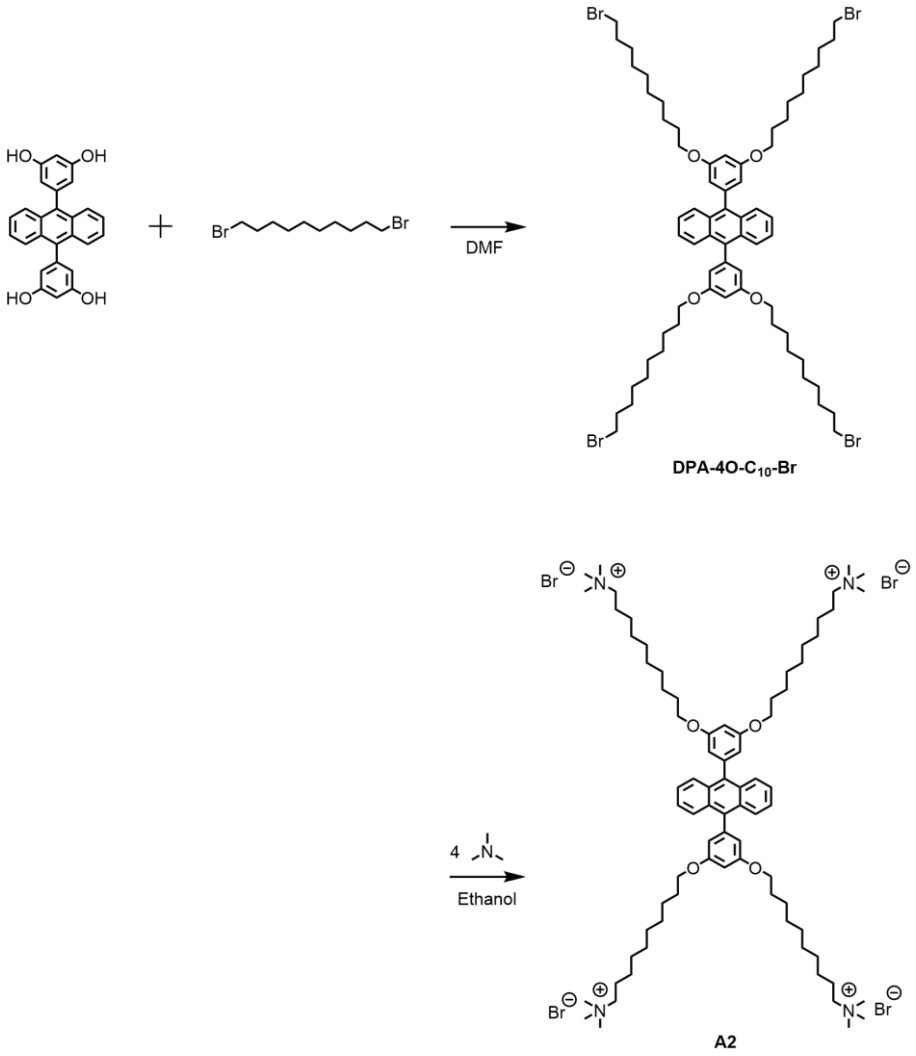

2.2.2-6 Synthesis of DPA-4C_{10}-Br

9,10-Bis(3,5-dihydroxyphenyl)anthracene, 0.78 g (2.0 mmol), 1,10-dibromodecane, 6.0 g (20 mmol), and Potassium carbonate 1.38 g (10 mmol) were placed in 100 ml flask under N_2, and 60 ml of dehydrated DMF was added. The solution was stirred at room temperature for 24 h. After the reaction, the solution was washed several times with hexane/dichloromethane mixture (1/5) and water, dried over anhydrous Na_2CO_3. The solvent was removed under reduced pressure, and the product was purified by recrystallization in ethyl acetate and hexane (1/49) to give needle crystals DPA-4O-C_{10}-Br (yield: 22.6%).

^{1}H NMR (300 MHz, $CDCl_3$, TMS standard): δ (ppm) = 1.20-1.50 (m, 48H), 1.81 (sep, 16H), 3.39 (t, 8H), 3.97 (t, 8H), 6.61 (d, 4H), 6.63 (t, 2H), 7.33 (dd, 4H), 7.78 (dd, 4H).

2.2.2-7 Synthesis of acceptor 2 (**A2**)

413 mg (0.33 mmol) of DPA-4O-C_{10}-Br was dissolved in 10 ml of trimethylamine ethanol solution. The solution was heated by microwave at 80 °C for 14 h. After the reaction, the solution was cooled to room temperature, and the precipitated colorless solid product was purified by filtration to provide **A2** (yield: 24.6%).

^{1}H NMR (300 MHz, DMF-d7): δ (ppm) = 1.30-1.50 (m, 48H), 1.80-1.90 (m, 16H), 3.35 (s, 36H), 3.61 (m, 8H), 4.13 (t, 8H), 6.66 (d, 4H), 6.82 (t, 2H), 7.51 (dd, 4H), 7.78 (dd, 4H).

Elemental analysis for C78H130N4O4Br4: calculated (%) H 8.69 C 62.14 N 3.72; found (%) H 8.62 C 61.97 N 3.67.

2.3 Results and discussion

2.3.1 Self-assembly behaviors of A1 in water

The novel acceptor **A1** was synthesized and fully characterized. Its purity was confirmed by ^{1}H-NMR measurements and elemental analysis (see Scheme 2-1). The self-assembly behavior of **A1** in water was studied using transmission electron microscopy, dynamic light scattering (DLS), IR spectroscopy and temperature-dependent absorption spectroscopy. Transmission electronmicroscopy conducted for the aqueous dispersion of **A1** exhibited round nanostructures with an average diameter of ca. 100 nm (Figure 2-3a). This was consistent with the DLS profile of **A1** in water ([**A1**] = 1 mM), which indicated the formation of nanoassemblies with an average size of 110 nm (Figure 2-3b). The IR spectrum of **A1** cast film showed a C=O stretching vibration at 1631 cm^{-1} and N–H stretching band at 3319 cm^{-1}, which indicate the formation of intermolecular hydrogen bonding (Figure 2-3c).[30,40,41] Importantly, these IR bands were maintained for the aqueous dispersion of **A1** (Figure 2-3c). These results clearly confirm that the acceptor amphiphile **A1** forms supramolecular nanoassemblies in water which are stabilized by hydrogen bonding and hydrophobic interactions.

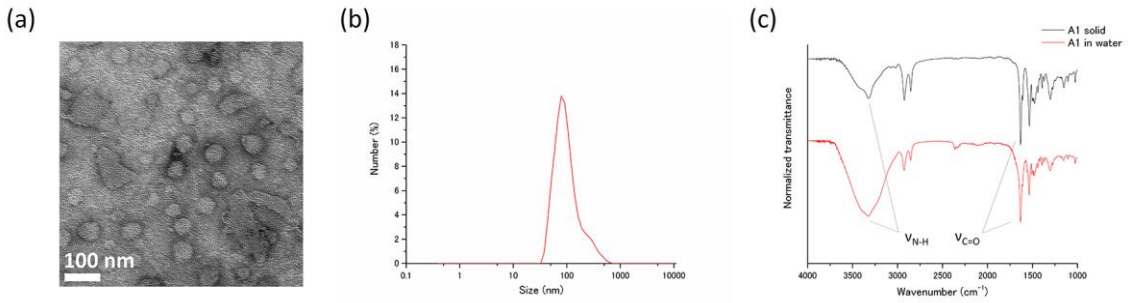

Figure 2-3. Self-assembly behaviors of **A1** in water. (a) Transmission electron microscopy image of **A1**. The sample was post stained with uranyl acetate. (b) DLS profile of **A1** in water ([**A1**] = 1 mM). (c) IR spectrum of **A1** in the solid state (black) and in the aqueous dispersion state ([**A1**] = 100 mM). High concentration of **A1** was necessary to observe the IR peaks due to the low sensitivity of IR measurements. The **A1** molecules were nicely dispersed in water without precipitation even in this high concentration condition.

The absorption spectrum of **A1** in water ([**A1**] = 1 mM) exhibited peaks of ^{1}La transitions at 360, 377.5 and 399 nm at 293 K, corresponding to transition dipoles polarized along the short axis of the anthracene moiety.[42] Upon heating the aqueous dispersion to 363 K, these bands showed small blue shifts to 358.5, 376, and 395.5 nm (Figure 2-4). The observed small spectral shifts indicate the presence of weak interactions between the transition moments, probably because of the steric effects caused by the conformationally twisted benzene groups attached to the 9,10-positions of the anthracene chromophore.

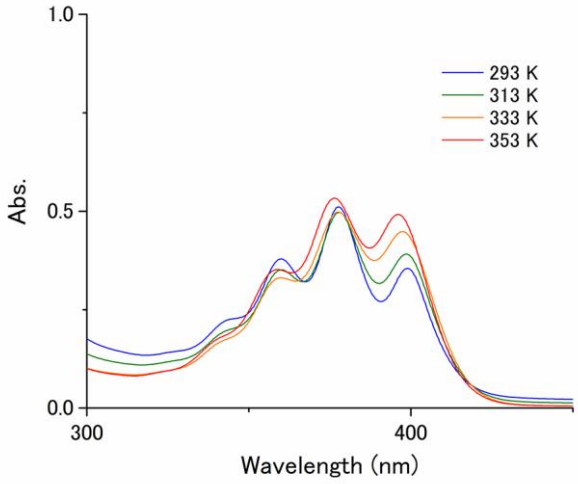

Figure 2-4. Temperature-dependent absorption spectra of **A1** in water ([**A1**] = 1 mM).

The fluorescence spectrum of **A1** in water shows a band at around 440 nm, which doesn't show large overlaps with the donor absorption spectra (Figure 2-5). A high absolute fluorescence quantum yield of 53% was observed for **A1** in water ([**A1**] = 1 mM).

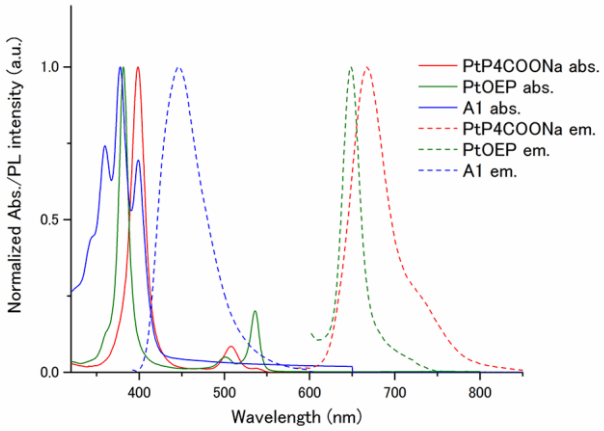

Figure 2-5. Normalized absorption (solid lines) and emission (dashed lines) spectra of **A1** (blue, λ_{ex} = 375 nm, 1 mM) and PtP4COONa (red, λ_{ex} = 510 nm, 1 μM) in water, and PtOEP in chloroform (green, λ_{ex} = 532 nm, 1 μM) at room temperature.

While the acceptor DPA units are densely arrayed in the **A1** assembly, the conformationally twisted phenyl rings attached to the anthracene moiety seem to suppress the strong interchromophore interactions and concomitant quenching of the fluorescence, as observed in absorption and emission behaviours.

2.3.2 TTA-UC properties of A1 in deaerated water

The dense molecular alignment with hydrogen bond networks formed in **A1** assemblies effectively prevent the quenching of the UC emission by oxygen in water. The photoluminescence spectra of **A1** and PtOEP in water ([**A1**] = 1 mM, [PtOEP] = 1 μM) were measured after deaeration by repeated freeze–pump–thaw cycles. Under excitation at 532 nm, an UC emission was clearly observed at around 440 nm (Figure 2-6a), and the spectral shape matches well with the fluorescence spectrum of **A1** (Figure 2-5). Very interestingly, this UC emission was found to be largely preserved also in the air-saturated aqueous dispersion (Figure 2-6a).

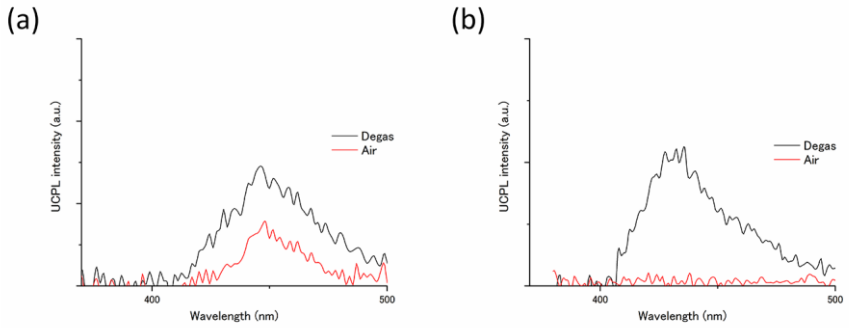

Figure 2-6. Upconvertd photoluminescence (UCPL) spectra of (a) **A1**-PtOEP (b) **A2**-PtOEP in water ([**A1**] = [**A2**] =1 mM, [PtOEP] = 1 μM) in the absence (black) and presence (red) of dissolved air (oxygen) under excitation at 532 nm. Scattered incident laser light was removed by a notch filter (532 nm).

To understand the role of the intermolecular network structure, we carried out control experiments by synthesizing another new DPA-based amphiphilic acceptor **A2** that does not possess amide groups (Figure 2-7a). The **A2** molecules also form self-assembled nanostructures in water, as evidenced by transmission electron microscopy, DLS and temperature-dependent absorption measurements (Figure 2-7). The **A2**–PtOEP also showed an UC emission in the deaerated aqueous dispersion ([**A2**] = 1 mM, [PtOEP] = 1 μM), however, this UC emission entirely disappeared in the aerated specimens (Figure 2-6b). These results indicate that the dense molecular alignment promoted by the developed intermolecular hydrogen bonding networks is crucial to avoid oxygen quenching.

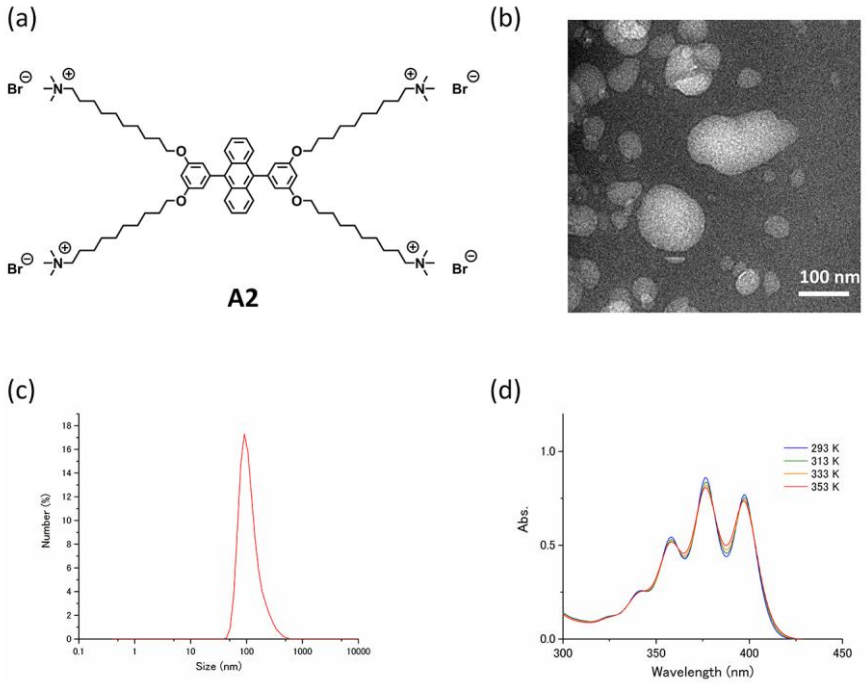

Figure 2-7. (a) Chemical structure of **A2**. (b) Temperature-dependent absorption spectra of **A2** in water ([**A2**] = 1 mM). (c) DLS profile of **A2** in water ([**A2**] = 1 mM). (d) Transmission electron microscopy image of **A2**. The sample was post stained by uranyl acetate.

Absorption spectrum of **A2** in water exhibited peaks at 358, 376, 396.5 nm at 293 K, which showed small blue shifts to 357, 375, 395.5 nm by heating to 353 K. The DLS profile of **A2** in water indicates the formation of nanoassemblies with an average size of 103.6 nm. The transmission electron microscopy image of **A2** exhibited round nanostructures. These results confirm that the hydrophobic interactions allow **A2** to form supramolecular nanoassemblies in water.

We should note that the UC emission of the **A1**–PtOEP system was weak even in the deaerated dispersion, which is accompanied by the phosphorescence of PtOEP at 650 nm. Upon incubating the aqueous **A1**–PtOEP dispersion for 24 h, precipitation of the red PtOEP aggregates was observed. Apparently, the hydrophobic donor PtOEP is not co-dispersed stably and tends to segregate, resulting in poor donor-to-acceptor TTET efficiency.

Meanwhile, by employing the anionic donor PtP4COONa (Figure 2-2), the compatibility with the cationic acceptor **A1** was improved. When PtP4COONa was mixed with **A1** in deaerated dispersion at room temperature ([**A1**] = 1 mM, [PtP4COONa] = 1 mM), only donor phosphorescence was observed with almost no UC emission, reflecting that the rigid molecular assembly of **A1** did not accommodate donor molecules. To co-assemble the donor and acceptor, a mixed aqueous dispersion of **A1**–PtP4COONa was heated in a microwave at 393 K for 30 min and incubated at room temperature under stirring for 48 h. The obtained aqueous dispersion was deaerated by repeated freeze–pump–thaw cycles. Interestingly, the obtained dispersion showed a clear UC emission at 440 nm (Figure 2-8a). Almost no donor phosphorescence at 670 nm indicates the integration of donor molecules in acceptor assemblies, facilitating efficient donor-to-acceptor TTET. The heating procedure may have disassembled the acceptor nanostructure but it ensured the electrostatic co-assembly between the acceptor and donor.

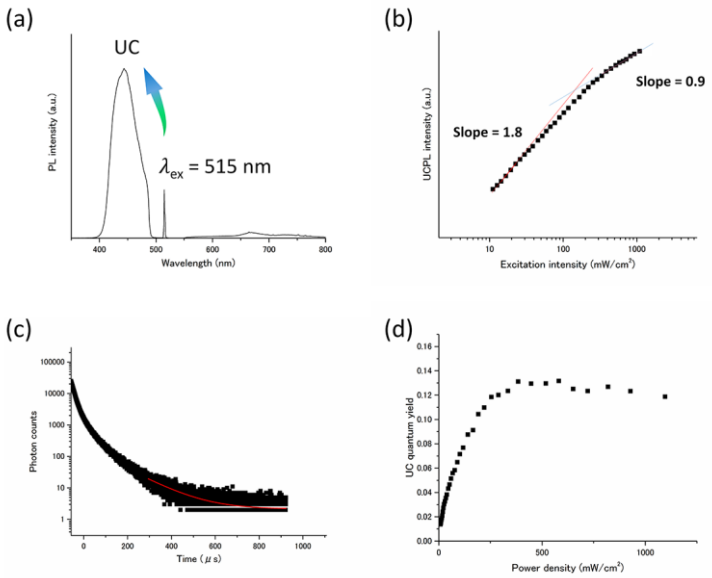

Figure 2-8. (a) Photoluminescence spectrum of **A1**–PtP4COONa in deaerated water ([**A1**] = 1 mM, [PtP4COONa] = 1 mM, λ_{ex} = 515 nm, excitation intensity = 275 mWcm^{-2}). Scattered incident laser light was removed by 490 nm short-pass filter (for UC emission) and by 550 nm long-pass filter (for phosphorescence). (b) UC emission intensity at 440 nm of **A1**–PtP4COONa in deaerated water as a function of the excitation intensity ([**A1**] = 1 mM, [PtP4COONa] = 1 mM, λ_{ex} = 515 nm). The solid red and blue lines are fitting results with slopes of 1.8 and 0.9 in the low and high power regimes, respectively. (c) UC emission decay at 440 nm of **A1**–PtP4COONa in deaerated water under 531 nm pulsed excitation. The red fitting curve in the tail part of the decay was obtained by considering the

relationship of $I_{UC}(t) \propto exp\left(-\frac{t}{\tau_{UC}}\right) = exp\left(-\frac{2t}{\tau_{A,T}}\right)$, where τ_{UC} is UC emission lifetime and $\tau_{A,T}$ is acceptor triplet lifetime. (d) Dependence of UC quantum yield Φ_{UC}' on the excitation intensity of **A1**-PtP4COONa in deaerated water at room temperature ([**A1**] = 1 mM, [PtP4COONa] = 1 μM, λ_{ex} = 515 nm).

The TTA-based UC mechanism was confirmed by the excitation intensity dependence and lifetime of the UC emission. The TTA-based UC emission intensity generally shows a quadratic and first-order dependence on the incident intensity in the low- and high-excitation intensity ranges, respectively. A double logarithmic plot for the UC emission intensity of the **A1**–PtP4COONa aqueous dispersion as a function of incident light intensity showed a transition from a slope of ca. 2 to 1, providing unequivocal evidence for TTA-based UC (Figure 2-8b). The I_{th} value of 130 mW cm^{-2} is experimentally determined as the intersection point. The TTA-based mechanism was further supported by the UC emission decay in microsecond time scale characteristics to UC via a long-lived triplet state (Figure 2-8c). It has been well documented that the TTA-based delayed fluorescence is not a single exponential decay, but its tail part obeys single exponential behavior.[3,43] The acceptor triplet lifetime $\tau_{A,T}$ was obtained as 238 μs by considering the known relationship of

$$I_{UC}(t) \propto \exp\left(-\frac{2t}{\tau_{A,T}}\right)$$

The triplet diffusion constant for the acceptor arrays D_T was estimated by using the following relationship,[44]

$$I_{th} = \frac{1}{8\pi a_0 \alpha \Phi_{TTET} D_T \tau_{A,T}^2}$$

where α is the absorption coefficient at the excitation wavelength in cm^{-1}, Φ_{TTET} is the donor-to-acceptor TTET efficiency (ca. 1), and a_0 is the annihilation distance between acceptor triplets (9.1 Å for DPA triplets).[44] From these parameters, we obtained a fairly high DT value of 1.4 × 10^{-4} cm^2 s^{-1}, being higher than the diffusion constant of DPA in a low-viscosity solvent (1.2 × 10^{-4} cm^2 s^{-1}).[44]

2.3.3 Air-stability of TTA-UC emission in aerated water

The remarkable air-stability of the aqueous TEM-UC emission was demonstrated by the UC quantum yield and time dependent UC emission measurements. The UC quantum yield was determined by using an aqueous solution of rhodamine B as a standard. Because the TTA-UC process converts two photons to one photon, the theoretical maximum of the UC quantum yield Φ_{UC} is 50%.[10,13,45] Meanwhile, in many reports this value is multiplied with 2 to set the maximum conversion efficiency as 100%. To avoid the confusion between these different definitions, the UC quantum yield is written as Φ_{UC}' ($= 2\Phi_{UC}$) when the maximum efficiency is standardized to be 100%. A high Φ_{UC}' value of 13% was obtained for **A1**–PtP4COONa in deaerated water (Figure 2-8d). Note that the fluorescence lifetime of **A1** was not almost affected by the donor PtP4COONa, indicating the absence of acceptor-to-donor singlet–singlet back energy transfer (Figure 2-9).

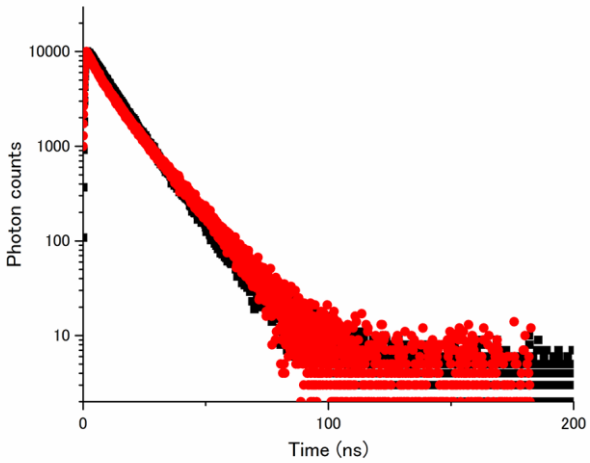

Figure 2-9. Fluorescence decays at 450 nm for **A1** (black) and **A1**-PtP4COONa (red) in air-saturated water under pulsed excitation at 365 nm ([**A1**] = 1 mM, [PtP4COONa] = 1 μM).

Significantly, even in the presence of dissolved oxygen, more than half of the Φ_{UC}' value was maintained (7.0%). This quantum yield is comparable to those of previous highly efficient molecular diffusion-based UC systems in aerated conditions.[21,22] The timedependent UC emission of **A1**–PtP4COONa in the air-saturated aqueous dispersion maintained peak intensity right after starting the laser irradiation for more than 10,000 seconds (Figure 2-10). It has been reported that the UC emission becomes stronger with time when oxygen molecules are consumed by photochemical reactions.[5,28] The absence of such a gradual increase in emission intensity indicates the intrinsic oxygen barrier ability of the aqueous molecular assembly system.

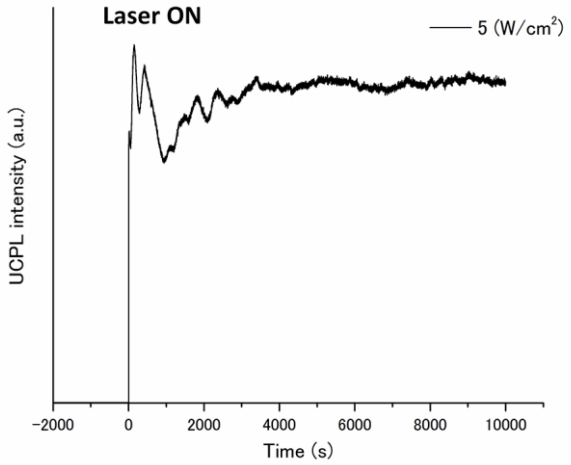

Figure 2-10. Time dependence of the UC emission intensity of **A1**–PtP4COONa in air-saturated water at 450 nm upon continuous excitation at 515 nm with a laser light intensity of 5 W cm^{-2}.

2.3.4 Oxygen-barrier ability and the effect of self-assembly

To understand this air-stable behaviour, we carried out control experiments by employing a water/DMF (1:1 in volume) mixed solvent instead of pure water for the **A1**–PtP4COONa pair to weaken the hydrophobic interactions and eventually break the hydrogen bonding networks. In contrast to the temperature-dependent shifts observed in the absorption spectra of **A1** by supramolecular assembly/disassembly (Figure 2-11), the absorption peaks of **A1** at 357.5, 376, 396 nm did not show any shift between 298 K and 363 K in water/DMF, indicating the absence of interchromophore close-contact assembly in water/DMF (Figure 2-11).

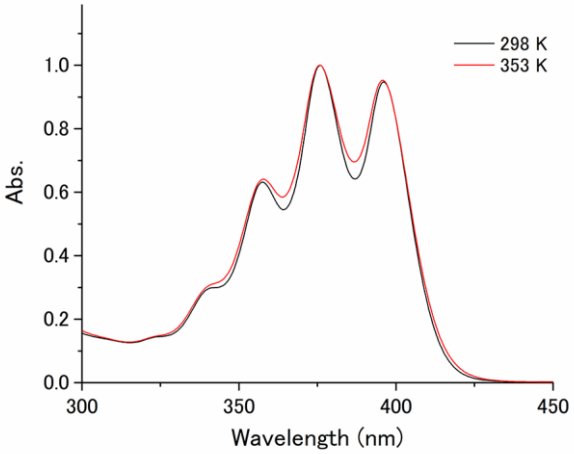

Figure 2-11. Absorption spectra of A1-PtP4COONa ([**A1**] = 1 mM, [PtP4COONa] = 1 μM) at 298 K (black) and 353 K (red) in DMF/water (1:1 in volume).

We compared the photoluminescence spectra of the **A1**–PtP4COONa pair in air-saturated water and water/DMF (Figure 2-12). Very interestingly, the UC emission, observed in aerated water, was completely quenched in aerated water/DMF. This clear difference supports the principal role of dense molecular alignment of **A1** promoted by hydrogen bonding networks in monolayer membranes in avoiding oxygen quenching.

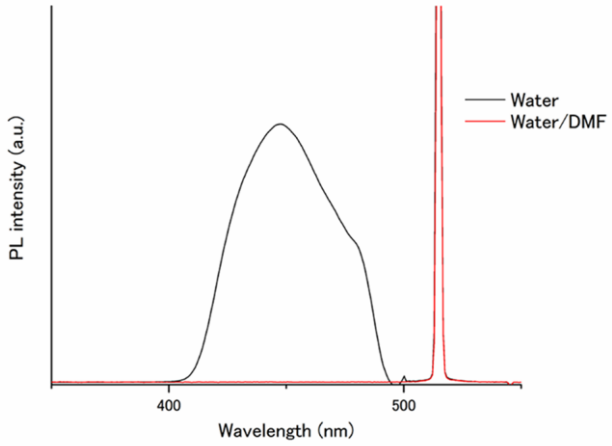

Figure 2-12. Photoluminescence spectra of **A1**–PtP4COONa ([**A1**] = 1 mM, [PtP4COONa] = 1 mM) in aerated water (black) and water/DMF (red) (λ_{ex} = 515 nm, excitation intensity = 1.3 W cm^{-2}). Scattered incident light was removed by a 490 nm short-pass filter.

Furthermore, the observed air stability of **A1**–PtP4COONa in pure water is in stark contrast to the control system without hydrogen bond networks, **A2**–PtP4COONa, for which the UC emission was completely quenched in aerated water similar to the case of **A2**–PtOEP. These results clearly demonstrate the proper amphiphilic molecular design of acceptor chromophores with dense intermolecular networks such as hydrogen bonds to achieve the air-stable TEM-UC aqueous system.

2.4 Conclusion

A supramolecular TEM-UC system showing an air-stable UC emission in an aqueous environment was developed for the first time. The rational design guideline to achieve this goal is demonstrated; the penetration of oxygen molecules is effectively blocked by the dense intermolecular networks driven by hydrogen bonding interactions in the hydrophobic environment of the acceptor self-assemblies. The stabilized acceptor triplets, sensitized by the co-assembled donor, migrate in the acceptor arrays and annihilate to produce efficient UC emission. The chromophores self-assembled in the hydrophobic interior with developed hydrogen bond networks of aqueous assembly systems thus are less influenced by dissolved molecular oxygen, which provides a new perspective in the design of photochemical or photophysical functions that require the interplay of reactive photo-generated species as observed in natural thylakoid membranes.

References

(1) Baluschev, S.; Miteva, T.; Yakutkin, V.; Nelles, G.; Yasuda, A.; Wegner, G. *Phys. Rev. Lett.* **2006,** *97*, 143903.

(2) Singh-Rachford, T. N.; Castellano, F. N. *Coord. Chem. Rev.* **2010,** *254*, 2560-2573.

(3) Monguzzi, A.; Bianchi, F.; Bianchi, A.; Mauri, M.; Simonutti, R.; Ruffo, R.; Tubino, R.et al. *Adv. Energy Mater.* **2013,** *3*, 680-686.

(4) Schulze, T. F.; Schmidt, T. W. *Energy Environ. Sci.* **2015,** *8*, 103-125.

(5) Zhou, J.; Liu, Q.; Feng, W.; Sun, Y.; Li, F. *Chem. Rev.* **2015,** *115*, 395-465.

(6) Wong, K. L.; Law, G. L.; Kwok, W. M.; Wong, W. T.; Phillips, D. L. *Angew. Chem. Int. Ed.* **2005,** *44*, 3436-3439.

(7) Haase, M.; Schafer, H. *Angew. Chem. Int. Ed.* **2011,** *50*, 5808-5829.

(8) Tanaka, K.; Inafuku, K.; Chujo, Y. *Chem. Commun.* **2010,** *46*, 4378-4380.

(9) Zhao, J.; Ji, S.; Guo, H. *RSC Adv.* **2011,** *1*, 937-950.

(10) Monguzzi, A.; Tubino, R.; Hoseinkhani, S.; Campione, M.; Meinardi, F. *Phys. Chem. Chem. Phys.* **2012,** *14*, 4322-4332.

(11) Simon, Y. C.; Weder, C. *J. Mater. Chem.* **2012,** *22*, 20817-20830.

(12) Duan, P.; Yanai, N.; Kimizuka, N. *J. Am. Chem. Soc.* **2013,** *135*, 19056-19059.

(13) Schmidt, T. W.; Castellano, F. N. *J. Phys. Chem. Lett.* **2014,** *5*, 4062-4072.

(14) Askes, S. H. C.; Bahreman, A.; Bonnet, S. *Angew. Chem. Int. Ed.* **2014,** *53*, 1029-1033.

(15) Duan, P.; Yanai, N.; Nagatomi, H.; Kimizuka, N. *J. Am. Chem. Soc.* **2015,** *137*, 1887-1894.

(16) Kim, J.-H.; Deng, F.; Castellano, F. N.; Kim, J.-H. *Chem. Mater.* **2012,** *24*, 2250-2252.

(17) Kim, J.-H.; Kim, J.-H. *J. Am. Chem. Soc.* **2012,** *134*, 17478-17481.

(18) Jiang, Z.; Xu, M.; Li, F.; Yu, Y. *J. Am. Chem. Soc.* **2013,** *135*, 16446-16453.

(19) Kim, J.-H.; Deng, F.; Castellano, F. N.; Kim, J.-H. *ACS Photonics* **2014,** *1*, 382-388.

(20) Svagan, A. J.; Busko, D.; Avlasevich, Y.; Glasser, G.; Baluschev, S.; Landfester, K. *ACS Nano* **2014,** *8*, 8198–8207

(21) Kim, J.-H.; Kim, J.-H. *ACS Photonics* **2015,** *2*, 633-638.

(22) Liu, Q.; Yin, B.; Yang, T.; Yang, Y.; Shen, Z.; Yao, P.; Li, F. *J. Am. Chem. Soc.* **2013,** *135*, 5029-5037.

(23) Marsico, F.; Turshatov, A.; Pekoz, R.; Avlasevich, Y.; Wagner, M.; Weber, K.; Donadio, D.et al. *J. Am. Chem. Soc.* **2014,** *136*, 11057-11064.

(24) Askes, S. H. C.; Mora, N. L.; Harkes, R.; Koning, R. I.; Koster, B.; Schmidt, T.; Kros, A.et al. *Chem. Commun.* **2015,** *51*, 9137-9140.

(25) Kwon, O. S.; Song, H. S.; Conde, J.; Kim, H. I.; Artzi, N.; Kim, J. H. *ACS Nano* **2016,** *10*, 1512-1521.

(26) Kim, H.-i.; Kwon, O. S.; Kim, S.; Choi, W.; Kim, J.-H. *Energy Environ. Sci.* **2016,** *9*, 1063-1073.

(27) Laquai, F.; Wegner, G.; Im, C.; Busing, A.; Heun, S. *J. Appl. Phys.* **2005,** *123*, 074902.

(28) Ogawa, T.; Yanai, N.; Monguzzi, A.; Kimizuka, N. *Sci. Rep.* **2015,** *5*, 10882.

(29) Hisamitsu, S.; Yanai, N.; Kimizuka, N. *Angew. Chem. Int. Ed.* **2015,** *54*, 11550-11554.

(30) Hosoyamada, M.; Yanai, N.; Ogawa, T.; Kimizuka, N. *Chem. - Eur. J.* **2016,** *22*, 2060-2067.

(31) Yanai, N.; Kimizuka, N. *Chem. Commun.* **2016,** *52*, 5354-5370.

(32) Kunitake, T. *Angew. Chem. Int. Ed.* **1992,** *31*, 709-726.

(33) Nakashima, T.; Kimizuka, N. *Adv. Mater.* **2002,** *14*, 1113-1116.

(34) Nishiyabu, R.; Aime, C.; Gondo, R.; Noguchi, T.; Kimizuka, N. *Angew. Chem. Int. Ed.* **2009,** *48*, 9465-9468.

(35) Okahata, Y.; Kunitake, T. *J. Am. Chem. Soc.* **1979,** *101*, 5231-5234.

(36) Shimomura, M.; Hashimoto, H.; Kunitake, T. *Chem. Lett.* **1982**, 1285-1288.

(37) Fuhrhop, J.-H.; Fritsch, D. *Acc. Chem. Res.* **1986,** *19*, 130-137.

(38) Kimizuka, N.; Kawasaki, T.; Hirata, K.; Kunitake, T. *J. Am. Chem. Soc.* **1998,** *120*, 4094-4104.

(39) Feng, D.; Gu, Z. Y.; Li, J. R.; Jiang, H. L.; Wei, Z.; Zhou, H. C. *Angew. Chem. Int. Ed.* **2012,** *51*, 10307-10310.

(40) Maeda, Y.; Higuchi, T.; Ikeda, I. *Langmuir* **2000,** *16*, 7503-7509.

(41) Onoda, A.; Yamada, Y.; Doi, M.; Okamura, T.-a.; Ueyama, N. *Inorg. Chem.* **2001,** *40*, 516-521.

(42) Harada, N.; Takuma, Y.; Uda, H. *J. Am. Chem. Soc.* **1978,** *100*, 4029-4036.

(43) Pope, M.; Swenberg, C. E. In *Electric Processes In Organic Crystals and Polymers*; 2nd ed.; Oxford University Press: New Yrok, 1999.

(44) Monguzzi, A.; Mezyk, J.; Scotognella, F.; Tubino, R.; Meinardi, F. *Phys. Rev. B* **2008,** *78*, 195112.

(45) Gray, V.; Dzebo, D.; Abrahamsson, M.; Albinsson, B.; Moth-Poulsen, K. *Phys. Chem. Chem. Phys.* **2014,** *16*, 10345-10352.

Chapter 3 Supramolecular Crowding Can Avoid Oxygen Quenching of Photon Upconversion in Water

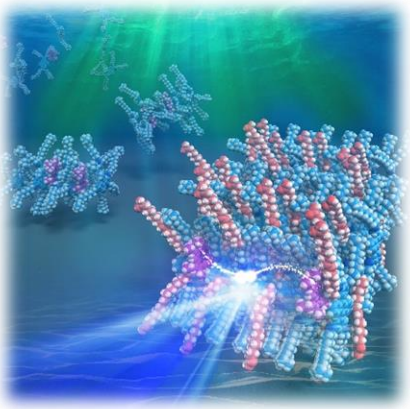

ABSTRACT: A common challenge in chemistry that deals with photo-excited states is to avoid oxygen quenching. This is crucial for hot research fields such as photon upconversion (UC), in which oxygen-sensitive triplet excited states play pivotal roles. However, methods to avoid oxygen quenching in aqueous media are far more limited despite eagerly anticipated catalytic and biological applications. This work introduces a simple strategy to achieve air-stable triplet–triplet annihilation (TTA)-based UC in water, namely, supramolecular crowding. Amphiphilic cationic acceptor molecules and anions with long alkyl chains co-assemble in water in which hydrophobic donor molecules are molecularly dispersed. Despite the common notion that oxygen molecules diffuse readily across hydrophobic domains in water, more than 80% of the TTA-UC emission of the obtained hydrophobic co-assemblies is maintained in air-saturated water. This work demonstrates the new promising potential of supramolecular chemistry for photo-physical and photochemical functions with oxygen-sensitive species.

3.1 Introduction

Efficient utilization of light energy is indispensable in photon science and technology, such as the conversion of photon energy to electrical/chemical energy. Controlling energy landscapes of the photo-excited states is at the heart of all these disciplines, and a molecule-based methodology to protect the excited states from the quenching by molecular oxygen is highly coveted. For example, the triplet excited states of organic molecules have received increased attention in the research fields of triplet–triplet annihilation-based photon upconversion (TTA-UC),[1-19] singlet fission,[20-22] and organic light emitting diodes.[23,24] All these studies suffer from overwhelming deactivation of excited triplets by molecular oxygen, which severely limits their operation to strictly deaerated conditions. In solid-state device applications, there are established techniques for this. On the other hand, methods to achieve oxygen tolerance in the solution phase are far more limited, although nano- and microscale photofunctional materials with excellent, long-term air stability are highly coveted for biological and photocatalytic applications in aqueous media.

Nonpolar oxygen molecules show higher solubility in nonpolar organic solvents than in water,[25] and consequently, it has been customarily assumed that oxygen dissolves and diffuses readily across cellular lipid membranes in a similar way as in bulk hydrocarbon solvents. Indeed, studies on oxygen transport across model and plasma membranes showed that membranes are in general not barriers to oxygen transport into the cell.[26] Meanwhile, oxygen concentration is known to be low in some tissues, notably fiber cells of the eye lens, in which the lens nuclei are protected from oxidative damage and cataracts.[27,28] The plasma membranes of these fiber cells show extremely high cholesterol content, which is considered to ensure the rigidity of the membrane that contributes to reducing its oxygen permeability.[27,28] Recent atomic-scale molecular dynamics investigations suggest that the close packing of cholesterol molecules and phospholipids generates a physical barrier to oxygen diffusion at the membrane interfaces.[27-29]

Inspired by the suppressed oxygen permeability in the lens lipid membrane system, we hypothesized that, even in artificial systems, the reinforcement of molecular self-assembly may lead to the suppression of oxygen partition if the intermolecular interactions and molecular density are enhanced to constitute an energy barrier to oxygen diffusion. To prove this hypothesis, we designed a new amphiphilic acceptor for TTA-UC in aqueous media and investigated the effect of introducing hydrophobic counterions on their self-assembly and TTA-UC characteristics.

TTA-UC is a wavelength-upshifting technology that can utilize noncoherent and low-intensity light sources. As summarized in Section 1-2, TTA-UC is a multicomponent system

that usually consists of hydrophobic donor and acceptor. First, the excited triplet donor is generated by intersystem crossing from the photo-excited singlet state. This triplet excited energy is transferred through triplet–triplet energy transfer (TTET) to the acceptor. Two sensitized acceptor triplets generate a higher excited singlet state through TTA, which consequently produces a delayed fluorescence. The TTET and TTA processes occur by an electron-exchange Dexter mechanism, which requires the involved molecules to approach one another within a distance of 1 nm. Although studies on TTA-UC have been carried out in organic media,[1-3,5-7,13,15,16] it is a challenge to develop useful methodologies to achieve TTA-UC in aqueous media. Aqueous TTA-UC has great potential for applications such as high-contrast bioimaging, photo-triggered drug-delivery systems, and photodynamic therapy.[4,8,30-38]

One of the serious problems of aqueous TTA-UC is quenching of excited triplet states by dissolved molecular oxygen. Although the suppression of oxygen quenching has been reported in several host–guest systems,[39-42] these works mainly focused on the single-exciton phosphorescence process and their design concept can not be simply extended to multi-exciton TTA-UC, which requires triplet exciton diffusion in multi-chromophore systems. By encapsulating UC chromophores in viscous organic liquids or rubbery matrices, oxygen diffusion was slowed down.[4,31,32,36] The addition of an oxygen scavenger further reduced the oxygen concentration in these matrices. However, these viscous liquids and matrices inevitably restrict the molecular diffusion of the chromophores as well, which intrinsically limits the efficiency of TTET and TTA processes.

We have previously reported an alternative strategy that harnesses triplet-energy migration in self-assembled acceptor chromophores in aqueous and organic media.[13,35,43,44] The amphiphilic cationic acceptors self-assembled in water through hydrophobic and hydrogen-bonding interactions, and the hydrogen-bonding networks were presumed to limit diffusion of oxygen molecules into the hydrophobic chromophore layer (Chapter 2).[35] However, about half of the UC emission was still quenched by dissolved oxygen, and it is difficult to separate the contribution of hydrogen bonding from the effect of molecular stacking. Thus, the understanding of the decreased oxygen quenching remains evasive, and it is necessary to develop new aqueous self-assembly systems that allow a better understanding of the oxygen screening effect and its improvement.

Herein, we demonstrate a simple strategy, namely, electrostatic supramolecular crowding, to achieve air-stable TTA-UC by reinforcing amphiphilic chromophore self-assemblies in water. Amphiphilic cationic acceptor **A2** was designed on the basis of 9,10-diphenylanthracene (DPA). Four quaternary ammonium groups were attached to the hydrophobic DPA chromophore through alkyl-chain spacers to ensure dispersibility in water (Figure 3-1).[45-47] Acceptor **A2** does not contain hydrogen-bonding units, and we show that the intermolecular interactions and molecular density are tunable by introducing hydrophobic counterions.[48,49]

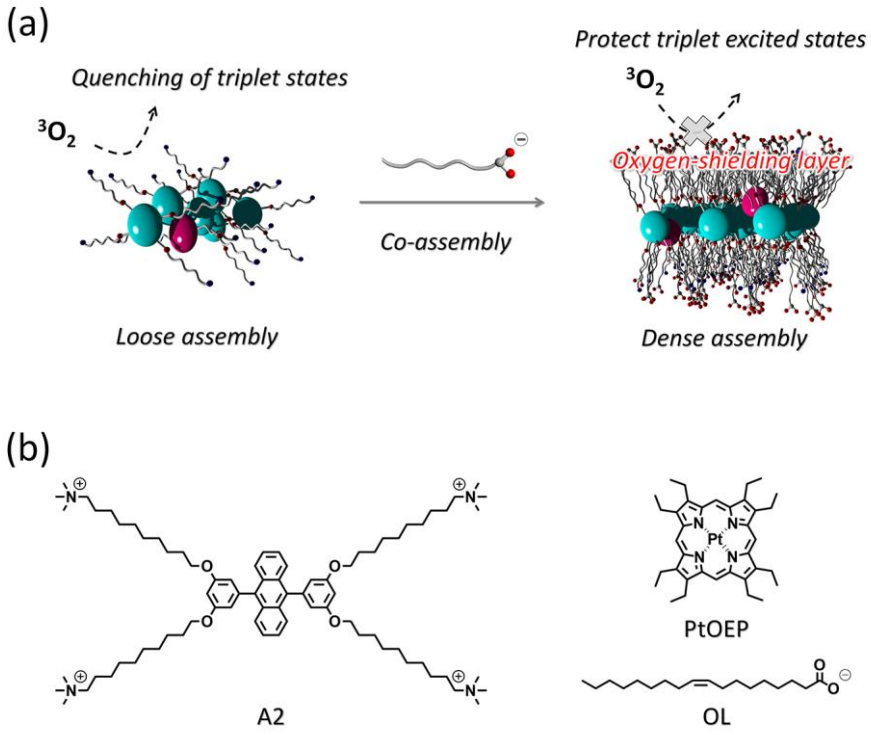

Figure 3-1. (a) Schematic illustration of the aqueous TTA–UC molecular system and oxygen-shielding property. Addition of OL anions to the cationic acceptor self-assemblies gives hydrophobic ion pairs. This shields the electrostatic repulsion between the cationic groups, and the resultant structural transformation into dense molecular assemblies leads to interfacial supramolecular crowding, which effectively shields the triplet excited states from quenching by dissolved oxygen in water (acceptor: blue, donor: red, and alkyl anion: gray). (b) Chemical structure of **A2**, PtOEP and OL.

Acceptor **A2** was mixed with fatty-acid anions with various structures to systematically elucidate the relationship between the molecular density around the chromophores and the oxygen-shielding effect (Figure 3-1). By molecularly dispersing donor PtOEP into the **A2**/fatty acid co-assemblies, more than 80% of TTA-UC emission was maintained in air-saturated water relative to that observed in deaerated water. The origin of this high oxygen-shielding ability was attributed to the hydrophobic counterions, which enhance the intermolecular interactions of **A2** by shielding electrostatic repulsions between the ammonium head groups. This simultaneously enhances the molecular density both at the surface of the **A2**/fatty acid co-assemblies and around the chromophores, and thus provides a physical energy barrier for partitioning of molecular oxygen from the bulk aqueous phase. This work presents a rational method to protect triplet states from oxygen quenching in aqueous self-assemblies.

3.2 Experimental section

3.2.1 General methods

Characterizations

^{1}H NMR (300 MHz) spectra were measured on a Bruker DRX-spectrometer using TMS as the internal standard. Elemental analysis was conducted at the Elemental Analysis Center, Kyushu University. UV-vis absorption spectra were recorded on a JASCO V-670 and V-770 spectrophotometer. Luminescence spectra were measured by using a PerkinElmer LS 55 fluorescence spectrometer. Time-resolved fluorescence lifetime measurements were carried out by using time-correlated single photon counting lifetime spectroscopy system, HAMAMATSU Quantaurus-Tau C11367-02 (for fluorescence lifetime)/C11567-01(for delayed luminescence lifetime). The quality of the fit was judged by the fitting parameters such as χ^2 (<1.2) as well as the visual inspection of the residuals. The absolute photoluminescence quantum yield was measured in an integrating sphere using a Hamamatsu Photonics absolute quantum yield measurement system. Transmission electron microscopy (TEM) images were measured by using JOEL JEM-2010. Dynamic light scattering measurements were carried out by using Malvern Nano-ZS ZEN3600. Confocal laser scanning microscope (CLSM) imaging was performed on a Carl Zeiss LSM 510 confocal microscope. The aqueous dispersion sample was prepared on glass-bottomed dishes (Matsunami Glass Ind., Ltd.). Blue fluorescence images were obtained through a 420 nm long-pass filter using a blue diode laser at λ_{ex} = 405 nm.

To measure TTA-UC emission spectra, a diode laser (532 nm, 200 mW, RGB Photonics) was used as an excitation source. The laser power was controlled by combining a software (Ltune) and a variable neutral density filter and measured using a PD300-UV photo-diode sensor (OPHIR Photonics). The laser beam was focused on a sample using a lens. The diameter of the laser beam ($1/e^2$) was measured at the sample position using a CCD beam profiler SP620 (OPHIR Photonics). A typical area of laser irradiation spot estimated from the diameter was 0.39×10^{-3} cm^2. The emitted light was collimated by an achromatic lens, the excitation light was removed using a notch filter (532 nm), and the emitted light was again focused by an achromatic lens to an optical fiber connected to a multichannel detector MCPD-9800 which was supplied and calibrated by Otsuka Electronics and equipped with a CCD sensor for the detection of whole visible range with high sensitivity.

Determination of TTA-UC quantum yield

In general, the quantum yield is defined as the ratio of absorbed photons to emitted photons, and thus the maximum quantum yield (Φ_{UC}) of the bimolecular TTA-UC process is 50%. However, many reports multiply this value by 2 to set the maximum efficiency at 100%. To avoid the confusion between these different definitions, the UC efficiency is written as Φ_{UC}' (= $2\Phi_{UC}$) when its maximum is normalized to be 100%. The UC efficiency in deaerated and aerated condition was determined relative to a standard (Rhodamine B in water, Φ_{std} = 0.35) according to the following equation,[2]

$$\Phi_{UC}' = 2\Phi_{std}(\frac{A_{std}}{A_{UC}})(\frac{I_{std}}{I_{UC}})(\frac{F_{UC}}{F_{std}})$$

where Φ, A, I, and F represent the quantum yield, absorbance at 532 nm, excitation intensity, and integrated photoluminescence spectral profile. The subscripts UC and std denote the parameters of the upconversion and standard systems.

3.2.2 Materials

All reagents and solvents for synthesis were used as received without further purification. Pt (II) octaethylporphyrin (PtOEP) was purchased from Sigma-Aldrich. Sodium oleate was synthesized according to the reported methods.[50] Sodium decanoate and sodium stearate were purchased from TCI and sodium propionate was from KISHIDA, respectively. The acceptor (**A2**) was synthesized and fully characterized (Scheme 2-2). Analytical grade methanol was purchased from Wako Pure Chemical and deionized water was generated by Direct-Q UV (Merck Millipore). For sample preparation of TTA-UC measurements, all the solids (**A2** and PtOEP with/without alkyl anion) were first dissolved in methanol. After evaporating methanol, deionized water was added, and the water dispersions were generated via ultrasonication. The deaeration of the aqueous dispersion was conducted by repeated freeze-pump-thaw cycles.

3.3 Results and discussion

3.3.1 Co-assembly behavior of A2-oleate system in water

Amphiphilic acceptor **A2** was synthesized and fully characterized. Self-assembly of **A2** in water was studied by dynamic light scattering (DLS), TEM, and ^{1}H NMR, absorption, and fluorescence spectroscopy. TEM and DLS studies on an aqueous dispersion of **A2** ([**A2**] = 1 mM) showed round nanostructures with an average size of about 100 nm (Figure 3-2a and b). ^{1}H NMR spectra of 1 mM **A2** in D_2O showed broad peaks at 293 K, and the sharpening of the peaks at higher temperature (353 K) indicated disassembly of the supramolecular structure by heating (Figure 3-2c). The absorption spectrum of **A2** in water ([**A2**] = 1 mM) at ambient temperature exhibited a π–π^* transition band at 261 nm, which is redshifted relative to that in DMF solution (λ_{max} = 259 nm, monomeric species). In addition, this band in water showed considerable hypochromism with spectral broadening. (Figure 3-2d) This band corresponds to the transition dipole polarized along the long axis of the anthracene moiety,[51] and the observed redshift indicates the presence of electronic interactions between DPA units in pure **A2** assemblies.

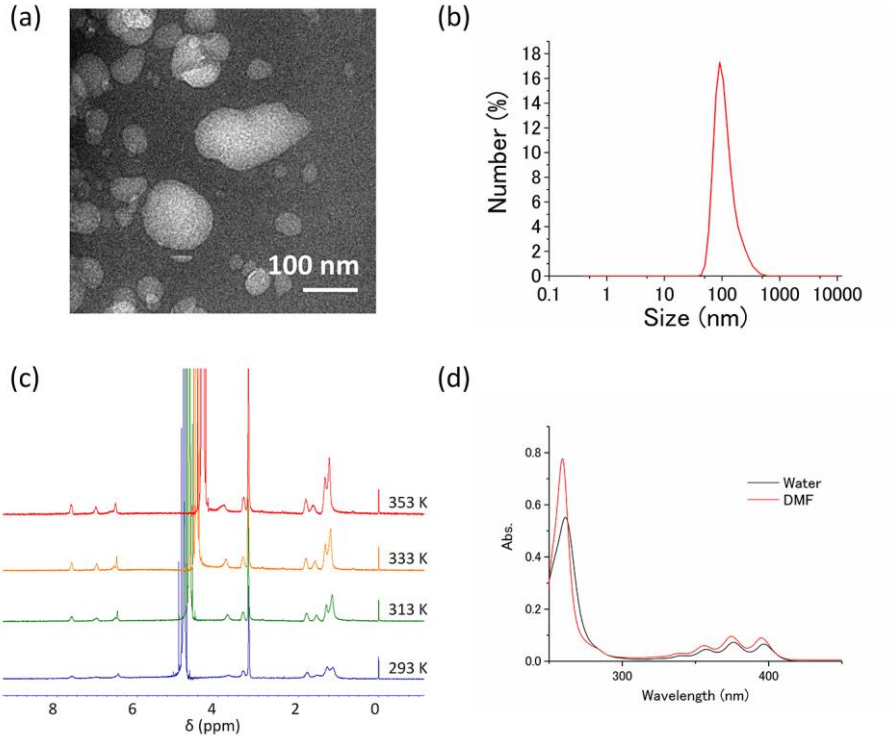

Figure 3-2. (a) Transmission electron microscopy (TEM) image of **A2**. The 1 mM aqueous solution of **A2** was cast on a TEM grid, and the sample was post-stained with aqueous 2 wt% uranyl acetate. (b) DLS profile of **A2** in water ([**A2**] = 1 mM) at room temperature. (c) Temperature-dependent ^{1}H NMR spectra in D_2O ([**A2**] = 1 mM, DSS (Sodium 2,2-Dimethyl-2-silapentane-5-sulfonate) was used as internal standard). Broad peaks became sharper as temperature increased from 293 K to 353 K. (d) Absorption spectra of **A2** in water and in DMF ([**A2**] = 1 mM) at room temperature.

The aqueous **A2** assemblies showed a blue and structured fluorescence band around at 440 nm (Figure 3-3). Notably, the supramolecular assemblies of **A2** showed a high fluorescence quantum yield Φ_{FL} of 92.3% which is ascribed to the steric hindrance of twisted phenyl rings attached to anthracene moiety, which prevented the formation of nonradiative aggregates serving as energy traps.[52,53]

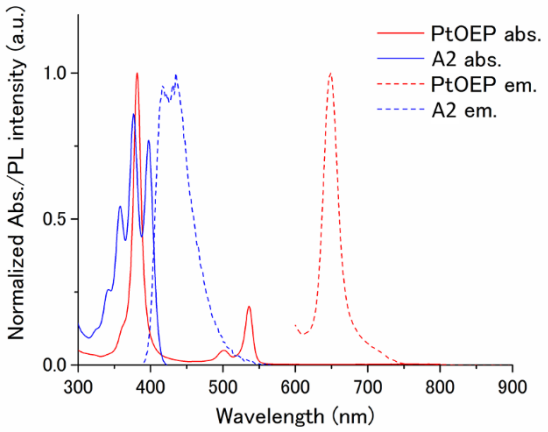

Figure 3-3. Normalized absorption (solid lines) and emission (dashed lines) spectra of **A2** in water (blue, λ_{ex} = 380 nm, [**A2**] = 1 mM) and PtOEP in chloroform (red, λ_{ex} = 532 nm, [PtOEP] = 10 μM) at room temperature.

The structural transformation by co-assembly of **A2** and sodium oleate (OL) was visibly discernible. Transparent aqueous dispersions were obtained for the single-component aggregates of **A2** ([**A2**] = 10 mM) or OL ([OL] = 40 mM). The concentration of aqueous OL (40 mM) employed was well above the critical micelle concentration of OL (cmc = 1–2 mM).[54] The aqueous mixture of **A2** and OL gave a turbid dispersion ([**A2**]=10 mM, [OL] = 40 mM, Figure 3-4a). The observed change is caused by electrostatic binding of OL to cationic **A2**, since the zeta potential ξ of +53.4 mV for aqueous **A2** decreased to +9.74 mV on addition of OL. The co-assembly of **A2** and OL was also confirmed by ^{1}H NMR spectra (Figure 3-4a). The NMR peaks of the **A2**–OL mixture were broader and shifted compared with those of single-component aqueous dispersions of **A2** or OL. In confocal laser micrographs, microparticles with an average size of about 2.5 μm were observed for the **A2**–OL co-assemblies (Figure 3-4b), which are larger than the DLS diameter observed for pure **A2** assemblies (~ 100 nm, Figure 3-2a). These observations indicate that the electrostatic binding of OL to **A2** gave hydrophobic ion pairs, which effectively shielded electrostatic repulsion between ammonium groups, and the consequent increase in intermolecular interactions caused structural transformation into larger assemblies, as was visually confirmed.[48,49]

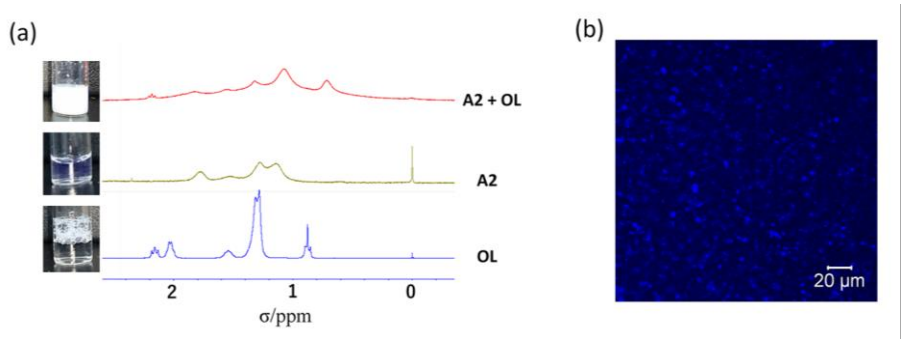

Figure 3-4. (a) ^{1}H NMR spectra of the alkyl region and photographs of **A2**–OL mixture, **A2**, and OL (red: [**A2**] = 10 mM and [OL] = 40 mM in D_2O, ocher: [**A2**] = 10 mM in D_2O, blue: [OL] = 40 mM in D_2O; DSS was used as internal standard). (b) Confocal laser micrograph of of aqueous **A2**–OL ([**A2**] = 10 mM and [OL] = 40 mM in water).

3.3.2 Comparison of TTA-UC properties between A2-PtOEP and A2-PtOEP-OL

The UC properties of the binary **A2**–PtOEP pair were examined in deaerated water. An aqueous dispersion ([**A2**] = 10 mM, [PtOEP] = 10 μM) was deaerated by repeated freeze–pump–thaw cycles. Under excitation by a 532 nm laser, the deaerated **A2**–PtOEP dispersion showed a blue UC emission at 440 nm (Figure 3-5a), which is consistent with the fluorescence peak position (440 nm). Similarly, the ternary dispersion of **A2**–PtOEP–OL ([**A2**] = 10 mM, [PtOEP] = 10 μM, [OL] = 40 mM) in deaerated water also showed an UC emission at 440 nm (Figure 3-6a).

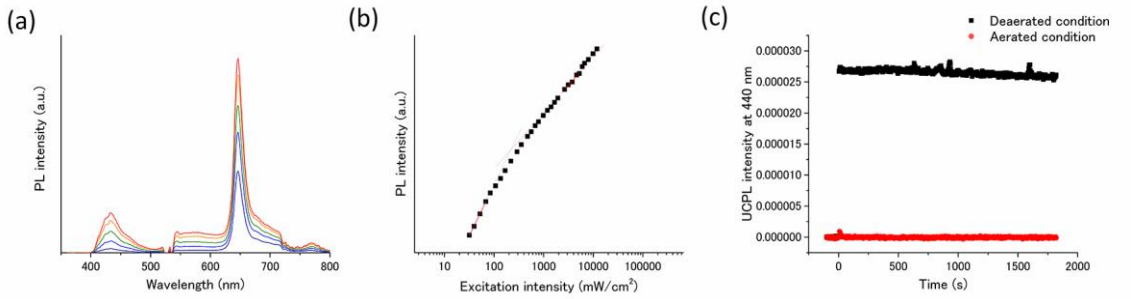

Figure 3-5. (a) Photoluminescence spectra of **A2** (10 mM)- PtOEP (10 μM) in deaerated water at different excitation intensities of 532 nm laser with 532 nm notch filter. (b) UC emission intensity at 440 nm of **A2** (10 mM) and PtOEP (10 μM) in deaerated water as a function of the excitation intensity. The solid blue and red lines were fitting results with the slopes of 1.8 and 1.0. (c) Time dependence of the UC emission intensity of **A2** (10 mM) and PtOEP (10 μM) at 440 nm in deaerated (black) and aerated (red) water upon continuous excitation at 532 nm with a laser light intensity of 3.4 W cm^{-2}.

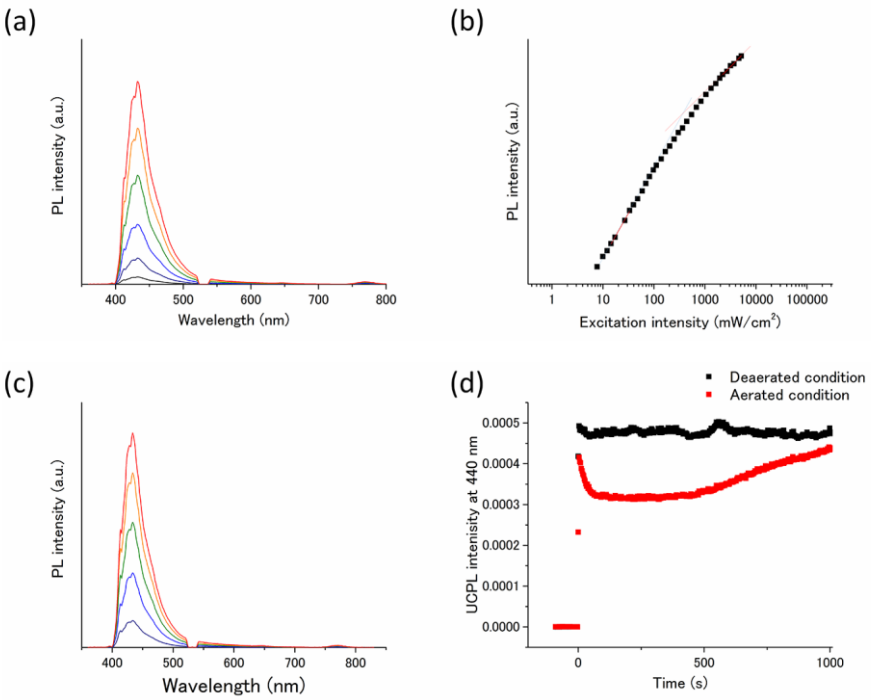

Figure 3-6. UC properties of **A2** (10 mM)- PtOEP (10 μM)- OL (40 mM) in water. (a) Photoluminescence spectra of **A2** (10 mM), PtOEP (10 μM) and OL (40 mM) in deaerated water with different excitation intensity of 532 nm laser with 532 nm notch filter. (b) UC emission intensity of **A2** (10 mM), PtOEP (10 μM) and OL (40 mM) at 440 nm as a function of the excitation intensity. The solid blue and red lines were fitting results with the slopes of 1.9 and 1.1. (c) Photoluminescence spectra of **A2** (10 mM), PtOEP (10 μM) and OL (40 mM) in aerated water. (d) Time dependence of the UC emission intensity of **A2** (10 mM), PtOEP (10 μM) and OL (40 mM) at 440 nm in deaerated (black) and aerated (red) water upon continuous excitation at 532 nm with laser light intensity of 3.7 W cm^{-2}. The increase in UCPL intensity under aerated condition after ca. 500 s is ascribed to consumption of dissolved molecular oxygen in the system.

3.3.3 TTA-UC properties of A2-PtOEP-OL ternary system

The TTA-based UC mechanism of the deaerated **A2**–PtOEP and **A2**–PtOEP–OL aqueous dispersions were confirmed by the excitation intensity dependence of the UC emission intensity and by the UC emission decays. In general, the intensity of the TTA-UC emission shows quadratic and linear dependences on the incident light intensity in the regimes of low and high excitation intensity, respectively. A double logarithmic plot of the UC emission intensity of the aqueous dispersions as a function of incident light intensity showed a transition from a slope of about 2 to 1, which provides evidence for TTA-based UC (Figures 3-5b and 6b). The TTA-based mechanisms were further supported by the decay of UC emission, which typically occurs on the millisecond timescale and reflects the generation of the singlet state via a long-lived triplet state. The TTA-based delayed fluorescence generally shows a non-exponential decay, but its tail part exhibits single exponential behavior that reflects the triplet lifetime.[55,56] The long acceptor triplet lifetimes $\tau_{A,T}$ of 0.45 and 1.67 ms that were obtained for deaerated aqueous dispersions of **A2**–PtOEP and **A2**–PtOEP-OL, respectively, are consistent with the TTA-UC mechanism. The UC efficiencies Φ_{UC} of the deaerated dispersion of **A2**–PtOEP–OL were further determined by a relative method (see section 3.2.1). A remarkably high Φ_{UC} value of 19.8% was observed for aqueous **A2**–PtOEP–OL at an excitation intensity of 3.9 Wcm^{-2}. This is the highest UC efficiency so far in aqueous systems. The remarkably high UC efficiency in the ternary dispersion is attributed to the high fluorescence quantum yield of the acceptor and the efficient TTET. The absence of the PtOEP phosphorescence for aqueous **A2**–PtOEP–OL indicates almost 100% donor-to-acceptor TTET efficiency (Figure 3-6a). Thus, flexible OL molecules introduced as counterions promote solubilization of PtOEP in the vicinity of the DPA chromophores. It is also noteworthy that the addition of PtOEP did not change the fluorescence lifetime of **A2**–OL; this suggests that singlet energy back-transfer from **A2** to PtOEP is well circumvented in aqueous **A2**–PtOEP–OL (Figure 3-7).

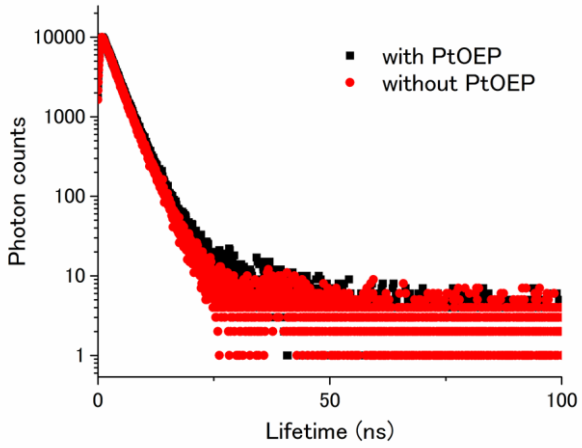

Figure 3-7. Fluorescence decays at 440 nm of **A2**-OL (red) and **A2**-PtOEP-OL (black) in air-saturated water under pulsed excitation at 365 nm ([**A2**] = 10 mM, [OL] = 40 mM, [PtOEP] = 10 μM). The lifetimes were 2.96 ns and 2.68 ns for **A2**-OL and A2-PtOEP-OL, respectively.

3.3.4 Oxygen-barrier efficiency of A2-PtOEP-OL ternary system

Although **A2**–PtOEP forms supramolecular nanoassemblies in water, its UC emission entirely disappeared in air-saturated water due to quenching of the excited triplet state by dissolved oxygen (Figure 3-8). Apparently, the molecular alignment in **A2**–PtOEP is not sufficient to shield DPA chromophores from molecular oxygen dissolved in the aqueous phase. This could be associated with the molecular design of **A2**. The hydrophobic DPA chromophore is connected to four cationic groups, the electrostatic repulsions of which overwhelm the hydrophobic association of the central DPA units. This loosens the molecular alignment, and, consequently, the spacer methylene groups connected to the highly hydrated ammonium groups exhibit enhanced micropolarity near the aggregate surface. A larger partition coefficient of oxygen to these molecular voids is expected, with a diffusion path possibly dominated by water.[27]

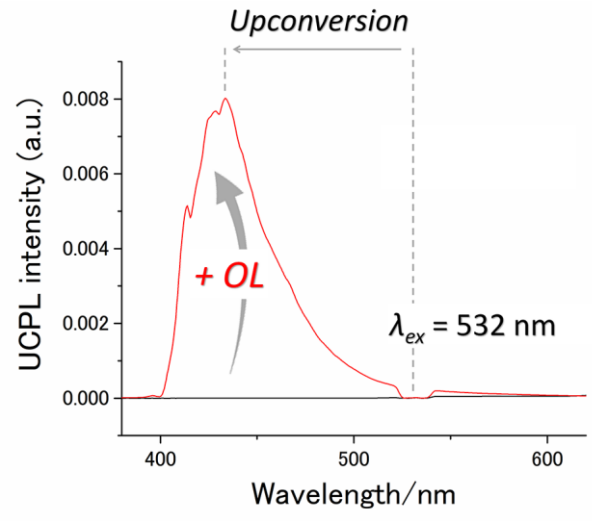

Figure 3-8. Photoluminescence spectra of **A2** and PtOEP with/without OL in aerated water. (black: [**A2**] = 10 mm, [PtOEP] = 10 mm; red: [**A2**] = 10 mm, [PtOEP] = 10 mm, [OL] = 40 mm), λ_{ex} = 532 nm, excitation intensity= 3.7 Wcm^{-2}. A notch filter at 532 nm was used to remove the scattered incident light.

In contrast, the mixed dispersion of **A2**–PtOEP–OL ([**A2**] = 10 mM, [PtOEP] = 10 μM, [OL] = 40 mM) showed stable UC emission even in air-saturated water (Figure 3-8). To estimate the oxygen-barrier efficiency, triplet lifetimes of **A2** were compared under deaerated and aerated conditions. Acceptor triplet lifetimes $\tau_{A,T}$ of 1.7 and 1.1 ms were observed for the deaerated and aerated dispersions, respectively (Figure 3-9a). From these values, the oxygen-barrier efficiency Φ_{OB} was estimated as $\Phi_{OB} = \tau_{A,T,aerated}/\tau_{A,T,deaerated}$ = 67%. A UC efficiency Φ_{UC}' in air-saturated water of 14.4% was achieved for the **A2**–PtOEP–OL dispersion (Figure 3-9b), and this value is comparable to the record Φ_{UC}' value in aerated aqueous systems.[36] The Φ_{OB} value was also estimated from the UC efficiency as $\Phi_{OB} = \Phi_{UC,aerated}/\Phi_{UC,deaerated}$ = 73 %. This Φ_{OB} value is close to that calculated from the triplet lifetime and thus supports the validity of the Φ_{OB} estimate.

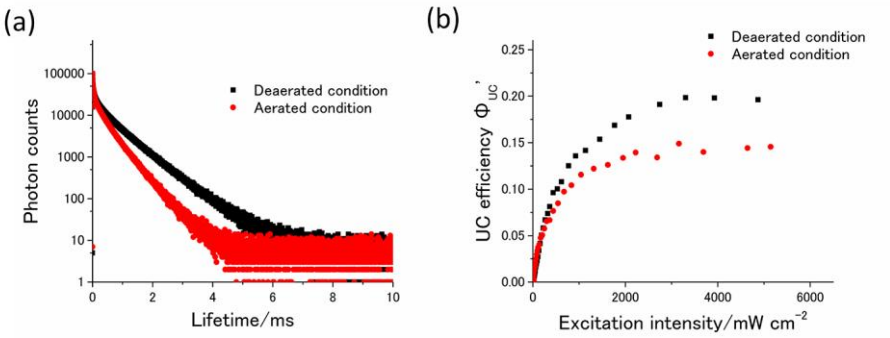

Figure 3-9. (a) UC emission decay at 440 nm of **A2**–PtOEP–OL in water under 531 nm pulsed excitation ([**A2**] = 10 mm, [PtOEP] = 10 μm, [OL] = 40 mm; black: deaerated and red: aerated conditions). (b) Dependence of UC efficiency Φ_{UC}' on the excitation intensity of **A2**–PtOEP–OL in water under ambient conditions ([**A2**] = 10 mm, [PtOEP] = 10 μm, [OL] = 40 mm; black: deaerated and red: aerated conditions; λ_{ex} = 532 nm).

This high oxygen-barrier ability was maintained under continuous laser excitation for 1000 s (Figure 3-6d). A similar time dependence of UC emission intensity was observed for repeated 10 min continuous laser excitation five times with 30 min intervals between measurements (Figure 3-10). After continuous excitation of an aqueous dispersion of **A2**-PtOEP-OL for 5 h with a 532 nm laser (I_{ex} = 3.7 Wcm^{-2}), water was removed by evaporation and [D7]DMF was added. The ^1H NMR spectrum of the resulting solution showed only small new peaks around 7.3 ppm (Figure 3-11). These results suggest that the oxygen quenching of triplet excited states is mainly physical with a minor contribution of chemical processes.[57] The highest Φ_{UC}' value in deaerated water together with the oxygen-shielding effect resulted in the remarkably high Φ_{UC}' value in air-saturated water.

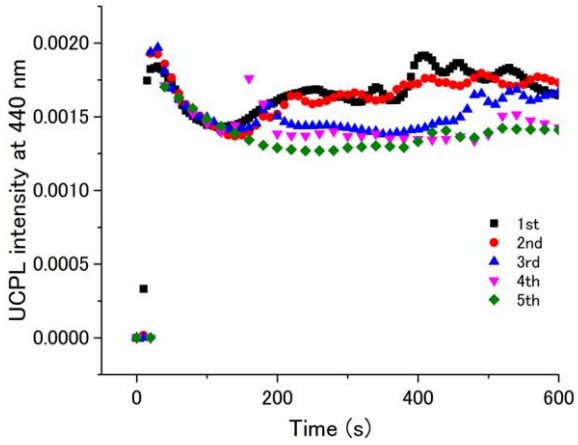

Figure 3-10. Time dependence of the UC emission intensity of **A2** (10 mM), PtOEP (10 μM) and OL (40 mM) at 440 nm in aerated water by repeated continuous excitation at 532 nm (I_{ex} = 3.7 W cm^{-2}) with 30 min intervals between each measurement.

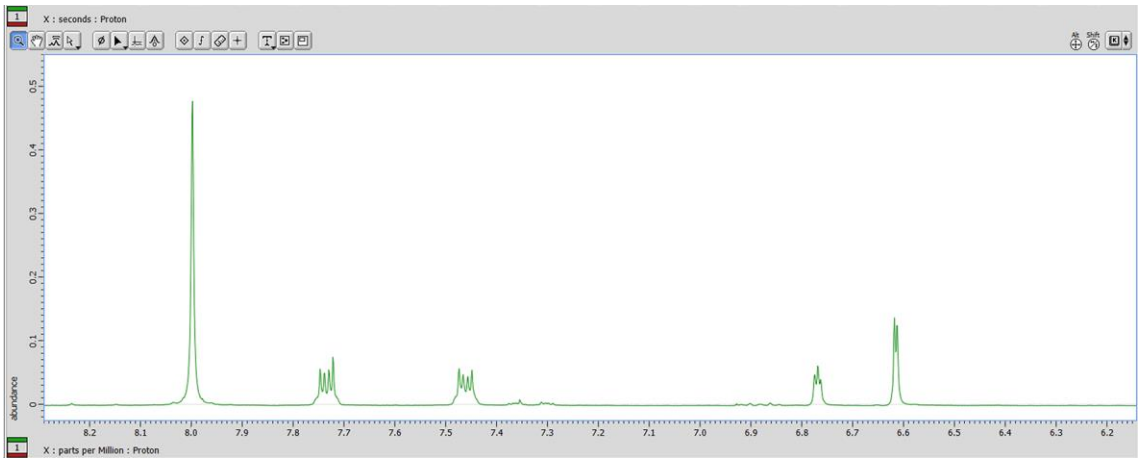

Figure 3-11. ^{1}H NMR spectrum of **A2**-OL-PtOEP in DMF-d7 after 5 hours of continuous 532 nm laser excitation (I_{ex} = 3.7 W cm^{-2}) in water.

3.3.5 Effect of double bond against oxygen-barrier properties

To better understand the mechanism of oxygen shielding, we first examined the effect of the double bond of OL. There have been some reports that OL works as an oxygen scavenger that allows TTA-UC emission in aerated specimens.[31,37,58] In these reports, OL was added in large excess compared with the chromophores to consume oxygen molecules by reaction with the double bonds. In contrast, only four equivalents of OL relative to **A2** were employed in our system. Furthermore, a similar Φ_{OB} value was observed when sodium stearate, which has no double bond in its structure, was used instead of OL (Figure 3-6 and Figure 3-12). This result clearly indicates the importance of hydrophobic ion pairing, which enhances the intermolecular interactions of **A2** and molecular density around the DPA chromophores, and not the consumption of oxygen by the chemical reaction. It explains the observed temporal stability of the TTA-UC emission (Figure 3-10). We used OL in the following experiments since **A2**–OL showed better dispersibility in water than **A2**–sodium stearate.

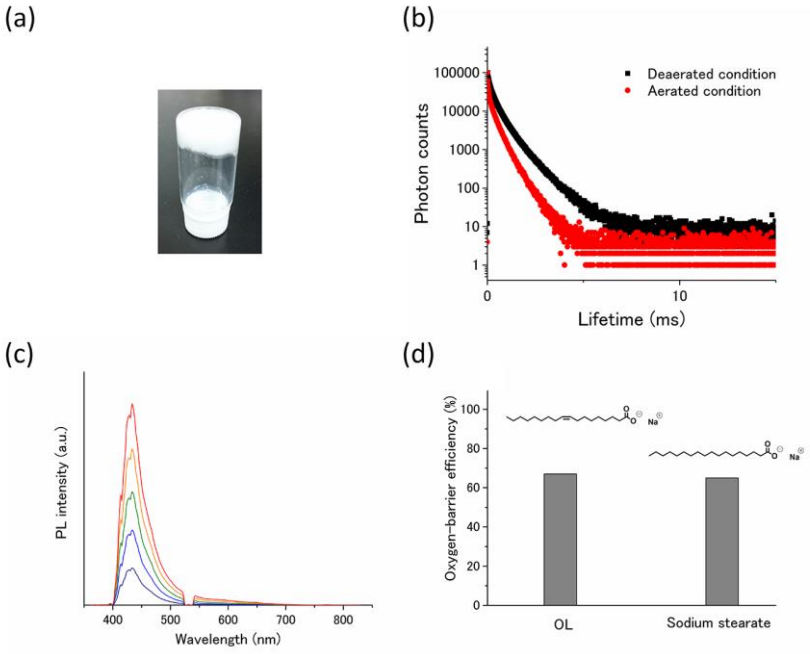

Figure 3-12. UC properties of **A2** (10 mM)-PtOEP (10 μM)-Sodium stearate (40 mM) in water. (a) A photograph of the sample that underwent physical gelation due to the strong hydrophobicity of stearate. (b) Photoluminescence spectra in deaerated water with different excitation intensity of 532 nm laser with 532 nm notch filter as a function of the excitation intensity. (c) UC emission decays at 440 nm in deaerated (black) and aerated (red) water under 531 nm pulsed excitation. (d) Dependence of Φ_{OB} on the presence (OL)/absence of a double bond (sodium stearate).

3.3.6 Relationship of oxygen-barrier properties against mixed ratio of oleate

We elucidated the critical role of alkyl-chain density in oxygen shielding by changing the alkyl-chain density and alkyl-chain length of fatty acids. To examine the effect of alkyl-chain density, different concentrations of OL (0, 20, 40, 80 mM) were added to a 10 mM aqueous dispersion of **A2**. We did not study higher concentrations of OL, because they decreased aqueous dispersibility. Interestingly, even the addition of two equivalents of OL led to an appreciable oxygen-barrier property, and higher concentrations of OL provided enhanced Φ_{OB} values (Figure 3-13, and Table 3-1).

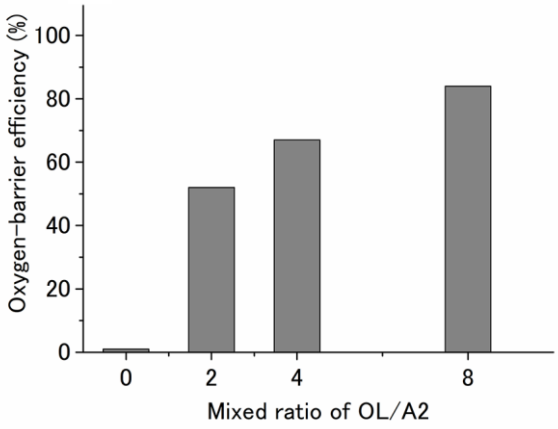

Figure 3-13. Dependence of Φ_{OB} on the OL/**A2** mixing ratio ([**A2**] = 10 mM; [PtOEP]=10 μM; [OL] = 0, 20, 40, 80 mM; system dispersed in water).

Table 3-1. Oxygen-shielding properties calculated from triplet lifetime of **A2** depend on mixed ratio of sodium oleate/**A2**. ([**A2**] = 10 mM, [PtOEP] = 10 μM and [OL] = 0, 20, 40, 80 mM in water)

		Mixed ratio of sodium oleate/A2			
		0	**2**	**4**	**8**
Triplet lifetime	**Deaerated sample**	**0.453**	**1.02**	**1.69**	**1.90**
(ms)	**Aerated sample**	**-**	**0.529**	**1.13**	**1.60**
	Oxygen-shielding efficiency	**0%**	**52%**	**67%**	**84%**

3.3.7 Relationship of oxygen-barrier properties against anion alkyl length

The effect of alkylchain length was investigated by adding 40 mM sodium propionate (C_3), decanoate (C_{10}), and stearate (C_{18}) to a 10 mM aqueous dispersion of **A2**. We observed a clear trend that longer alkyl chains of the fatty acid anion lead to higher Φ_{OB} (Figure 3-14 and Table 3-2). These results confirm that the hydrophobic counterions bind more efficiently, and the consequent ion paring with enhanced intermolecular interactions and molecular crowding around the DPA chromophores effectively reduces the access of oxygen. It is interesting that simple electrostatic complexation with hydrophobic anions and the resultant structural transformation in the co-assembly lead to excellent oxygen-barrier ability.

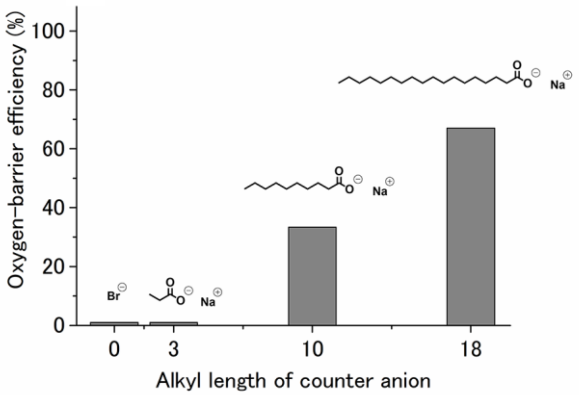

Figure 3-14. Dependence of Φ_{OB} on alkyl-chain length of the counteranion in water ([**A2**] = 10 mM, [PtOEP] = 10 μM, [sodium propionate, decanoate, stearate] = 40 mM).

Table 3-2. Oxygen-shielding properties calculated from triplet lifetime of **A2** depend on fatty acid alkyl length. ([**A2**] = 10 mM, [PtOEP] = 10 μM and [fatty acid anion] = 40 mM in water)

Added counter ion		**none**	**Propionate (C_3)**	**Decanoate (C_{10})**	**Oleate (C_{18})**
Triplet lifetime	**Deaerated sample**	**0.453**	**-** [a]	**1.40**	**1.69**
(ms)	**Aerated sample**	**-**	**-**	**0.47**	**1.13**
	Oxygen-shielding efficiency	**0%**	**0%**	**34%**	**67%**

[a]: The UC emission at 440 nm was not detected in the lifetime instrument. Meanwhile, the UC emission was observed in deaerated condition by 532 nm laser excitation. Therefore, the oxygen-barrier efficiency value of propionate was determined as 0%.

3.3.8 Relationship of oxygen-barrier properties against assembled size

This oxygen-shielding mechanism was further supported by reducing the size of UC assemblies. The nanosized assemblies (ca. 50 nm) obtained at a lower **A2**–OL concentration ([**A2**] = 1 mM, [PtOEP] = 1 μm, [OL] = 8 mM) also showed stable UC emission in air-saturated water (Φ_{OB} = 54%, Figure 3-15). The observed size dependence supports the hypothesis that the oxygen-barrier mechanism is based on suppression of oxygen partition by reinforced self-assemblies with enhanced molecular density. The importance of molecular densification based on hydrophobic ion paring is also shown by the absence of UC emission from the **A2** assembly with larger size (104 nm, Φ_{OB} = 0%). Thus, the observed oxygen-barrier ability is not simply correlated with the aggregate size, but rather with the molecular organization of the unit ion-paired structure.

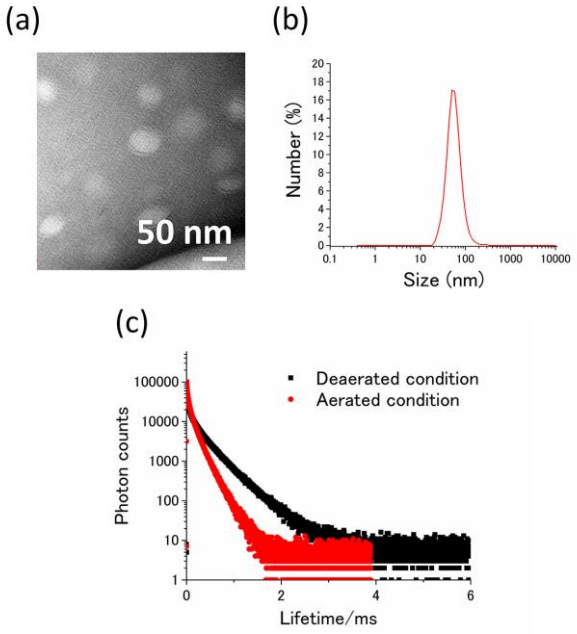

Figure 3-15. (a) TEM image of **A2**–OL dispersed in water. The sample was poststained with 2 wt% aqueous uranyl acetate. (b) DLS profile of aqueous **A2**–OL dispersion. ([**A2**] = 1 mM, [OL]=8 mM). (c) UC emission decay at 440 nm of **A2**–PtOEP–OL in water under 531 nm pulsed incident light excitation ([**A2**] = 1 mM, [PtOEP] = 1 μM, [OL] = 8 mM; black: deaerated and red: aerated conditions).

3.3.9 Consideration of oxygen-barrier mechanism

The permeation of small molecules across hydrophobic molecular assemblies, as typified by lipid bilayer membranes, has been traditionally explained by the solubility-diffusion model, in which permeability is correlated with the oil/water partition coefficient.[59,60] This works well for modeling permeation of small molecules in thick membranes.[61] Recent computational investigations show that the rate-determining steps for oxygen permeation across lipid bilayer membranes arise from the barrier associated with low local oxygen solubility and low oxygen diffusion rates. Fiber-cell plasma membranes show moderate barriers to oxygen transport, which have been explained by close packing of rigid cholesterol molecules and phospholipid tails, which generates a physical barrier to oxygen permeation at the interface.[27] These theoretical and experimental investigations on oxygen permeation in biomembranes are consistent with the present results; the enhanced intermolecular interactions and density at the aggregate surface of co-assembly **A2**–PtOEP–OL provides a rigid barrier that reduces oxygen partition and diffusion. In contrast to the case of ternary **A2**–PtOEP–OL, the less-developed binary aqueous molecular assembly **A2**–PtOEP showed quenching of excited triplets by dissolved oxygen, which is possibly facilitated by the presence of aqueous diffusion paths near to the chromophores. Thus, the control of intermolecular interactions and interfacial molecular density in acceptor self-assemblies are the key to enhancing their tolerance to molecular oxygen.

3.4 Conclusion

A supramolecular-crowding approach to achieve air-stable TTA-UC in aqueous media has been demonstrated on the basis of hydrophobic ion pairing of amphiphilic cationic acceptors and soft alkyl anions. The electrostatic repulsions between cationic groups surrounding the DPA chromophore are effectively shielded by the introduced hydrophobic counterions, and the consequent dense molecular organization exhibited a physical energy barrier to oxygen permeation and thus suppressed the quenching of triplet excited states by dissolved oxygen molecules. Both the hydrophobicity and flexibility of the counterions are important elements that control the stability of the dispersion and also provide solubilization sites for hydrophobic donor molecules. Thanks to the effective oxygen-shielding effect as well as the nearly 100% donor-to-acceptor TTET and high fluorescence quantum yield, the current self-assembled systems showed significantly high UC efficiency, comparable to that of the most efficient system in air-saturated water. Although the formation of hydrophobic ion pairs involving ionic dyes has been utilized to promote aggregation,[49,62-64] the engineering of the oxygen-shielding property of ion-paired amphiphilic chromophore self-assemblies was unprecedented. It would be worthwhile to generalize the current methodology for other wavelength conversions. The reinforcement of chromophoric self-assembly through hydrophobic ion pairing and the concept of supramolecular crowding developed in this work offer rational guidelines, not only for triplet-based technologies, but also for a wide range of chemistry that deals with oxygen-sensitive intermediates.

References

(1) Baluschev, S.; Miteva, T.; Yakutkin, V.; Nelles, G.; Yasuda, A.; Wegner, G. *Phys. Rev. Lett.* **2006,** *97*, 143903.

(2) Singh-Rachford, T. N.; Castellano, F. N. *Coord. Chem. Rev.* **2010,** *254*, 2560-2573.

(3) Zhao, J.; Ji, S.; Guo, H. *RSC Adv.* **2011,** *1*, 937-950.

(4) Kim, J.-H.; Kim, J.-H. *J. Am. Chem. Soc.* **2012,** *134*, 17478-17481.

(5) Monguzzi, A.; Tubino, R.; Hoseinkhani, S.; Campione, M.; Meinardi, F. *Phys. Chem. Chem. Phys.* **2012,** *14*, 4322-4332.

(6) Simon, Y. C.; Weder, C. *J. Mater. Chem.* **2012,** *22*, 20817-20830.

(7) Börjesson, K.; Dzebo, D.; Albinsson, B.; Moth-Poulsen, K. *J. Mater. Chem. A* **2013,** *1*, 8521-8524.

(8) Askes, S. H. C.; Bahreman, A.; Bonnet, S. *Angew. Chem. Int. Ed.* **2014,** *53*, 1029-1033.

(9) Häring, M.; Pérez-Ruiz, R.; von Wangelin, A. J.; Diaz, D. D. *Chem. Commun.* **2015,** *51*, 16848-16851.

(10) Schulze, T. F.; Schmidt, T. W. *Energy Environ. Sci.* **2015,** *8*, 103-125.

(11) Zhou, J.; Liu, Q.; Feng, W.; Sun, Y.; Li, F. *Chem. Rev.* **2015,** *115*, 395-465.

(12) Andernach, R.; Utzat, H.; Dimitrov, S. D.; McCulloch, I.; Heeney, M.; Durrant, J. R.; Bronstein, H. *J. Am. Chem. Soc.* **2015,** *137*, 10383-10390.

(13) Yanai, N.; Kimizuka, N. *Chem. Commun.* **2016,** *52*, 5354-5370.

(14) Fan, C.; Wu, W.; Chruma, J. J.; Zhao, J.; Yang, C. *J. Am. Chem. Soc.* **2016,** *138*, 15405-15412.

(15) Hill, S. P.; Hanson, K. *J. Am. Chem. Soc.* **2017,** *139*, 10988-10991.

(16) Huang, Z.; Tang, M. L. *J. Am. Chem. Soc.* **2017,** *139*, 9412-9418.

(17) Yang, D.; Duan, P.; Liu, M. *Angew. Chem. Int. Ed.* **2018,** *57*, 9357-9361.

(18) Xu, W.; Liang, W.; Wu, W.; Fan, C.; Rao, M.; Su, D.; Zhong, Z.et al. *Chem. - Eur. J.* **2018,** *24*, 16677-16685.

(19) Yang, X.; Han, J.; Wang, Y.; Duan, P. *Chem. Sci.* **2019,** *10*, 172-178.

(20) Smith, M. B.; Michl, J. *Chem. Rev.* **2010,** *110*, 6891-6936.

(21) Yost, S. R.; Lee, J.; Wilson, M. W. B.; Wu, T.; McMahon, D. P.; Parkhurst, R. R.; Thompson, N. J.et al. *Nat. Chem.* **2014,** *6*, 492-497.

(22) Busby, E.; Xia, J.; Wu, Q.; Low, J. Z.; Song, R.; Miller, J. R.; Zhu, X.-Y.et al. *Nat. Mater.* **2015,** *14*, 426-433.

(23) Chen, S.; Deng, L.; Xie, J.; Peng, L.; Xie, L.; Fan, Q.; Huang, W. *Adv. Mater.* **2010,** *22*, 5227-5239.

(24) Uoyama, H.; Goushi, K.; Shizu, K.; Nomura, H.; Adachi, C. *Nature* **2012,** *492*, 234-238.

(25) Quaranta, M.; Murkovic, M.; Klimant, I. *Analyst* **2013,** *138*, 6243-6245.

(26) Subczynski, W. K.; Swartz, H. M. In *Biomedical EPR - Part A: Free Radicals, Metals, Medicine, and Physiology*; 1st ed.; Eaton, S. R.;Eaton, G. R.;Berlier, L. J., Eds.; Springer US, 2005; Vol. 23.

(27) Dotson, R. J.; Smith, C. R.; Bueche, K.; Angles, G.; Pias, S. C. *Biophys. J.* **2017,** *112*, 2336-2347.

(28) Plesnar, E.; Szczelina, R.; Subczynski, W. K.; Pasenkiewicz-Gierula, M. *Biochim. Biophys. Acta* **2018,** *1860*, 434-441.

(29) Widomska, J.; Raguz, M.; Subczynski, W. K. *Biochim. Biophys. Acta* **2007,** *1768*, 2635-2645.

(30) Monguzzi, A.; Frigoli, M.; Larpent, C.; Tubino, R.; Meinardi, F. *Adv. Funct. Mater.* **2012,** *22*, 139-143.

(31) Liu, Q.; Yin, B.; Yang, T.; Yang, Y.; Shen, Z.; Yao, P.; Li, F. *J. Am. Chem. Soc.* **2013,** *135*, 5029-5037.

(32) Kim, J.-H.; Deng, F.; Castellano, F. N.; Kim, J.-H. *ACS Photonics* **2014,** *1*, 382-388.

(33) Askes, S. H. C.; Mora, N. L.; Harkes, R.; Koning, R. I.; Koster, B.; Schmidt, T.; Kros, A.et al. *Chem. Commun.* **2015,** *51*, 9137-9140.

(34) Kim, J.-H.; Kim, J.-H. *ACS Photonics* **2015,** *2*, 633-638.

(35) Kouno, H.; Ogawa, T.; Amemori, S.; Mahato, P.; Yanai, N.; Kimizuka, N. *Chem. Sci.* **2016,** *7*, 5224-5229.

(36) Thévenaz, D. C.; Monguzzi, A.; Vanhecke, D.; Vadrucci, R.; Meinardi, F.; Simon, Y. C.; Weder, C. *Mater. Horiz.* **2016,** *3*, 602-607.

(37) Kim, H.-i.; Kwon, O. S.; Kim, S.; Choi, W.; Kim, J.-H. *Energy Environ. Sci.* **2016,** *9*, 1063-1073.

(38) El Roz, K. A.; Castellano, F. N. *Chem. Commun.* **2017,** *53*, 11705-11708.

(39) Ramamurthy, V.; Caspar, J. V.; Eaton, D. F.; Kuo, E. W.; Corbin, D. R. *J. Am. Chem. Soc.* **1992,** *114*, 3882-3892.

(40) Nishiyabu, R.; Aime, C.; Gondo, R.; Noguchi, T.; Kimizuka, N. *Angew. Chem. Int. Ed.* **2009,** *48*, 9465-9468.

(41) Jayaraj, N.; Maddipatla, M. V. S. N.; Prabhakar, R.; Steffen Jockusch; N. J. Turro; Ramamurthy, V. *J. Phys. Chem. B* **2010,** *114*, 14320–14328.

(42) Easley, C. J.; Mettry, M.; Moses, E. M.; Hooley, R. J.; Bardeen, C. J. *J. Phys. Chem. A* **2018,** *122*, 6578-6584.

(43) Kimizuka, N.; Yanai, N.; Morikawa, M. *Langmuir* **2016,** *32*, 12304-12322.

(44) Joarder, B.; Yanai, N.; Kimizuka, N. *J. Phys. Chem. Lett.* **2018,** *9*, 4613-4624.

(45) Okahata, Y.; Kunitake, T. *J. Am. Chem. Soc.* **1979,** *101*, 5231-5234.

(46) Fuhrhop, J.-H.; Fritsch, D. *Acc. Chem. Res.* **1986,** *19*, 130-137.

(47) Kunitake, T. *Angew. Chem. Int. Ed.* **1992,** *31*, 709-726.

(48) Shikata, T.; Hirata, H. *Langmuir* **1988,** *4*, 345.

(49) Nakashima, T.; Kimizuka, N. *Adv. Mater.* **2002,** *14*, 1113-1116.

(50) Gusain, R.; Khatri, O. P. *RSC Adv.* **2016,** *6*, 3462-3469.

(51) Harada, N.; Takuma, Y.; Uda, H. *J. Am. Chem. Soc.* **1978,** *100*, 4029-4036.

(52) Islangulov, R. R.; Kozlov, D. V.; Castellano, F. N. *Chem. Commun.* **2005**, 3776-3778.

(53) Islangulov, R. R.; Castellano, F. N. *Angew. Chem. Int. Ed.* **2006,** *45*, 5957-5959.

(54) Hildebrand, A.; Garidel, P.; Neubert, R.; Blume, A. *Langmuir* **2004,** *20*, 320-328.

(55) Monguzzi, A.; Bianchi, F.; Bianchi, A.; Mauri, M.; Simonutti, R.; Ruffo, R.; Tubino, R.et al. *Adv. Energy Mater.* **2013,** *3*, 680-686.

(56) Pope, M.; Swenberg, C. E. In *Electric Processes In Organic Crystals and Polymers*; 2nd ed.; Oxford University Press: New Yrok, 1999.

(57) Fujiwara, Y.; Ozawa, R.; Onuma, D.; Suzuki, K.; Yoza, K.; Kobayashi, K. *J. Org. Chem.* **2013,** *78*, 2206-2212.

(58) Mongin, C.; Golden, J. H.; Castellano, F. N. *ACS Appl. Mater. Interfaces* **2016,** *8*, 24038-24048.

(59) Overton, E. *Ueber die osmotischen Eigenschaften der Zelle in ihrer Bedeutung für die Toxikologie und Pharmakologie*; Vierteljahrssche Naturforch, Ges.: Zürich, 1899.

(60) Mathai, J. C.; Tristram-Nagle, S.; Nagle, J. F.; Zeidel, M. L. *J. Gen. Physiol.* **2008,** *131*, 69-76.

(61) Walter, A.; Gutknecht, J. *J. Membr. Biol.* **1986,** *90*, 207-217.

(62) Faul, C. F. J.; Antonietti, M. *Adv. Mater.* **2003,** *15*, 673-683.

(63) Morikawa, M.; Yoshihara, M.; Endo, T.; Kimizuka, N. *J. Am. Chem. Soc.* **2005,** *127*, 1358-1359.

(64) Shiraki, T.; Morikawa, M.; Kimizuka, N. *Angew. Chem. Int. Ed.* **2008,** *47*, 106-108.

Chapter 4 Nonpentacene Polarizing Agents with Improved Air Stability for Triplet Dynamic Nuclear Polarization at Room Temperature

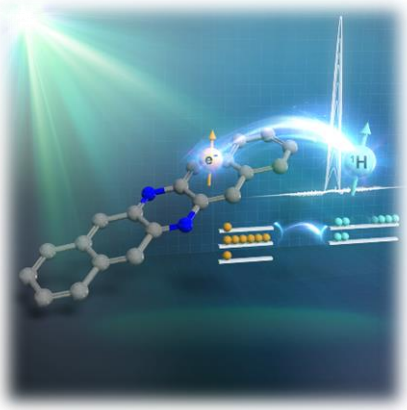

ABSTRACT: Triplet dynamic nuclear polarization (triplet-DNP), a method to enhance nuclear magnetic resonance (NMR) and magnetic resonance imaging (MRI) sensitivity using photo-excited triplet electrons, has great potential to hyperpolarize nuclear spins at room temperature. Since the first report of room-temperature triplet-DNP in 1990, pentacene has been the only and best option of triplet polarizing agent. However, the poor air-stability of pentacene has severely limited the applicability of triplet-DNP. We report the first example of polarizing agents with significant air stability as well as high polarizing ability comparable to pentacene. The introduction of electron-withdrawing diaza-substitution to pentacene and tetracene reduces the lowest unoccupied molecular orbital level and endows much improved stability under the ambient conditions. Importantly, the diaza-substituted pentacene and tetracene offer similar, or even slightly better, ^{1}H NMR signal enhancement compared with pentacene in the prototypical triplet-DNP test using *p*-terphenyl crystals. This work removes one of the largest obstacles toward the application of triplet-DNP for the hyperpolarization of biological molecules.

4.1 Introduction

Nuclear magnetic resonance (NMR) and magnetic resonance imaging (MRI) are informative analytical methods for molecular structure and spatial morphology. The general problem of NMR and MRI is their low sensitivity. The NMR/MRI signal intensity is proportional to the nuclear spin polarization that is on the order of 10^{-5} or less at a common magnetic field of NMR/MRI. Thus, in clinical MRI, highly abundant ^{1}H nuclei of water are predominantly observed. To overcome this limitation, dynamic nuclear polarization (DNP) has attracted much attention.[1-5] In common DNP, the electron spin polarization of free radicals is transferred to the nuclear polarization. The thermal electron spin polarization is 660 times larger than that of ^{1}H spins; accordingly, the ^{1}H sensitivity is enhanced by DNP. Importantly, the spin polarization depends on the Boltzmann distribution, and the high polarization enhancement over 660 times is obtained at very low temperature around 1 K.[6,7] Whereas the development of DNP has opened up new possibilities represented by metabolic imaging, it remains a grand challenge to achieve a high polarization enhancement at room temperature toward an ultimate goal, in vivo polarization of biological substances. To achieve hyperpolarization at room temperature, nonequilibrated photo-excited triplet electrons have been employed as a polarization source instead of free radicals.[8-14] The typical scheme of DNP based on a photo-excited triplet (triplet-DNP) is summarized in Figure 4-1. A polarizing agent absorbs light, and the subsequent spin-selective intersystem crossing (ISC) produces the large electron spin polarization in the excited triplet state sublevels regardless of temperature.[15] This polarization is effectively transferred to nuclear spins by the integrated solid effect (ISE), followed by polarized spin diffusion to the bulk.[16,17]

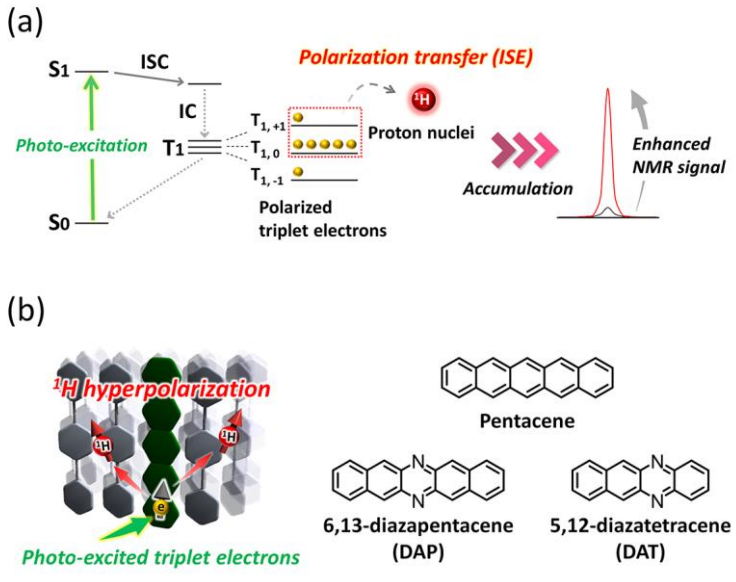

Figure 4-1. (a) Typical scheme of triplet-DNP. Photo-excitation of a polarizing agent is followed by spin-selective intersystem crossing (ISC). The resulting large electron spin polarization is transferred to the nuclear spin polarization through the integrated solid effect (ISE). (b) Schematic illustration of the triplet-DNP system and the chemical structure of triplet-DNP polarizing agents (pentacene, 6,13-diazpentacene (DAP), and 5,12-diazatetracene (DAT)).

Since the first report of room-temperature triplet-DNP by Wenckebach and coworkers in 1990,[8] pentacene has been the first and only option of triplet polarizing agent in this research field. Pentacene has the ideal properties of the polarizing agent such as strong absorption of visible light, high electron spin polarization, and microsecond-scale polarization lifetime that is long enough for the polarization transfer through ISE.[15] Whereas the triplet electron spin polarization was observed in other dyes such as aromatic hydrocarbons, porphyrins, and amino acids,[18-22] no compounds were found to compete with pentacene in terms of nuclear polarization enhancement at room temperature.

However, despite its potential, the application of triplet-DNP has been limited to bulk solids, largely due to the instability of pentacene under the ambient condition. Pentacene easily degrades within minutes by oxidation in the presence of light and air.[23,24] To expand the applicability of triplet-DNP to biological and medical fields, it is crucial to develop polarizing agents not only with high polarization but also with good air stability.

Here we report air-stable polarizing agents with high polarization ability comparable to pentacene for the first time. We employ diaza-substituted pentacene and tetracene, 6,13-diazapentacene (DAP),[25,26] and 5,12-diazatetracene (DAT)[27] (Figure 4-1). Recent theoretical studies predict that the introduction of nitrogen atoms to pentacene and tetracene would suppress the electron transfer from acene compounds to oxygen molecules by decreasing the lowest unoccupied molecular orbital (LUMO) energy levels.[28,29] We experimentally verified this prediction by observing remarkably improved stability of DAP and DAT compared with pentacene and tetracene in tetrahydrofuran (THF) under the ambient condition. Furthermore, polarization transfers from triplet electrons of DAP and DAT to ^{1}H nuclei in *p*-terphenyl successfully occurred. The resulting ^{1}H spin polarization enhancements of 970 and 840 times with DAP and DAT, respectively, are slightly higher than and comparable to that with pentacene (930 times). This work would open a wide range of new possibilities of triplet-DNP by solving the long awaited issue, the concomitant achievement of air stability and high polarization enhancement.

4.2 Experimental section

4.2.1 General methods

Characterization

^{1}H-NMR (400 MHz) spectra were measured on a JEOL JNM-ECZ400 spectrometer using TMS as the internal standard (for liquid samples). Elemental analysis was carried out by using a Yanaco CHN Corder MT-5 at the Elemental Analysis Center, Kyushu University. UV-Vis absorption spectra were recorded on JASCO V-670 and 770 spectrophotometers. Transmission and diffuse reflection methods were employed for solution and solid samples, respectively. Powder X-ray diffraction (PXRD) patterns were measured on a Bruker D2 Phaser (Cu-Kα, 30 kV, 10 mA). For fluorescence spectra measurement, a diode laser (532 nm, 200 mW, RGB Photonics) was used as an excitation source. The laser power was controlled by combining a software (Ltune) and a variable neutral density filter and measured using a PD300-UV photo-diode sensor (OPHIR Photonics). The laser beam was focused on a sample using a lens. The diameter of the laser beam ($1/e^2$) was measured at the sample position using a CCD beam profiler SP620 (OPHIR Photonics). The emitted light was collimated by an achromatic lens, the excitation light was removed using a notch filter (532 nm), and the emitted light was again focused by an achromatic lens to an optical fiber connected to a multichannel detector MCPD-9800 which was supplied and calibrated by Otsuka Electronics and equipped with a CCD sensor for the detection of whole visible range with high sensitivity. Transient absorption measurements were conducted by using a UNISOKU TSP-2000 system.

Triplet-DNP setup

Time-resolved ESR and triplet-DNP experiments were performed on home-built spectrometers explained below. The powder samples were packed in glass capillaries (FPT-220, FUJISTON, diameter 2.2 mm, inner diameter 1.4 mm) in air.

Triplet-DNP measurements were carried out using a home-build ~18 GHz cylindrical resonator with a window for laser irradiation and a coil for magnetic field sweep at a magnetic field generated by an electromagnet. A home-built laser (explained below) was used for pentacene, DAP, DAT excitation. After DNP, the polarized sample was shuttled into an NMR coil positioned above the resonator, which was tuned for ^{1}H spin. The timing control of the ISE sequence and the NMR detection were performed with an OPENCORE NMR spectrometer.

An electromagnet was purchased from Takano (MC160-60G-0.8T). The gap and pole size are 60 and 160 mm, respectively. A power supply PAG60-55 (Kikusui) with the stability of 10^{-4} was used. A microwave was generated from HMC-T2220 (Analog Devices) and amplified (PT188-1KW, Instruments For Industry) with the power of 1500 W. A transmission loss is -7dB. A triangle wave for field sweep was produced with a function generator (WF1945, NF Corporation) and amplified with OPamp (PA05, Apex Microtechnology).

Microwave resonator

A cylindrical resonator was designed by using an electromagnetic simulator (CST Studio). An enclosure is a copper, and four copper rods with a diameter of 1 mm are inserted for field sweep. A diameter and height are 21 and 30 mm, respectively. The materials are put on Teflon holders. A microwave is coupled with a rectangular waveguide (WR-51) through an iris with a diameter of 6 mm which is filled with Teflon. A laser is irradiated from the opposite side. Coils for ^{1}H detection were put outside/inside the resonator. In this experiment, we used outer one because of better sensitivity.

532 nm laser system

An ISC yield of pentacene is not high (< 30%). To increase the yield effectively, the pulse width of excitation light should be set much longer than fluorescence lifetime (~9 ns at room temperature) of pentacene. The 532 nm laser system consists of a Nd-doped YAG lasers with wavelengths of 1064 nm and a LiB_3O_5 (LBO) crystal for second harmonic generation (SHG). The wavelength, pulse width, maximum repetition rate, and output power of the system are 532 nm, ~180 ns, 3 kHz, and 0.5 mJ/pulse, respectively.

We constructed oscillator based on a Nd-doped YAG crystal with a high-reflection flat mirror for 1064 nm, and an output coupler. A YAG rod is mounted in a chamber and pumped by laser diodes with a wavelength of 808 nm. A rotator is inserted between the chambers to minimize birefringence losses. A thin glass plate set at Brewster's angle in the oscillator is used to generate polarized light, and an aperture in the 1064-nm oscillator is used to select the TEM00 mode beam. An acoustic-optic Q-switch (A/O Q-sw) is employed to pulse the laser as the switch provides a high repetition frequency.
In order to generate the 532 nm light, the two infrared beams are summed in the LBO crystal. Before the beam transmitted to the crystal, the diameter and polarization of the infrared beam are precisely adjusted by telescopes and quarter-wavelength plates. The phase

matching for SHG is accomplished by controlling the crystal temperature. The optimal temperature for SFG was 147.5 °C for our crystal and the conversion efficiency was 13%. Finally, the residual infrared beams are separated by visible-coated mirrors.

4.2.2 Materials

All reagents were used as received unless otherwise noted. 2,3-Diaminonaphthalene, 2,3-dihydroxynaphthalene, and pentacene (99.999%, purified by sublimation) were purchased from TCI. Analytical grade dichloromethane, pyridine, cupper acetate monohydrate, o-phenylenediamine, potassium dichromate and *p*-terphenyl were purchased from Wako Pure Chemical and glacial acetic acid was purchased from KISHIDA. *p*-Terphenyl was purified by zone melting. 6,13-Diazapentacene and 5,12-diazatetracene were synthesized according to the reported methods.[26,27,30] For sample preparation, each triplet polarizing agent (pentacene, 6,13-diazapentacene and 5,12-diazatetracene) was dispersed in CH_2Cl_2 and the dispersion was cast on agate mortar. After evaporation of CH_2Cl_2, *p*-terphenyl purified by zone melting was added on the agate mortar. After grinding, the powder was inserted into an ampule and sealed under vacuum. The sealed ampule was heated in an oil bath with a mantle heater above 220 °C (melting point of *p*-terphenyl). The resulting liquid was rapidly cooled with liquid nitrogen. Obtained solids were taken out from ampule and ground in an agate mortar.

Scheme 4-1.

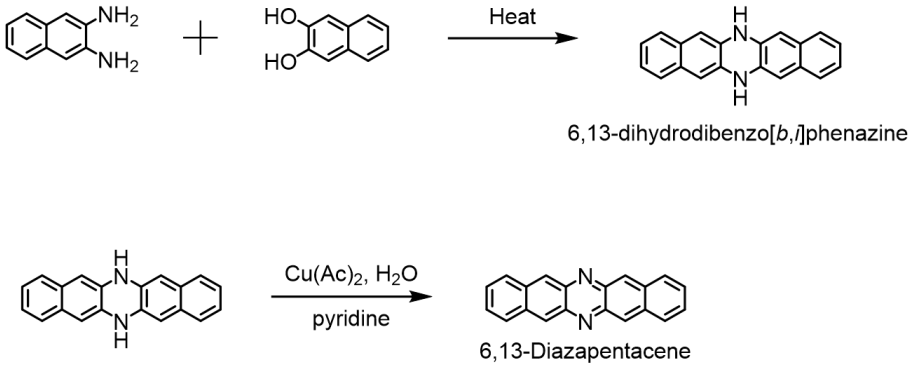

4.2.2-1 Synthesis of 6,13-dihydrodibenzo[b,i]phenazine

465 mg (2.94 mmol) of 2,3-diaminonaphthalene and 465 mg (2.90 mmol) of 2,3-dihydroxynaphthalene were placed in a 50 ml flask under N_2 after grinding. The solid mixture was heated for 1 hour at 180 °C, which is above the melting point of 2,3-dihydroxynaphthalene. After the reaction, the reacted liquid was cooled to room temperature and the crude product was made into a slurry with acetone. The slurry was filtered and washed with acetone and Et_2O several times. 6,13-dihydrodibenzo[b,i]phenazine was obtained as light green powder in a yield of 88.7%.

^{1}H-NMR (400 MHz, DMSO-d6): σ (ppm) = 6.48 (s, 4H), 6.97 (dd, 4H), 7.28 (dd, 4H), 8.85 (s, 2H).

4.2.2-2 Synthesis of dibenzo[b,i]phenazine (6,13-diazapentacene)

250 mg (0.89 mmol) of 6,13-dihydrodibenzo[b,i]phenazine was placed in a 10-20 ml microwave vial and 2 ml pyridine was added. 260 mg (1.43 mmol) of copper acetate monohydrate suspended in 18 ml pyridine was added to a microwave vial. The color of reaction mixture immediately turned to dark green. The resulting mixture was heated for 1 hour at 100 °C by microwave reactor (Biotage Initiator 2.5) under stirring. The suspension was cooled to room temperature, and added to 40 ml water. The resulting suspension was filtered and washed by acetone several times, and the dark green solid product was obtained in a yield of 85.5%.

^{1}H-NMR (400 MHz, DMF-d7, 60 °C): σ (ppm) = 7.59 (dd, 4H), 8.26 (dd, 4H), 9.04 (s, 4H).

Elemental analysis for C20H12N2: calculated (%) H 4.31, C 85.69, N 9.99; found (%) H 4.52, C 85.58, N 9.77.

Scheme 4-2.

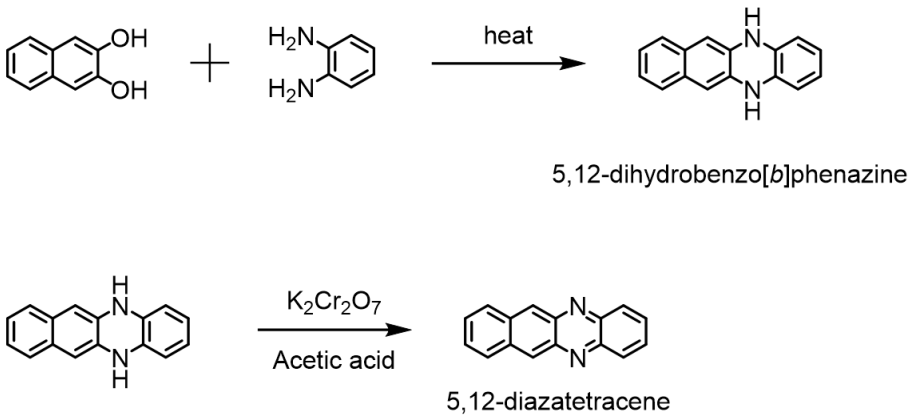

4.2.2-3 Synthesis of 5,12-dihydrodibenzo[b]phenazine

2.0 g (12.5 mmol) of 2,3-dihydroxynaphthalene and 1.35 g (12.5 mmol) of o-phenylenediamine were placed in a 50 ml flask under N_2 after grinding. The solid was heated for 1 hour at 180 °C that is above the melting point of 2,3-dihydroxynaphthalene. After the reaction, the reacted liquid was cooled to room temperature and the crude product was made into a slurry with acetone. The slurry was filtered and washed with acetone and methanol for several times. 5,12-dihydrodibenzo[b]phenazine was obtained as yellow powder in a yield of 86.2%.

^{1}H-NMR (400 MHz, DMSO-d6): σ (ppm) = 6.16 (dd, 2H), 6.25 (s, 2H), 6.34 (dd, 2H), 6.90 (dd, 2H), 7.15 (dd, 2H), 8.10 (s, 2H).

4.2.2-4 Synthesis of dibenzo[b,i]phenazine (5,12-diazatetracene)

900 mg (3.87 mmol) of 5,12-dihydrodibenzo[b]phenazine was placed in a 100 ml flask and dispersed in 27 ml of glacial acetic acid. 2N aqueous solution of potassium dichromate was added to the dispersion and stirred overnight at room temperature. The resulting solution was extracted with water and $CHCl_3$. After drying the organic phase over Na_2SO_4 and removing the solvent, the product was recrystallized in ethanol. The dark red crystal was filtered and washed with ethanol several times in ayield of 85.1%.

^{1}H-NMR (400 MHz, $CDCl_3$): σ (ppm) = 7.54 (dd, 2H), 7.82 (dd, 2H), 8.15 (dd, 2H), 8.24 (dd, 2H), 8.93 (s, 2H).

Elemental analysis for C16H10N2: calculated (%) H 4.38, C 83.46, N 12.17; found (%) H 4.35, C 83.35, N 12.21.

4.3 Results and discussion

4.3.1 Stability of diaza-substituted acenes

The new polarizing agents DAP and DAT were synthesized and characterized by ^{1}H NMR and elemental analysis (Scheme 4-1 and 2). Highest occupied molecular orbital (HOMO) and LUMO energy levels of pentacene, tetracene, and the diaza-substituted compounds DAP and DAT were calculated with density functional theory (DFT) using the B3LYP hybrid functional with the 6-31G* basis set (Figure 4-2). The estimated energy levels agree well with previous reports.[28,31] Reflecting the introduction of electron-withdrawing nitrogen atoms, both the HOMO and LUMO energy levels of DAP and DAT decreased compared with pentacene and tetracene, respectively. The lower LUMO energy levels of DAP and DAT suggest their higher stability under ambient conditions by suppressing the photo-oxidation through electron transfer from the photo-excited aromatic compounds to oxygen molecules.

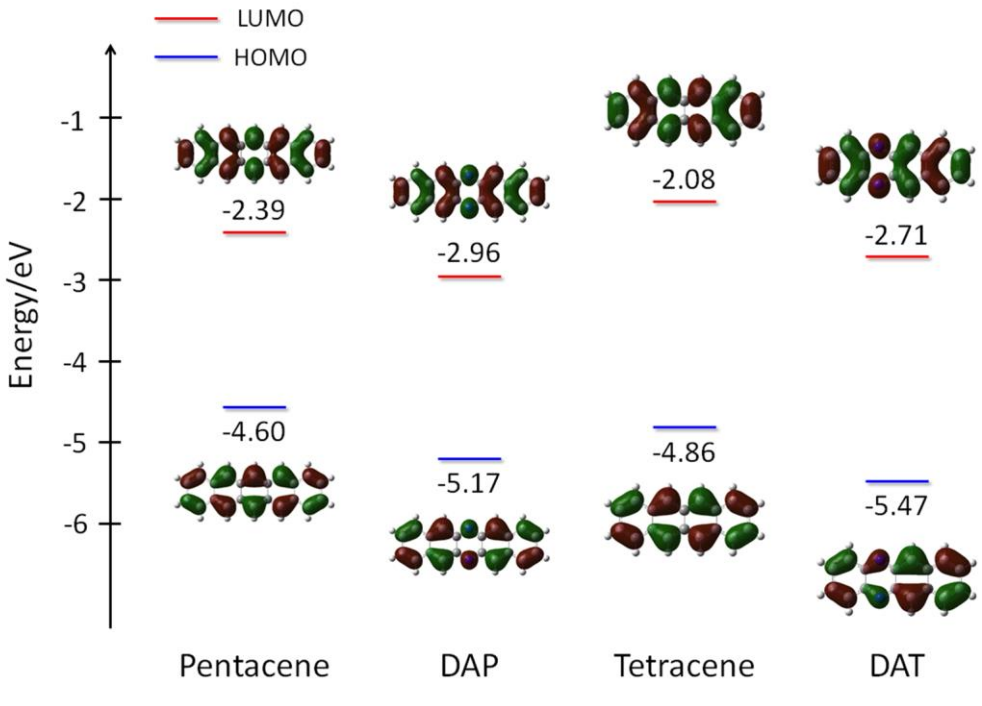

Figure 4-2. HOMO and LUMO energy levels of pentacene, DAP, tetracene, and DAT at the B3LYP/6-31G(d) level.

To experimentally assess the stability of the polarizing agents, a THF suspension of pentacene, DAP, a THF solution of tetracene, and DAT were exposed to the ambient light and air, and their UV−vis absorption spectra were measured at different times to monitor the degradation process (Figure 4-3).[24] Because of the poor solubility, saturated THF suspensions were employed for pentacene and DAP. The absorption intensities of the longest wavelength peaks were plotted as a function of time under the ambient condition (Figure 4-4). Obviously, the introduction of diaza-substitution significantly suppressed the decomposition of DAP and DAT compared with pentacene and tetracene, respectively. To quantify the stability, the half lives of each plot were employed. In the case of pentacene, the peak intensity was instantly decreased, and the half life was < 5 min. In contrast, the half life of DAP was much longer than the examined duration of 1500 min. Similarly, DAT showed a much longer half life of 750 min than that of tetracene (60 min). Agreeing with the DFT calculation results, the diaza-substitution significantly enhanced the stability of acenes under the air-saturated and ambient light conditions.

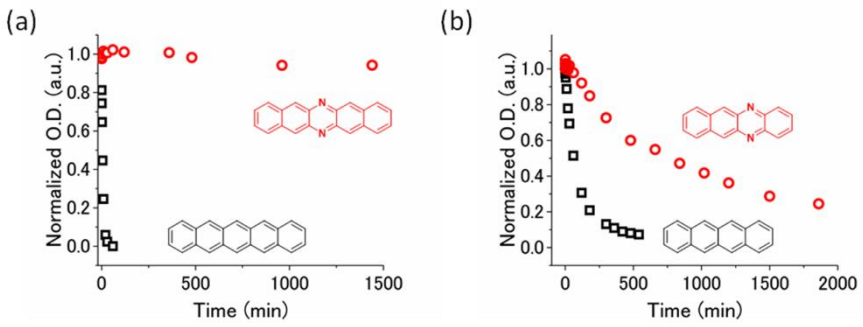

Figure 4-3. (a) Time dependence of optical density (O.D.) at the absorption peak positions of pentacene (575 nm) and DAP (640 nm) in THF under the air-saturated and ambient light conditions. (b) Time dependence of O.D. at the absorption peak positions of tetracene (473.5 nm) and DAT (500 nm) in THF under the air-saturated and ambient light conditions.

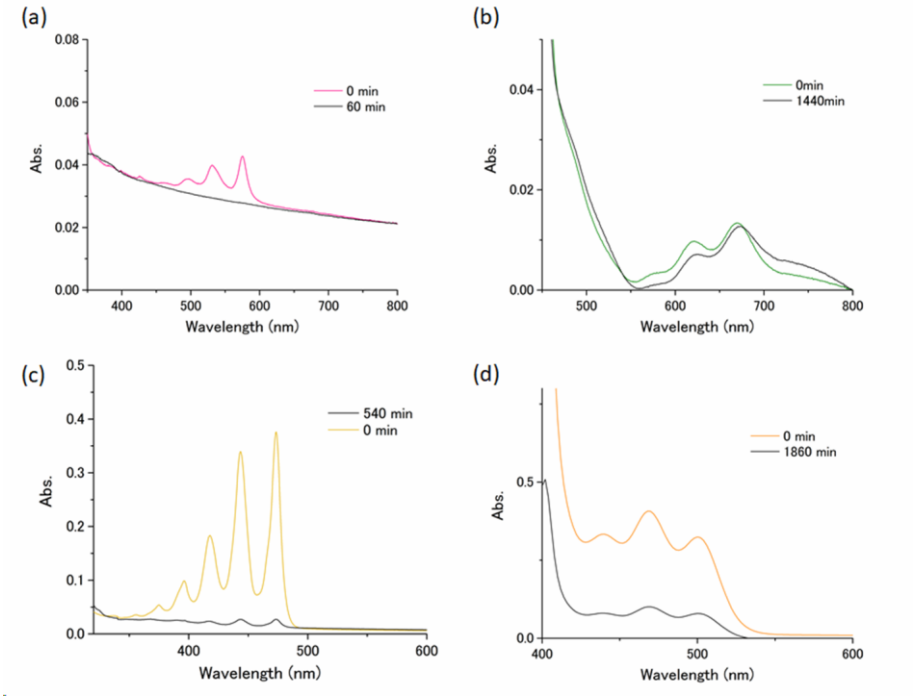

Figure 4-4. Absorption spectra of (a) pentacene, (b) DAP, (c) tetracene and (d) DAT in THF obtained right after the preparation and after placing the samples in the ambient light and temperature for certain times that are written in each graph. Due to the poor solubility of pentacene and DAP in THF (and any organic solvents), 1 mM dispersions were prepared and filtered with a pore size of 20 μm to get saturated dispersions. Tetracene and DAT were dissolved in THF (1 mM).

4.3.2 Sample preparation for triplet-DNP

The potential of DAP and DAT as polarizing agents was tested by the prototypical setup of triplet-DNP, which was doped in host crystalline powders of *p*-terphenyl. The aggregation of triplet polarizing agents induces the spin relaxation of triplet excitons.[32] It has been reported that pentacene molecules can be molecularly dispersed in *p*-terphenyl crystals by replacing one *p*-terphenyl molecule with one pentacene molecule.[33] 0.05 mol % of each polarizing agents was doped in *p*-terphenyl crystalline powders. Powder X-ray diffraction (PXRD) measurements were carried out for *p*-terphenyl crystalline powders including 0.05 mol % triplet polarizing agents (Figure 4-5). The basic crystal structure of *p*-terphenyl was well maintained, and only slight broadening was observed by the doping of DAP and DAT.

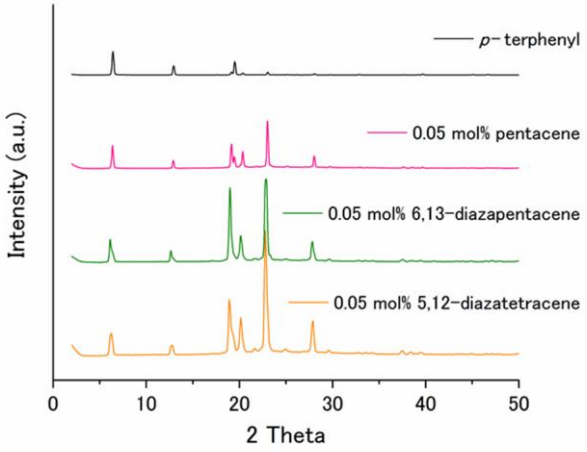

Figure 4-5. PXRD patterns of *p*-terphenyl crystals (black), *p*-terphenyl crystals doped with 0.05mol% pentacene (pink), DAP (green), and DAT (orange).

The good dispersibility of DAP and DAT in *p*-terphenyl crystals was confirmed by absorption spectra (Figure 4-6). The absorption peaks of DAP and DAT in *p*-terphenyl crystals were clearly blue-shifted and sharpened compared with those of bulk DAP and DAT solids, indicating the molecularly dispersed condition of the chromophores in *p*-terphenyl crystals. Tetracene molecules can be also molecularly dispersed in *p*-terphenyl crystals,[34] however, our experimental setup (532 nm excitation) is not suitable for tetracene excitation. Hereafter, pentacene, DAP, and DAT were employed as triplet polarizing agents.

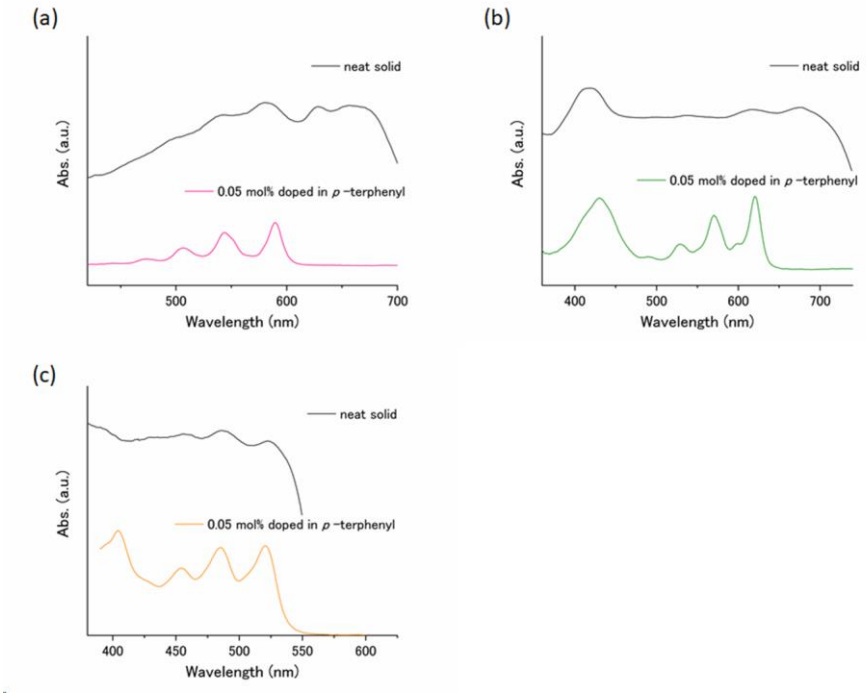

Figure 4-6. UV-vis absorption spectra of (a) pentacene, (b) DAP and (c) DAT in the neat solid and doped in *p*-terphenyl crystals at the molar ratio of 0.05 mol%.

4.3.3 Polarizing properties in photo-excited triplet states

The generation of electron spin polarization in the photo-excited triplet state was investigated by time-resolved electron spin resonance (ESR) measurements at room temperature. Under pulsed laser excitation at 532 nm, ESR spectra and the peak decay of each polarizing agent in *p*-terphenyl crystalline powders were measured (Figure 4-7). These spectra showed a characteristic line shape of the spin-polarized triplet state. The emission and absorption peaks in Figure 4-7a correspond to $T_{1,0} \rightarrow T_{1,-1}$ and $T_{1,0} \rightarrow T_{1,+1}$ transitions, respectively. These $\Delta m = 1$ transitions take place between the triplet sublevels in the nonequilibrium distribution that are caused by the spin-selective ISC. Decays of absorption peaks are shown in Figure 4-7b. The negative components derived from $T_{1,+1} \rightarrow S_0$ transitions support the spin-selective ISC process[35,36] and originate from a slower lifetime of $T_{1,+1} \rightarrow S_0$ transition than that of $T_{1,0} \rightarrow S_0$ transition. The decay lifetimes are summarized in Table 4-1. The ESR spectra were simulated by using the EasySpin toolbox in MATLAB (red lines in Figure 4-7a), and the obtained fitting parameters are shown in Table 4-2.[37] The spin polarization in triplet excited electrons was 49 and 66% for DAP and DAT. (Table 4-2) These values are close to that of pentacene (73%, Figure 4-7b, Table 4-2).[25] The diaza-substitution of pentacene and tetracene does not deteriorate the polarization of the triplet electrons, which is suitable for triplet-DNP.

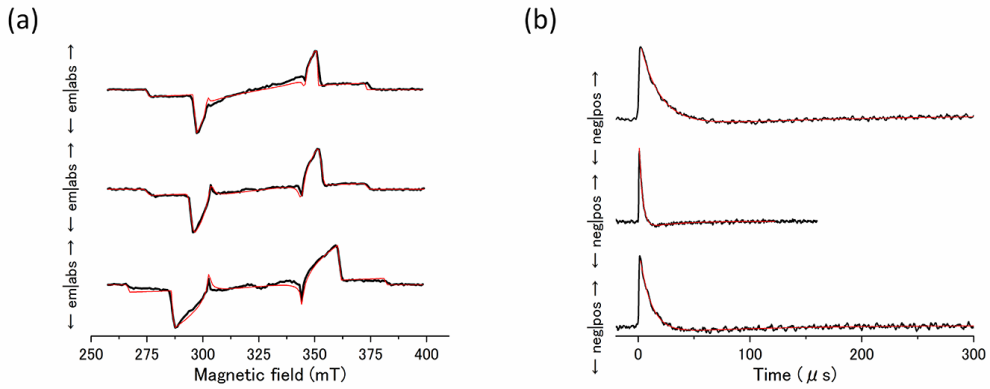

Figure 4-7. (a) Time-resolved ESR spectrum (black lines) of *p*-terphenyl crystalline powders doped with 0.05 mol % pentacene, DAP, and DAT at room temperature just after pulsed photoexcitation at 532 nm using a 9.15 GHz cylindrical resonator. The simulation results of ESR spectra by using the EasySpin toolbox in MATLAB are also shown (red lines). (b) Decays of the ESR peaks (black lines) under pulsed photoexcitation at 532 nm of *p*-terphenyl crystalline powders doped with 0.05 mol % pentacene at 349 mT, DAP at 352 mT, and DAT at 359 mT at room temperature. The fitting results are shown as red lines according to the following equation: $A \exp(-t/\tau_A) + B \exp(-t/\tau_B) + C$. Fitting parameters are shown in Tables 4-1 and 4-2.

Table 4-1. ESR decay time of *p*-terphenyl doped with 0.05mol% pentacene, DAP, and DAT obtained by fitting the data shown in Figure 4-7.

	A	τ_A (μs)	B	τ_B (μs)
pentacene	0.23	18	-0.033	140
6,13-diazapentacene	0.52	3.1	-0.038	26
5,12-diazatetracene	0.22	11	-0.023	98

Table 4-2. Zero-field splitting parameters and relative zero-field populations derived from simulation of the time-resolved ESR spectra of *p*-terphenyl doped with 0.05mol% pentacene, DAP, and DAT at room temperature shown in Figure 4-7. (D and E were assumed to be both positive)

	D (MHz)	E (MHz)	P_x	P_y	P_z
pentacene	1315	50	0.760	0.160	0.080
6,13-diazapentacene (DAP)	1355	81	0.600	0.175	0.235
5,12-diazatetracene (DAT)	1598	153	0.706	0.110	0.184

Calculation of the triplet polarization.

The triplet polarization $P_{triplet}$ is defined by the following equation,

$$P_{triplet} = \frac{p_x - \left(\frac{p_y + p_z}{2}\right)}{p_x + \left(\frac{p_y + p_z}{2}\right)}$$

where the p_x, p_y, p_z are the population along the canonical orientations of the zero-field splitting tensor and they are in the energy order $p_x > p_y > p_z$. Assuming the high field limit, the relationships $p_0 = p_x$ and $p_{\pm1} = (p_y + p_z)/2$ are established, where p_0, $p_{\pm1}$ are the population under the magnetic field.[38] The obtained fitting parameters are shown in Table 4-2. In powder samples, all orientations are present with the same probability and the resulting ESR spectrum is the sum of all contributions weighted over a sphere.[25]

4.3.4 ^{1}H hyperpolarization by triplet-DNP

The polarization transfer from photoexcited triplet electrons to ^{1}H nuclei by the ISE sequence was evaluated by ^{1}H NMR measurements. The triplet-DNP process was conducted at 0.676 T and ambient temperature. (See section 4.2.1) DAP and DAT molecules in *p*-terphenyl crystalline powders were photo-excited by a pulsed 532 nm laser, followed by the microwave irradiation and field sweep for polarization transfer. The field-sweep width of the magnetic field was ±30 mT at absorption peaks of ESR spectra (Figure 4-7a). After the triplet-DNP process was repeated to accumulate the spin polarization, ^{1}H NMR signals were measured to estimate the enhancement factor. The magnetic field and field-sweep time were optimized based on the ^{1}H NMR signal intensity for each sample (Figures 4-8). The optimum magnetic field of DAP and DAT for triplet-DNP was slightly shifted to a higher magnetic field compared with that of pentacene, which corresponds to the different ESR peak positions (Figure 4-7a). The optimized field-sweep times agree well with the ESR decays; ^{1}H NMR signal intensity saturates at a longer field-sweep time for a longer ESR lifetime (Figure 4-7b, Table 4-2).

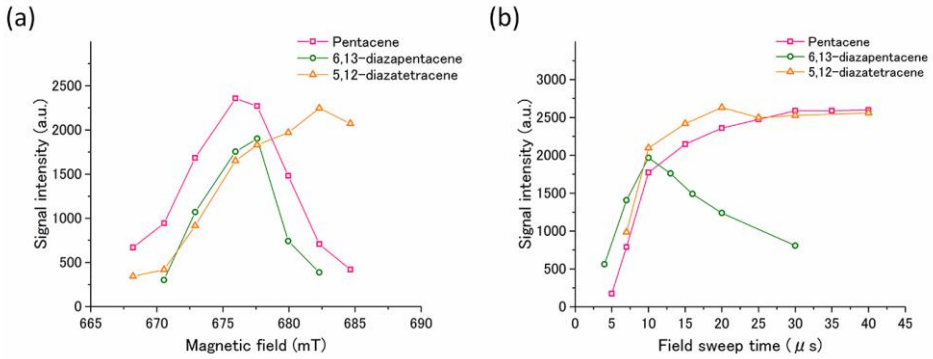

Figure 4-8. (a) Magnetic field dependence of ^{1}H NMR signal intensity of *p*-terphenyl doped with 0.05mol% pentacene (pink), DAP (green), and DAT (orange) after the triplet-DNP process. (b) Field sweep time dependence of ^{1}H NMR signal intensity of *p*-terphenyl doped with 0.05mol% pentacene (pink), DAP (green), and DAT (orange) after the triplet-DNP process.

The potential of DAP and DAT as polarizing agents was evaluated in *p*-terphenyl crystalline powders by measuring the ^{1}H NMR intensity after the triplet-DNP sequence under optimized conditions. Figure 4-9 and 4-10 shows buildup curves of ^{1}H spin polarization in each sample by changing the duration of the triplet-DNP process.

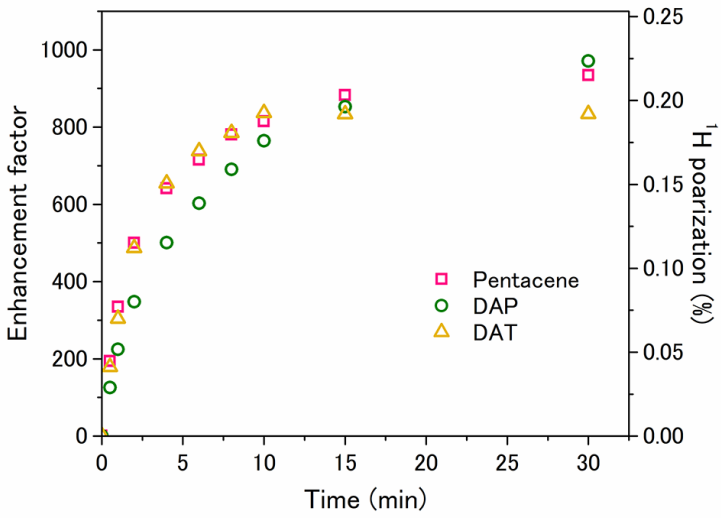

Figure 4-9. ^{1}H polarization buildup curves of *p*-terphenyl crystalline powders doped with 0.05 mol % of pentacene (pink, 0.676 T), DAP (green, 0.678 T), and DAT (yellow, 0.682 T) at room temperature using a 18.2 GHz cylindrical resonator. The sweep width of the magnetic field for polarization transfer was ±30 mT. The polarizations and enhancement factors were estimated by comparing the intensities of the hyperpolarized signals and the thermal signal of ethanol in 0.676 T at room temperature.

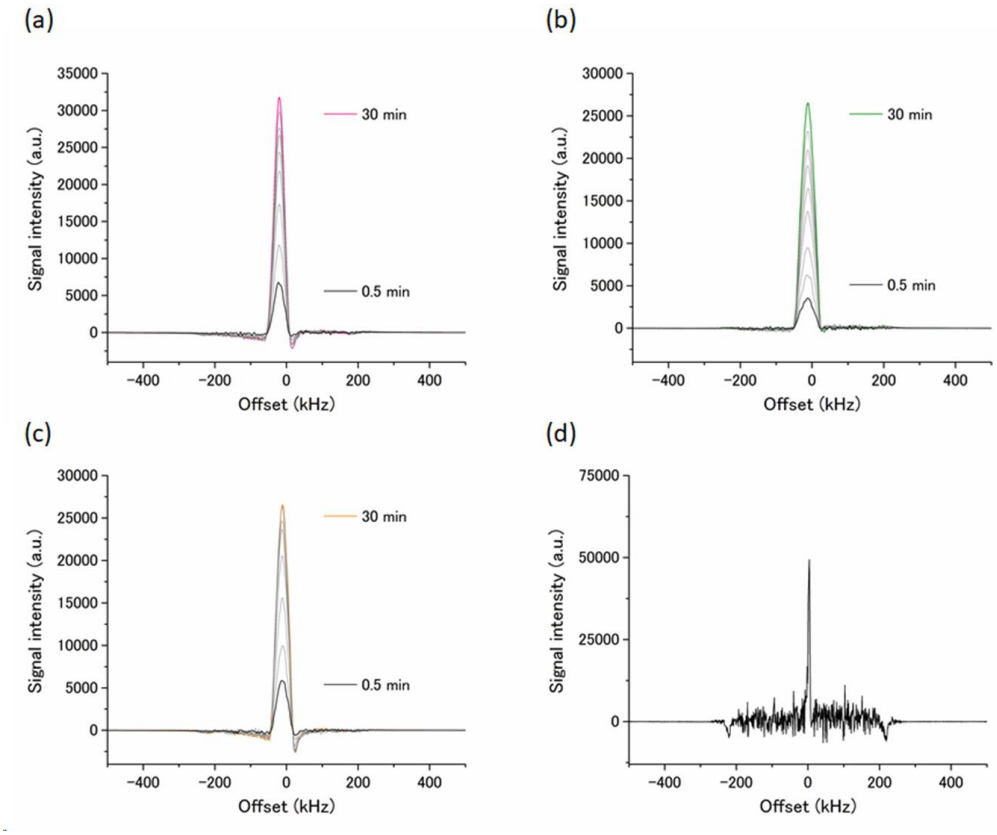

Figure 4-10. ^{1}H NMR spectra of *p*-terphenyl doped with 0.05mol% (a) pentacene (pink), (b) DAP (green), and (c) DAT (orange) after the triplet-DNP process for different durations and (d) ^{1}H NMR signal of ethanol with 10 times multiplication used as a reference.

For DAT, the final ^{1}H spin polarization was 0.19%, and the enhancement factor was 840, which are comparable to those of pentacene (0.21% and 930 times). Notably, DAP showed 0.22% ^{1}H spin polarization and 970 times enhancement, exceeding the performance of pentacene. This is probably related to the shorter triplet lifetime of DAP (3.3 μs) than that of pentacene (89 μs), as observed by transient absorption measurements (Figure 4-11). The existence of long-lived paramagnetic triplet electrons would induce the shortening of the spin–lattice relaxation time T_1 of ^{1}H spins.

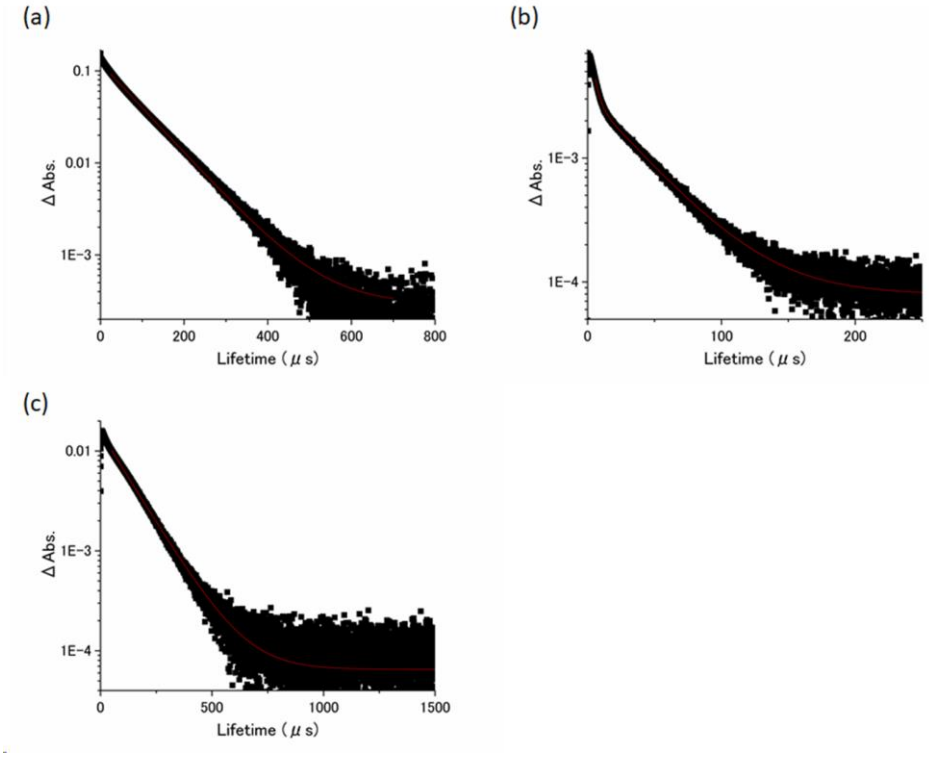

Figure 4-11. Triplet lifetime of *p*-terphenyl doped with 0.05mol% (a) pentacene (λ_{ex} = 590 nm and λ_{dt} = 520 nm), (b) DAP (λ_{ex} = 620 nm and λ_{dt} = 510 nm), and (c) DAT (λ_{ex} = 530 nm and λ_{dt} = 580 nm) measure by transient absorption. Triplet lifetimes obtained by fitting the decay curves are also shown.

4.4 Conclusion

In conclusion, we demonstrated the potential of diazasubstituted acenes as air-stable and high-performance triplet polarizing agents. Much higher stability of diaza-substituted DAP and DAT was observed compared with corresponding pentacene and tetracene under the ambient condition. Furthermore, comparable and superior enhancement of ^{1}H NMR signals was achieved with DAT and DAP compared with pentacene, respectively. The application of triplet-DNP has been limited to dense molecular crystals because air-sensitive pentacene molecules need to be well isolated from air. The air-stable polarizing agents developed here provide an important initial step toward the hyperpolarization of various target substances in water and even in vivo.

References

(1) Carver, T. R.; Slichter, C. P. *Phys. Rev.* **1953,** *92*, 212-213.

(2) Overhauser, A. W. *Phys. Rev.* **1953,** *92*, 411-415.

(3) Song, C.; Hu, K.-N.; Joo, C.-G.; Swager, T. M.; Griffin, R. G. *J. Am. Chem. Soc.* **2006,** *128*, 11385-11390

(4) Gallagher, F. A.; Kettunen, M. I.; Day, S. E.; Hu, D. E.; Ardenkjær-Larsen, J. H.; Zandt, R.; Jensen, P. R.et al. *Nature* **2008,** *453*, 940-943.

(5) Ji, X.; Bornet, A.; Vuichoud, B.; Milani, J.; Gajan, D.; Rossini, A. J.; Emsley, L.et al. *Nat. Commun.* **2017,** *8*, 13975.

(6) Ardenkjær-Larsen, J. H.; Fridlund, B.; Gram, A.; Hansson, G.; Hansson, L.; Lerche, M. H.; Servin, R.et al. *Proc. Natl. Acad. Sci. USA* **2003,** *100*, 10158–10163.

(7) Ardenkjær-Larsen, J. H. *J. Magn. Reson.* **2016,** *264*, 3-12.

(8) Henstra, A.; Lin, T.-S.; Schmidt, J.; Wenckebach, W. T. *Chem. Phys. Lett.* **1990,** *165*, 6-10.

(9) Iinuma, M.; Takahashi, Y.; Shaké, I.; Oda, M.; Masaike, A.; Yabuzaki, T.; Shimizu, H. M. *J. Magn. Reson.* **2005,** *175*, 235-241.

(10) Takeda, K. *Triplet State Dynamic Nuclear Polarization*; VDM Verlag Dr. Müeller: Saarbrücken, Germany, 2009.

(11) Tateishi, K.; Negoro, M.; Kagawa, A.; Kitagawa, M. *Angew. Chem. Int. Ed.* **2013,** *52*, 13307-13310.

(12) Tateishi, K.; Negoro, M.; Nishida, S.; Kagawa, A.; Morita, Y.; Kitagawa, M. *Proc. Natl. Acad. Sci. USA* **2014,** *111*, 7527-7530.

(13) Negoro, M.; Kagawa, A.; Tateishi, K.; Tanaka, Y.; Yuasa, T.; Takahashi, K.; Kitagawa, M. *J. Phys. Chem. A* **2018,** *122*, 4294-4297.

(14) Fujiwara, S.; Hosoyamada, M.; Tateishi, K.; Uesaka, T.; Ideta, K.; Kimizuka, N.; Yanai, N. *J. Am. Chem. Soc.* **2018,** *140*, 15606-15610.

(15) Sloop, D. J.; Yu, H. L.; Lin, T. S.; Weissman, S. I. *J. Chem. Phys.* **1981,** *75*, 3746-3757.

(16) Henstra, A.; Wenckebach, W. T. *Mol. Phys.* **2014,** *112*, 1761-1772.

(17) Can, T. V.; Weber, R. T.; Walish, J. J.; Swager, T. M.; Griffin, R. G. *Angew. Chem. Int. Ed.* **2017,** *56*, 6744-6748.

(18) Zuclich, J. *J. Chem. Phys.* **1970,** *52*, 3586-3591.

(19) Ozarowski, A.; Misra, A.; Ghosh, S.; Maki, A. H. *J. Phys. Chem. B* **2002,** *106*, 5099-5104.

(20) Akiyama, K.; Tero-Kubota, S.; Ikegami, Y. *Chem. Phys. Lett.* **1991,** *185*, 65-67.

(21) Deimling, M.; Brunner, H.; K. P. Dinse; Hausser, K. H.; Colpa, J. P. *J. Magn. Reson.* **1980,** *39*, 185-202.

(22) van Kesteren, H. W.; Wenckebach, W. T.; Schmidt, J. *Phys. Rev. Lett.* **1985,** *55*, 1642-1644.

(23) Yamada, M.; Ikemoto, I.; Kuroda, H. *Bull. Chem. Soc. Jpn.* **1988,** *61*, 1057-1062.

(24) Maliakal, A.; Raghavachari, K.; Katz, H.; Chandross, E.; Siegrist, T. *Chem. Mater.* **2004,** *16*, 4980-4986.

(25) Bogatko, S.; Haynes, P. D.; Sathian, J.; Wade, J.; Kim, J.-S.; Tan, K.-J.; Breeze, J.et al. *J. Phys. Chem. C* **2016,** *120*, 8251-8260.

(26) Miao, Q.; Nguyen, T.-Q.; Someya, T.; Blanchet, G. B.; Nuckolls, C. *J. Am. Chem. Soc.* **2003,** *125*, 10284-10287.

(27) Miao, S.; Brombosz, S. M.; Schleyer, P. v. R.; Wu, J. I.; Barlow, S.; Marder, S. R.; Hardcastle, K. I.et al. *J. Am. Chem. Soc.* **2008,** *130*, 7339-7344.

(28) Chen, Y.; Shen, L.; Li, X. *J. Phys. Chem. A* **2014,** *118*, 5700-5708.

(29) Kaur, I.; Jia, W.; Kopreski, R. P.; Selvarasah, S.; Dokmeci, M. R.; Pramanik, C.; McGruer, N. E.et al. *J. Am. Chem. Soc.* **2008,**

130, 16274-16286.

(30) Weng, S. Z.; Shukla, P.; Kuo, M. Y.; Chang, Y. C.; Sheu, H. S.; Chao, I.; Tao, Y. T. *ACS Appl. Mater. Interfaces* **2009,** *1*, 2071-2079.

(31) Wang, X.; Lau, K.-C. *J. Phys. Chem. C* **2012,** *116*, 22749−22758.

(32) Bizzaro, W.; Yarmus, L.; Rosenthal, J.; Berk, N. F. *Phys. Rev. B* **1981,** *23*, 5673-5675.

(33) Bordat, P.; Brown, R. *Chem. Phys. Lett.* **1998,** *291*, 153-160.

(34) Yu, H. L.; Lin, T. S.; Sloop, D. J. *J. Chem. Phys.* **1983,** *78*, 2184-2188.

(35) Terazima, M.; Yamauchi, S.; Hirota, N. *J. Chem. Phys.* **1986,** *84*, 3679-3687.

(36) Hirota, N.; Yamauchi, S. *J. Photochem. Photobiol. C* **2003,** *4*, 109-124.

(37) Stoll, S.; Schweiger, A. *J. Magn. Reson.* **2006,** *178*, 42-55.

(38) Hintze, C.; Steiner, U. E.; Drescher, M. *ChemPhysChem* **2017,** *18*, 6-16.

Chapter 5 Water-Soluble Polarizing Agents for Triplet Dynamic Nuclear Polarization of Crystalline Ice

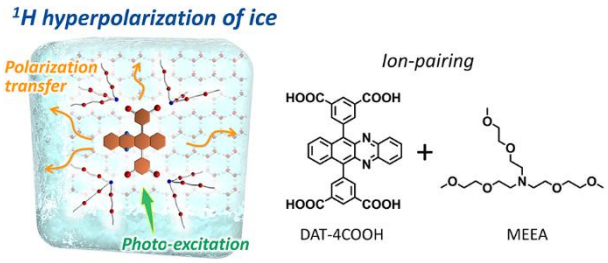

ABSTRACT: Triplet dynamic nuclear polarization (triplet-DNP) is a method to enhance nuclear spin polarization at moderate temperatures by employing photo-excited polarized triplet electrons. While the hyperpolarization of water is strongly desired for medical and biological applications, water-soluble triplet polarizing agents have not been reported so far. In addition, it is particularly important to develop polarizing agents dispersible in crystalline ice with long spin-lattice relaxation time (T_1) for triplet-DNP above liquid nitrogen temperature. Herein, the first example of triplet-DNP of crystalline ice is reported. A novel water-soluble triplet polarizing agent having carboxylic acid functionalities is developed, and it is successfully dispersed in pure crystalline ice through ion-pairing with a hydrophilic and bulky amine. The ^{1}H hyperpolarization of crystalline ice is confirmed by a long build-up time over tens of minutes at 140 K, demonstrating the critical initial step towards the hyperpolarization of biological molecules by triplet-DNP.

5.1 Introduction

Dynamic nuclear polarization (DNP) is a promising technique to overcome the sensitivity limitation of nuclear magnetic resonance (NMR) and magnetic resonance imaging (MRI).[1-8] Water works as a contrast agent in magnetic resonance angiography (MRA) for diagnosing various medical conditions such as emboli, stenosis, and aneurysms.[9,10] Furthermore, water is a ubiquitous polarization source for biological substances such as metabolites, peptides, and proteins. The hyperpolarization of water has been attained by using polarized electron spins of free radicals at around 1.5 K.[11-13] The mixture of water and glycerol/DMSO, so-called DNP juice, was hyperpolarized at the cryogenic temperature, and then the DNP juice was dissolved and injected into the NMR tube containing biomolecules. Through proton exchange, the water hyperpolarization was transferred to biomolecules such as amino acids, peptides, and proteins.[11-13] While significant polarization enhancements of biological substances have been achieved by using this dissolution-DNP method, the use of cryogenic temperatures around 1.5 K inevitably increases the cost of the instruments.[14]

To achieve hyperpolarization at much higher temperature, another DNP method using polarized electron spins of photo-excited triplet state (triplet-DNP) has attracted much attentions (Figure 5-1a).[15-24] In triplet-DNP, polarized triplet electrons are produced by spin-selective intersystem crossing (ISC) from photo-excited singlet state (S_1), which is followed by polarization transfer from triplet electron spins to nuclear spins through the integrated solid effect (ISE). Despite its potential, the applications of triplet-DNP have been limited to organic bulk crystals[15-20], nanocrystals,[21] metal-organic frameworks (MOFs),[22] or molecular glass.[23,24] The key to achieve a high water polarization at a higher temperature is to utilize the long spin-lattice relaxation time (T_1) of ^{1}H in crystalline ice over 5 minutes. However, there have been no reports on water-soluble polarizing agents. Therefore, to dissolve hydrophobic polarizing agents, it has been required to use the ethanol-d6 : water = 80 : 20 (w/w) mixture, whose T_1 was only ~10 s.[24] There is a clear need to develop water-soluble triplet polarizing agents for hyperpolarization of crystalline ice.

Here, we report the first example of a water-soluble triplet polarizing agent as well as the first demonstration of crystalline ice by triplet-DNP (Figure 5-1b). Conventionally, pentacene has been the only and best option for the triplet polarizing agent, but pentacene is immediately decomposed by oxidation at the ambient condition.[25,26] To solve this stability issue, our group has reported that 5,12-diazatetracene (DAT) shows the significant air stability as well as the high polarizing ability comparable to pentacene.[20] Based on this previous work, we design a novel water-soluble polarizing agent DAT-4COOH by modifying DAT with four carboxylic acid groups (Figure 5-1b). While a sodium salt DAT-

4COONa aggregated in ice, an ion-pair between DAT-4COOH and bulky hydrophilic tris[2-(2-methoxyethoxy)ethyl]amine (MEEA) is successfully dispersed in ice without aggregation. We also found that the number of carboxylic acid groups is important to be dispersed in ice since DAT with two carboxylic acid moieties could not be dispersed. The polarization transfer from DAT-4COOH/MEEA triplet to water ^{1}H is realized with a significantly long build-up time over tens of minutes, reflecting the long ^{1}H T_1 of crystalline ice.

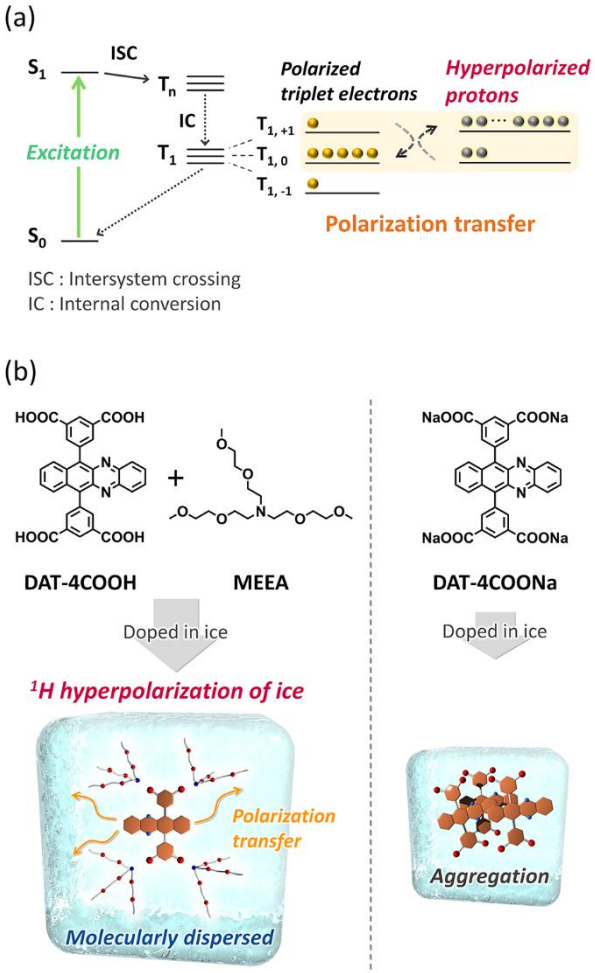

Figure 5-1. (a) Typical scheme of triplet-DNP. Photoexcitation of a polarizing agent is followed by spin-selective intersystem crossing (ISC). The resulting large electron spin polarization is transferred to the nuclear spin polarization through the integrated solid effect (ISE). (b) Schematic illustration of aggregation-free dispersion of the ion pair between DAT-4COOH and MEEA for triplet-DNP in crystalline ice for triplet-DNP. DAT-4COONa aggregates in crystalline ice.

5.2 Experimental section

5.2.1 General methods

Characterization

^{1}H-NMR (400 MHz) spectra were measured on a JEOL JNM-ECZ400 spectrometer using TMS as the internal standard (for liquid samples). Elemental analysis was carried out by using a Yanaco CHN Corder MT-5 at the Elemental Analysis Center, Kyushu University. Dynamic light scattering (DLS) measurements were carried out by using Malvern Nano-ZS ZEN3600. UV-Vis absorption spectra were recorded on JASCO V-670 and 770 spectrophotometers. Temperature-dependent photoluminescence and excitation spectra were recorded in a cryostat (Optistat DN2, Oxford Instruments) equipped with a controller (MercuryiTC, Oxford Instruments). The cryostat was mounted in the JASCO FP8500 spectrofluorometer. Low temperature quantum yield was measured in an integrating sphere using a Hamamatsu Photonics absolute quantum yield measurement system (C9920-02G) equipped with a holder for low-temperature measurement (A11238-01).

Triplet-DNP setup

Time-resolved ESR and triplet-DNP experiments were performed on home-built spectrometers explained in Chapter 4. The aqueous solution was added in glass capillaries (FPT-220, FUJISTON, diameter 2.2 mm, inner diameter 1.4 mm) in air and frozen in a liquid nitrogen.

5.2.2 Materials

Synthesis of DAT was reported[20] and all reagents were used as received unless otherwise noted. Bromine, sodium sulfite, cesium carbonate and sodium hydroxide, potassium hydroxide were purchased from Wako pure chemical, dimethyl 5-(4,4,5,5-Tetramethyl-1,3,2-dioxaborolan-2-yl)isophthalate, 4-(methoxycarbonyl)phenylboronic acid were purchased from TCI, and Tris[2-(2-methoxyethoxy)ethyl]amine and PEPPSI-IPr was purchased from Sigma Aldrich. Potassium carbonate and 1,4-dioxane were purchased from KISHIDA. Tris[2-(2-methoxyethoxy)ethyl]amine was purified by distillation.

Scheme 5-1

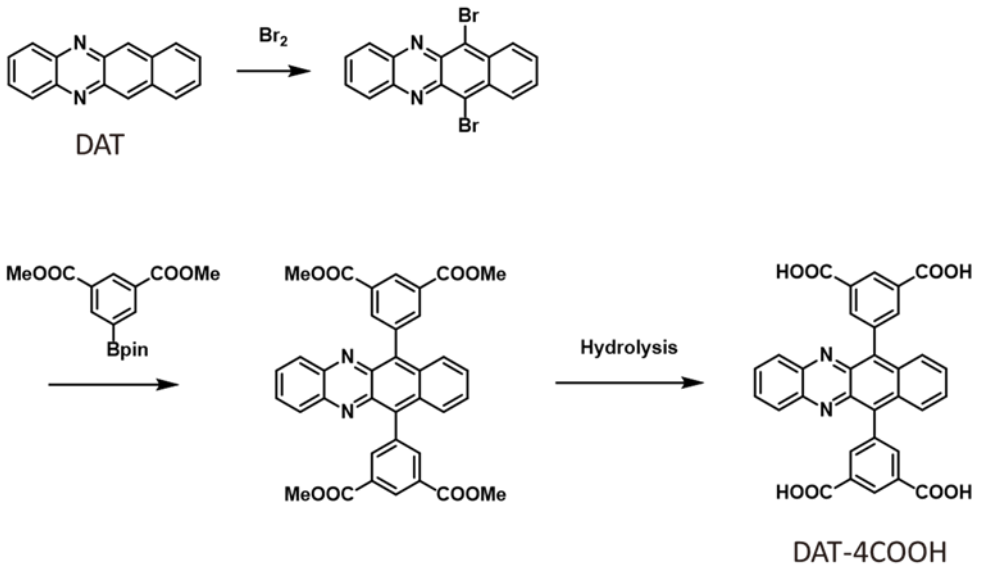

5.2.2-1 Synthesis of 6,11-dibromobenzo[b] phenazine

1.0 g (4.3 mmol) of DAT was placed in a 300 ml flask and dissolved in 175 ml of $CHCl_3$. After cooling in the ice bath, 0.5 ml of bromine was slowly added to the DAT solution. The resulting dark solution was kept stirred until room temperature and reaction was monitored by TLC. Then, the solution was washed with a Na_2SO_3 aqueous solution to quench the bromine. The organic layer was dried over anhydrous Na_2SO_4 and concentrated under reduced pressure after filtration. The crude product was purified by column chromatography with CH_2Cl_2 /hexane (1 : 3) and benzo[b]phenazine was obtained as dark purple solids (yield: 50%).
^{1}H-NMR (400 MHz, $CDCl_3$): σ (ppm) = 8.70-8.73 (m, 2H), 8.36-8.39 (m, 2H), 7.88-7.90 (m, 2H), 7.67-7.70 (m, 2H).

5.2.2-2 Synthesis of tetramethyl 5,5'-(benzo[b]phenazine-6,11-diyl)diisophthalate

A mixture of 50 mL of toluene, 10 mL of ethanol and 20 mL of H_2O was bubbled with N_2. 388 mg (1.0 mmol) of 6,11-dibromobenzo[b] phenazine, 1.25 g (4.0 mmol) of dimethyl 5-(4,4,5,5-Tetramethyl-1,3,2-dioxaborolan-2-yl)isophthalate, 13.6 mg (0.02 mmol) of PEPPSI-IPr, and 1.3 g (4.0 mmol) of $CsCO_3$ were dispersed in the above mixed solvents under an atmosphere of N_2. The mixture was refluxed for 8 hours. Thereafter, the mixture was extracted with CH_2Cl_2/brine, and dried over anhydrous Na_2SO_4, and concentrated under reduced pressure. The crude materials was purified through column chromatography with $CHCl_3$/methanol (100 : 1) as eluent. DAT-4COOMe was obtained as red solids including some impurity.

5.2.2-3 Synthesis of 5,5'-(benzo[b]phenazine-6,11-diyl)diisophthalic acid (DAT-4COOH)

To a suspension of 400 mg (0.65 mmol) of DAT-4COOMe in the mixture of 50 ml THF, 50 ml methanol and 25 ml 4N NaOH aqueous solution was added. The mixture was stirred overnight. The mixture formed by acidification with 4N aqueous HCl was collected by centrifugation and washed several times with methanol. The filtrate was recrystallized in THF and DAT-4COOH was obtained as red solids by filtration. (yield: 15%)
^{1}H-NMR (400 MHz, DMSO-d6): σ (ppm) = 13.4 (br, 4H), 8.72-8.73 (t, 2H), 8.35 (m, 4H), 7.98-8.01 (dd, 2H), 7.82-7.87 (m, 4H), 7.60-7.62 (dd, 2H).
Elemental analysis for C32H18N2O8: calculated (%) H 3.25, C 68.82, N 5.02; found (%) H 3.44, C 68.67, N 4.95.

5.3 Results and discussion

5.3.1 Dispersibility of polarizing agent in ice

The new polarizing agent DAT-4COOH was synthesized and characterized by ^{1}H NMR and elemental analysis (Scheme 5-1). Since the aggregation of triplet polarizing agents has been known to largely decrease the effect of triplet-DNP, we attempted to increase the solubility of DAT-4COOH by the complexation with MEEA that works as hydrophilic and bulky cations.[27] When the DAT-4COOH/MEEA mixed solution was frozen by being soaked in liquid nitrogen, the sample color and fluorescence were close to those of molecularly-dispersed DAT-4COOH/MEEA in frozen DMSO (Figure 5-2a).

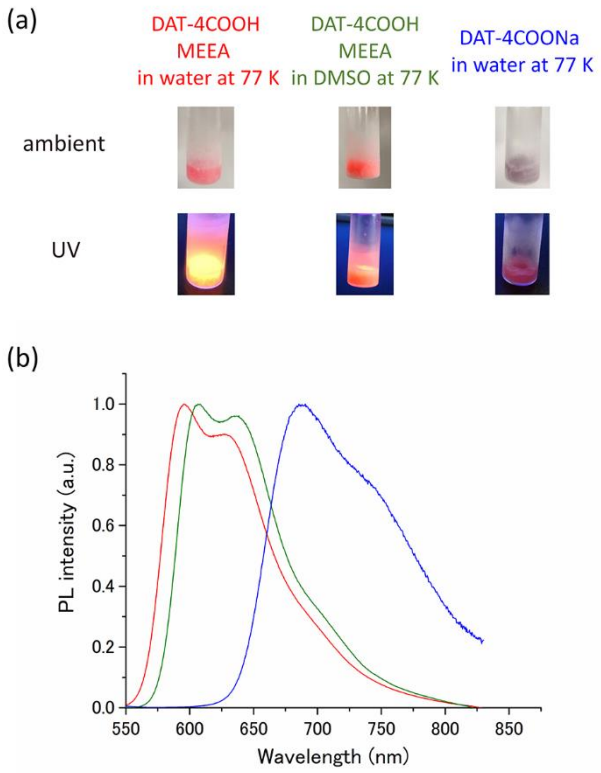

Figure 5-2. (a) Photographs of DAT-4COOH (1 mM)/MEEA (4mM) mixture in water at 77 K, DAT-4COOH (1 mM)/MEEA (4mM) mixture in DMSO at 77 K, and 1 mM DAT-4COONa in water at 77 K under ambient light and UV light. (b) Photoluminescence (PL) spectra (λ_{ex} = 532 nm) of DAT-4COOH (1 mM)/MEEA (4 mM) mixture in water at 140 K (red), DAT-4COOH (1 mM)/MEEA (4 mM) mixture in DMSO at 140 K (green), and 1 mM DAT-4COONa in water at 140 K (blue).

Indeed, excitation and fluorescence peaks of DAT-4COOH/MEEA in water at 140 K (557 nm and 596 nm, respectively) was close to those of DAT-4COOH/MEEA molecularly-dispersed in DMSO at the same temperature (560 nm and 609 nm, respectively) (Figure 5-2b, 5-3, 5-4, 5-5). On the other hand, an aqueous solution of DAT-4COONa, obtained by neutralization of DAT-4COOH with NaOH, showed a different color (dark purple) and very weak fluorescence (Figure 5-2a). Compared with DAT-4COOH/MEEA in ice, excitation and fluorescence peaks of DAT-4COONa in frozen ice showed a redshift to 590 nm and 690 nm, respectively (Figure 5-2b, 5-5). Significantly, the ion-pairing with MEEA improved the hydrophilicity of the polarizing agent to be able to be molecularly dispersed in ice.

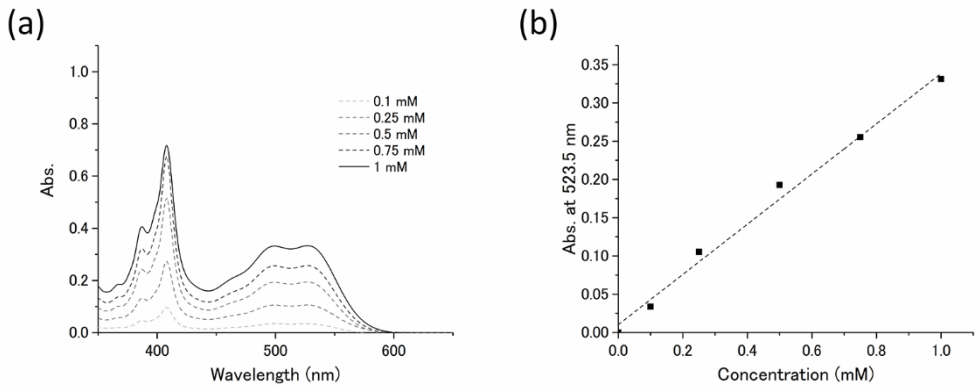

Figure 5-3. (a) Concentration-dependent absorption spectra of DAT-4COOH/MEEA (1:4) in DMSO at room temperature. (b) The absorbance of DAT-4COOH/MEEA (1:4) in DMSO at 523.5 nm with different DAT-4COOH concentrations. The fitting result is shown as a black line according to be following equation, y = Ax+B. The observed linearity supports the molecularly-dispersed state of DAT-4COOH/MEEA in DMSO at room temperature in the examined concentration range.

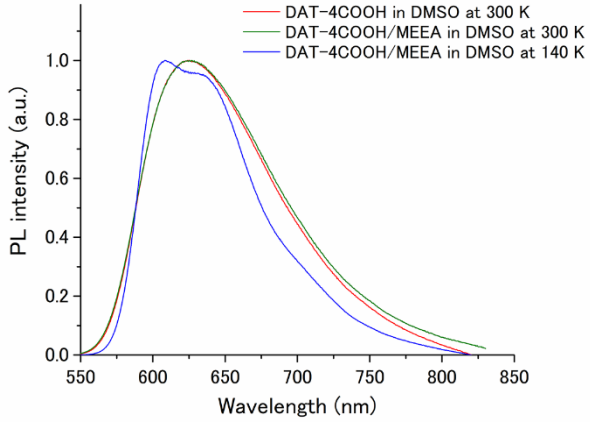

Figure 5-4. Photoluminescence (PL) spectra (λ_{ex} = 532 nm) of DAT-4COOH (1 mM) in DMSO at 300 K (red), DAT-4COOH (1 mM)/MEEA (4mM) mixture in DMSO at 300 K (green) and DAT-4COOH (1 mM)/MEEA (4mM) mixture in DMSO at 140 K (blue). The absence of any significant shift by decreasing the temperature below the glass transition temperature of DMSO (292 K) indicates the molecularly dispersed state of DAT-4COOH/MEEA in glassy DMSO.

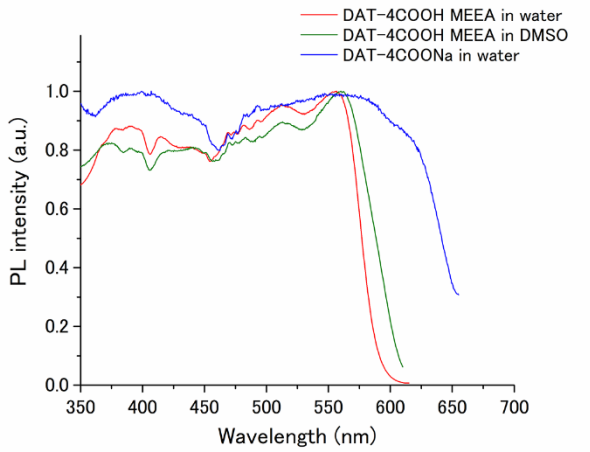

Figure 5-5. Excitation spectra of DAT-4COOH/MEEA in water at 140 K (red, [DAT-4COOH] = 1 mM, [MEEA] = 4 mM, λ_{dt} = 630 nm), DAT-4COOH/MEEA in DMSO at 140 K (green, [DAT-4COOH] = 1 mM, [MEEA] = 4 mM, λ_{dt} = 625 nm), and DAT-4COONa in water at 140 K (blue, [DAT-4COONa] = mM, λ_{dt} = 670 nm).

5.3.2 Polarizing properties in photo-excited triplet state

The generation of polarized triplet electrons in ice was confirmed by time-resolved electron paramagnetic resonance (EPR) measurements with a home-build setup.[20] Under pulsed excitation at 532 nm, EPR spectra of DAT-4COOH/MEEA in water at 140 K showed the typical shape for photo-excited triplet state of DAT (Figure 5-6a). The EPR spectrum was simulated by using the EasySpin toolbox in MATLAB.[28] The zero-field splitting parameters (|D| = 1484 MHz and |E| = 133 MHz) and relative zero-field populations (P_x : P_y : P_z = 0.56 : 0.21 : 0.23) of DAT-4COOH/MEEA were close to the values of DAT (Figure 5-6a and Table 5-1).[20] The hydrophilic modification to DAT skeleton has no significant effect on triplet polarization properties. A lifetime of EPR signal decay of DAT-4COOH/MEEA in water at 140 K was 37 μs (Table 5-2), being long enough for triplet-to-nuclei polarization transfer.

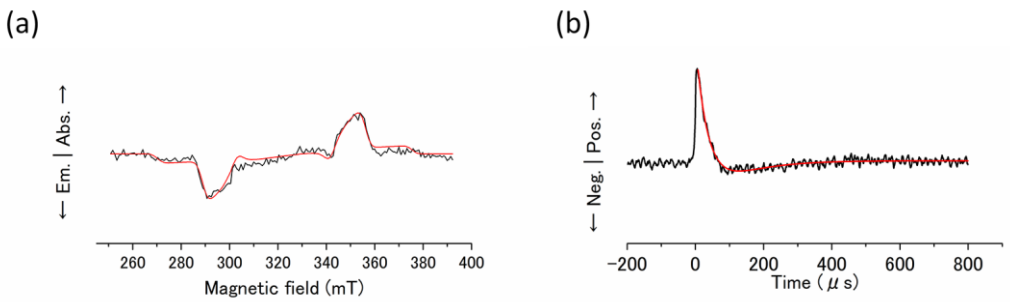

Figure 5-6. (a) Time-resolved ESR spectrum (black) and simulated spectrum (red) of DAT-4COOH/MEEA in water at 140 K just after pulsed photoexcitation at 532 nm ([DAT-4COOH] = 1 mM, [MEEA] = 4 mM). (b) Decay of the EPR peak at 354 mT under pulsed photoexcitation at 532 nm of DAT-4COOH/MEEA in water at 140 K (black), and its fitting result according to the following equation, $A \exp(-t/\tau_A) + B \exp(-t/\tau_B) + C$. (red).

We also checked the effect of MEEA concentration (4, 6, 8, 20, 40 mM) in 1 mM DAT-4COOH aqueous dispersion. The EPR signal intensity at 140 K was not largely changed by the increased MEEA concentration (Figure 5-7), and thus four equivalents of MEEA are sufficient to disperse DAT-4COOH in ice.

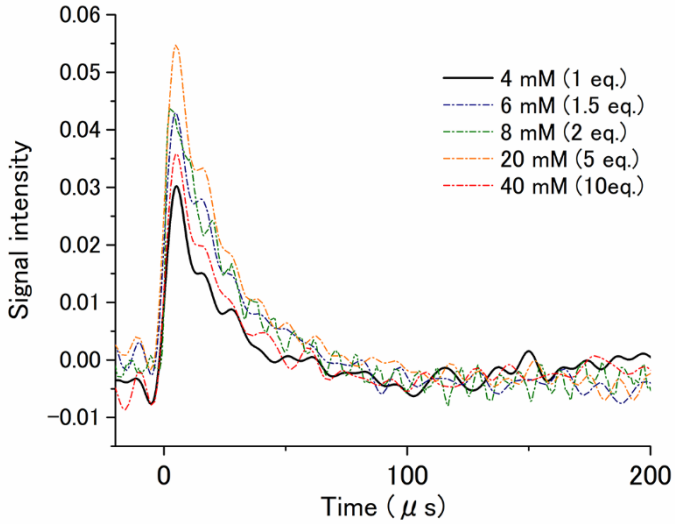

Figure 5-7. Time-resolved EPR signal intensity of DAT-4COOH (1 mM)/MEEA in water at 140 K with different MEEA concentrations of 4, 6, 8, 20, and 40 mM.

Table 5-1. Zero-field splitting parameters and relative zero-field populations derived from simulation of the time-resolved EPR spectra of 0.05mol% DAT in *p*-terphenyl at room temperature[20] and DAT-4COOH/MEEA ([DAT-4COOH] = 1 mM, [MEEA] = 4 mM) in water at 140 K. D and E were assumed to be both positive.

	|D| (MHz)	|E| (MHz)	P_x	P_y	P_z
5,12-diazatetracene (DAT)	1598	153	0.71	0.11	0.18
DAT-4COOH MEEA	1484	133	0.56	0.21	0.23

Table 5-2. EPR decay time of 0.05 mol% DAT in *p*-terphenyl at room temperature[20] and DAT/4COOH MEEA ([DAT-4COOH] = 1 mM, [MEEA] = 4 mM) in water at 140 K. The fitting was according to be following equation: $A \exp(-t/\tau_A) + B \exp(-t/\tau_B) + C$.

	A	τ_A (μs)	B	τ_B (μs)
5,12-diazatetracene (DAT)	0.22	11	-0.023	98
DAT-4COOH MEEA	0.031	37	-0.0094	108

5.3.3 ^{1}H hyperpolarization of crystalline ice

The triplet-DNP process was conducted for water doped with DAT-4COOH/MEEA at 140 K by the integrated solid effect (ISE) sequence. The triplet polarizing agent was photo-excited by 400 Hz pulsed 532 nm laser, followed by a 17.7 GHz microwave irradiation for 30 μs under a magnetic field sweep (± 30 mT). After repeating the triplet-DNP sequence to accumulate the spin polarization, the polarized sample was shuttled to the coil above the resonator within 3 s and ^{1}H NMR signal was measured. Typically, the spin-lattice relaxation time (T_1) of crystalline ice is longer than 5 min at 200K, and that of glassy water is much shorter around 5 s.[29,30] The buildup curve was fitted with the following equation, A[1-exp(-t/T_B)], and T_B was estimated as 11.6 minutes (Figure 5-8). polarization is transferred to crystalline water ^{1}H with long T_1. An enhancement factor (ε) of 23 at 140 K was obtained for ^{1}H of water molecules. The enhancement factor was calculated by comparing the thermal equilibrium signal of methanol at 140 K. When the NMR signal intensity is compared with the room-temperature signal, ε was 49. The first example of triplet-DNP of crystalline water is achieved by molecularly dispersing the water-soluble polarizing agent with the help of bulky hydrophilic counter cation.

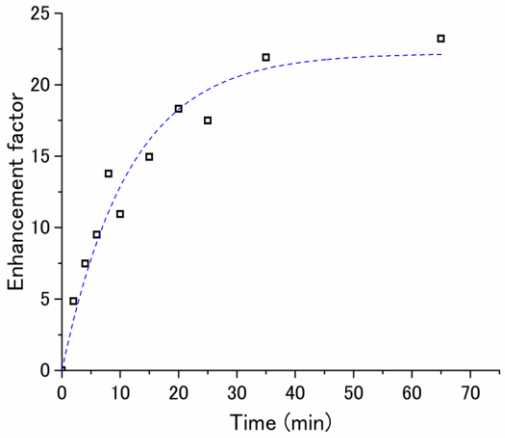

Figure 5-8. Buildup curve of the ^{1}H NMR signal of water doped with DAT-4COOH/MEEA at 140 K and 664 mT. The broken line is a fitting curve with the following equation, A[1-exp(-t/T_B)].

5.3.4 Consideration

This moderate polarization enhancement is partly due to the quantum yield of triplet formation through ISC (Φ_{ISC}). 0.05 mol% DAT doped in *p*-terphenyl crystalline powder showed a very low fluorescence quantum yield Φ_F < 1% at 77 K, implying the efficient ISC. On the other hand, Φ_F of DAT-4COOH/MEEA in ice at 77 K was 77%, indicating the maximum Φ_{ISC} of 23%. Another possible reason is the disorder of ice crystals around the DAT-4COOH/MEEA ion pair. When dilute aqueous solutions are frozen, the coexistence of the water-rich crystalline part and the solute-rich glassy part is widely observed.[31] The glassy region around the polarizing agents might induce a faster T_1 relaxation.[32-34] Indirect information about the size of the glassy region is provided by the characterizations of DAT-4COOH/MEEA in water at 300 K. Compared with the molecularly-dispersed state of DAT-4COOH/MEEA in ice, DAT-4COOH/MEEA in water at 300 K showed a red-shift and broadening in excitation and fluorescence spectra (Figure 5-9). These results indicate the aggregation of DAT-4COOH/MEEA in water at room temperature, which was also supported by the red-shift and broadening in absorption and fluorescence spectra compared with the molecularly-dispersed DAT-4COOH/MEEA in DMSO at 300 K (Figure 5-10).

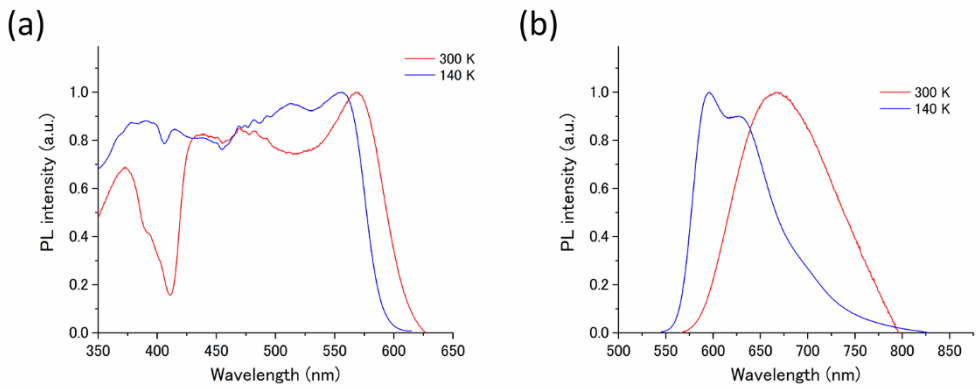

Figure 5-9. (a) Excitation spectra of DAT-4COOH/MEEA in water ([DAT-4COOH] = 1 mM, [MEEA] = 4 mM) at 300 K (red, λ_{dt} = 665 nm) and 140 K (blue, λ_{dt} = 630 nm). (b) Photoluminescece (PL) spectra (λ_{ex} = 532 nm) of DAT-4COOH (1 mM)/MEEA (4 mM) mixture in water at 300 K (red) and 140 K (blue).

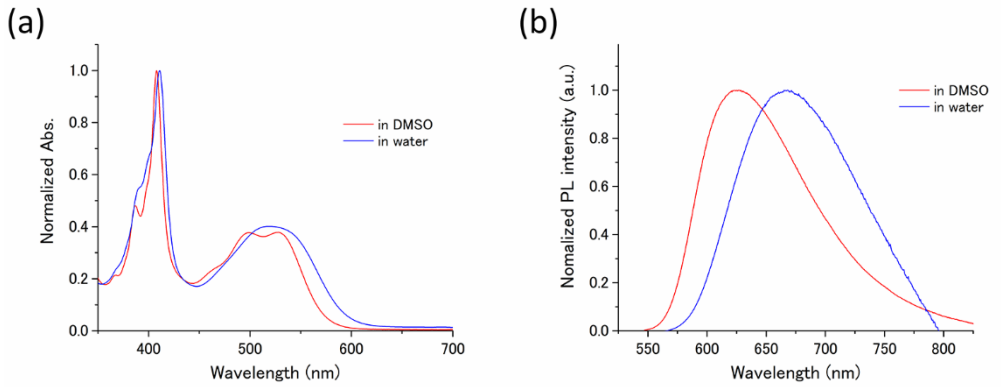

Figure 5-10. (a) Absorption spectra of DAT-4COOH (1 mM)/MEEA (4 mM) mixture in DMSO (red) and in water (blue) at 300 K. (b) Photoluminescece (PL) spectra (λ_{ex} = 532 nm) of DAT-4COOH (1 mM)/MEEA (4 mM) mixture in DMSO (red) and in water (blue) at 300 K.

Dynamic light scattering (DLS) measurements of DAT-4COOH/MEEA in water at room temperature confirmed the presence of nano-aggregates with an average size of 64 nm (Figure 5-11). Therefore, interestingly, the nanoscale aggregates of DAT-4COOH/MEEA disassemble during the freezing of water. Taking into account that DAT-4COONa aggregates in ice, MEEA should play an important role to form amorphous water structure around the polarizing agents.[35] It would be reasonable to consider that the solute (DAT-4COOH/MEEA)-rich, glassy nanodomains are formed within the crystalline ice, which results in the coexistence of two solid parts with different ^{1}H T_1 values.

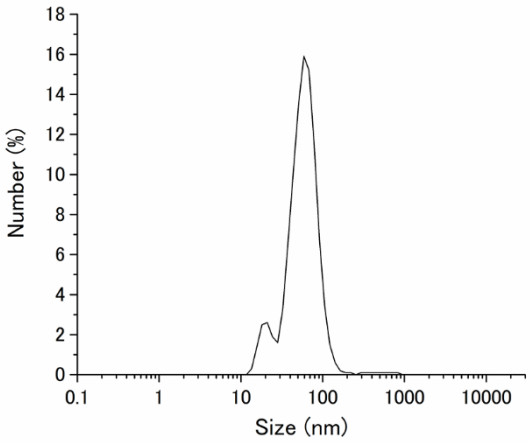

Figure 5-11. DLS profile of DAT-4COOH/MEEA in water ([DAT-4COOH] = 1 mM, [MEEA] = 4 mM).

5.4 Conclusion

In conclusion, we showed the first example of the water-soluble triplet-DNP polarizing agent and demonstrated the first example of ^{1}H NMR signal enhancement of crystalline ice by triplet-DNP. The ion-pairing of the triplet polarizing agent with the bulky and hydrophilic amine allows the good dispersibility of the polarizing agent in the crystalline ice matrix. The polarized photo-excited triplet state is produced in water at 140 K, and the electron polarization is successfully transferred to ^{1}H nuclei of water molecules in crystalline ice. This work provides an important initial step toward the hyperpolarization of various biomolecules through proton exchange with water and the contrast enhancement in MRA to diagnose various organs.

References

(1) Overhauser, A. W. *Phys. Rev.* **1953,** *92*, 411-415.

(2) Carver, T. R.; Slichter, C. P. *Phys. Rev.* **1953,** *92*, 212-213.

(3) Hall, D. A.; Maus, D. C.; Gerfen, G. J.; Inati, S. J.; Becerra, L. R.; Dahlquist, F. W.; Griffin, R. G. *Science* **1997,** *276*, 930-932.

(4) Gallagher, F. A.; Kettunen, M. I.; Day, S. E.; Hu, D. E.; Ardenkjær-Larsen, J. H.; Zandt, R.; Jensen, P. R.et al. *Nature* **2008,** *453*, 940-943.

(5) Rossini, A. J.; Zagdoun, A.; Lelli, M.; Lesage, A.; Copéret, C.; Emsley, L. *Acc. Chem. Res.* **2013,** *46*, 1942–1951

(6) Chappuis, Q.; Milani, J.; Vuichoud, B.; Bornet, A.; Gossert, A. D.; Bodenhausen, G.; Jannin, S. *J. Phys. Chem. Lett.* **2015,** *6*, 1674-1678.

(7) Kurzbach, D.; Canet, E.; Flamm, A. G.; Jhajharia, A.; Weber, E. M. M.; Konrat, R.; Bodenhausen, G. *Angew. Chem. Int. Ed.* **2017,** *56*, 389-392.

(8) Ajoy, A.; Liu, K.; Nazaryan, R.; Lv, X.; Zangara, P. R.; Safvati, B.; Wang, G.et al. *Sci. Adv.* **2018,** *4*, eaar5492.

(9) Lingwood, M. D.; Siaw, T. A.; Sailasuta, N.; Abulseoud, O. A.; Chan, H. R.; Ross, B. D.; Bhattacharya, P.et al. *J. Radiol.* **2012,** *265*, 418-425.

(10) Lipsø, K. W.; Hansen, E. S. S.; Tougaard, R. S.; Laustsen, C.; Ardenkjær-Larsen, J. H. *Magn. Reson. Med.* **2018,** *80*, 1165-1169.

(11) Harris, T.; Szekely, O.; Frydman, L. *J. Phys. Chem. B* **2014,** *118*, 3281-3290.

(12) Kim, J.; Mandal, R.; Hilty, C. *J. Phys. Chem. Lett.* **2019,** *10*, 5463-5467.

(13) Sadet, A.; Stavarache, C.; Bacalum, M.; Radu, M.; Bodenhausen, G.; Kurzbach, D.; Vasos, P. R. *J. Am. Chem. Soc.* **2019,** *141*, 12448-12452.

(14) Jannin, S.; Dumez, J. N.; Giraudeau, P.; Kurzbach, D. *J. Magn. Reson.* **2019,** *305*, 41-50.

(15) Henstra, A.; Lin, T.-S.; Schmidt, J.; Wenckebach, W. T. *Chem. Phys. Lett.* **1990,** *165*, 6-10.

(16) Iinuma, M.; Takahashi, Y.; Shaké, I.; Oda, M.; Masaike, A.; Yabuzaki, T.; Shimizu, H. M. *J. Magn. Reson.* **2005,** *175*, 235-241.

(17) Takeda, K. *Triplet State Dynamic Nuclear Polarization*; VDM Verlag Dr. Müeller: Saarbrücken, Germany, 2009.

(18) Tateishi, K.; Negoro, M.; Nishida, S.; Kagawa, A.; Morita, Y.; Kitagawa, M. *Proc. Natl. Acad. Sci. USA* **2014,** *111*, 7527-7530.

(19) Negoro, M.; Kagawa, A.; Tateishi, K.; Tanaka, Y.; Yuasa, T.; Takahashi, K.; Kitagawa, M. *J. Phys. Chem. A* **2018,** *122*, 4294-4297.

(20) Kouno, H.; Kawashima, Y.; Tateishi, K.; Uesaka, T.; Kimizuka, N.; Yanai, N. *J. Phys. Chem. Lett.* **2019,** *10*, 2208-2213.

(21) Nishimura, K.; Kouno, H.; Tateishi, K.; Uesaka, T.; Ideta, K.; Kimizuka, N.; Yanai, N. *Phys. Chem. Chem. Phys.* **2019,** *21*, 16408-16412.

(22) Fujiwara, S.; Hosoyamada, M.; Tateishi, K.; Uesaka, T.; Ideta, K.; Kimizuka, N.; Yanai, N. *J. Am. Chem. Soc.* **2018,** *140*, 15606-15610.

(23) Tateishi, K.; Negoro, M.; Kagawa, A.; Kitagawa, M. *Angew. Chem. Int. Ed.* **2013,** *52*, 13307-13310.

(24) Tateishi, K.; Negoro, M.; Nonaka, H.; Kagawa, A.; Sando, S.; Wada, S.; Kitagawa, M.et al. *Phys. Chem. Chem. Phys.* **2019,** *21*, 19737-19741.

(25) Yamada, M.; Ikemoto, I.; Kuroda, H. *Bull. Chem. Soc. Jpn.* **1988,** *61*, 1057-1062.

(26) Maliakal, A.; Raghavachari, K.; Katz, H.; Chandross, E.; Siegrist, T. *Chem. Mater.* **2004,** *16*, 4980-4986.

(27) Ishiba, K.; Noguchi, T.; Iguchi, H.; Morikawa, M. A.; Kaneko, K.; Kimizuka, N. *Angew. Chem. Int. Ed.* **2017,** *56*, 2974-2978.

(28) Stoll, S.; Schweiger, A. *J. Magn. Reson.* **2006,** *178*, 42-55.

(29) Barnaal, D. E.; Lowe, I. J. *J. Chem. Phys.* **1968,** *48*, 4614-4618.

(30) Koivula, E.; Punkkinen, M.; Tanttila, W. H.; Ylinen, E. E. *Phys. Rev. B: Condens. Matter Mater. Phys.* **1985,** *32*, 4556-4564.

(31) Suzuki, Y. *J. Chem. Phys.* **2019,** *150*, 224508.

(32) Ji, X.; Bornet, A.; Vuichoud, B.; Milani, J.; Gajan, D.; Rossini, A. J.; Emsley, L.et al. *Nat. Commun.* **2017,** *8*, 13975.

(33) Salzmann, C. G. *J. Chem. Phys.* **2019,** *150*, 060901.

(34) Wang, Q.; Huang, X.; Guo, W.; Cao, Z. *Phys. Chem. Chem. Phys.* **2019,** *21*, 10293-10299.

(35) Gemmei-Ide, M.; Motonaga, T.; Kasai, R.; Kitano, H. *J. Phys. Chem. B* **2013,** *117*, 2188-2194.

Chapter 6 Conclusions and future remarks

6.1 Conclusions of all the chapters

The first chapter of this thesis provided the introduction of the intriguing phenomena using photo-excited state, especially TTA-UC and triplet-DNP, and their research histories. A lot of physicists have developed fundamental researches for TTA-UC and triplet-DNP. On the other hand, a few researchers have designed molecules in terms of giving functions. The work presented in this thesis discussed the concept of developing self-assembly molecular systems with the ability to work in aqueous media.

Chapters 2 and 3 discussed the air-saturated aqueous triplet energy migration-based TTA-UC systems. In chapter 2, the first example of triplet energy migration-based aqueous TTA-UC system was developed and dense intermolecular networks driven by hydrogen bonding successfully suppressed oxygen quenching. To deepen the understanding of oxygen-barrier mechanism, a novel amphiphilic acceptor was designed and TTA-UC properties were investigated through the structural effect of introducing various hydrophobic counterions. The consequent dense molecular organization exhibited a physical energy barrier to oxygen permeation and thus suppressed the quenching of triplet excited states by dissolved oxygen molecules.

In chapters 4 and 5, molecular design guidelines to achieve ^{1}H hyperpolarization of water molecules were shown. Chapter 4 described the potential of diaza-substituted acenes as triplet polarizing agents. DAT and DAP showed much higher photo-stability compared with pentacene, which is a conventional triplet polarizing agent, and the enhanced of ^{1}H NMR signals were comparable with that of pentacene. In chapter 5, water-soluble triplet polarizing agent based on DAT skeleton was designed. The polarizing agent ion-paired with hydrophilic amine was well-dispersed in crystalline ice. This allowed the first demonstration of crystalline ice by triplet-DNP was shown.

6.2 Future remarks

TTA-UC

In this thesis, air-stable aqueous TTA-UC systems were presented, however, their conversion wavelengths were vis (green: 532 nm)-to-vis (blue: 440 nm). For biological applications, NIR excitation is desired from the viewpoint of biopermeability. Although recent efforts have been contributed to the development of NIR-to-vis TTA-UC, solution systems and there are limited researchers related to aqueous dispersion systems in aerated condition. In addition, I_{th} value should be further improved especially in NIR-to-vis UC. Self-assembly approach has the potential to achieve oxygen-barrier and low I_{th}. Amphiphilic assemblies can incorporate hydrophobic donors without aggregation allowing the enhancement of absorption coefficient. If re-absorption of donor is hampered, NIR-to-vis TTA-UV with low I_{th} would be expected.

Triplet-DNP

The ^{1}H polarization of crystalline ice was shown in chapter 5, however, the enhancement factor was dozens of time. The reason might be due to the ISC quantum yield and the vitrification around the DAT-COOH/MEEA ion pair. The relationship between T_1 and S_1 should be precisely controlled because the relationship of energy levels could be changed in frozen condition. DAT skeleton gave flexibility to the molecular design thanks to its photo-stability and solubility in common solvents. It is expected that the newly designed triplet polarizing agents would achieve better enhancement of ^{1}H NMR signal of water.